# Designing eco-efficient structures using multi-material topology optimization
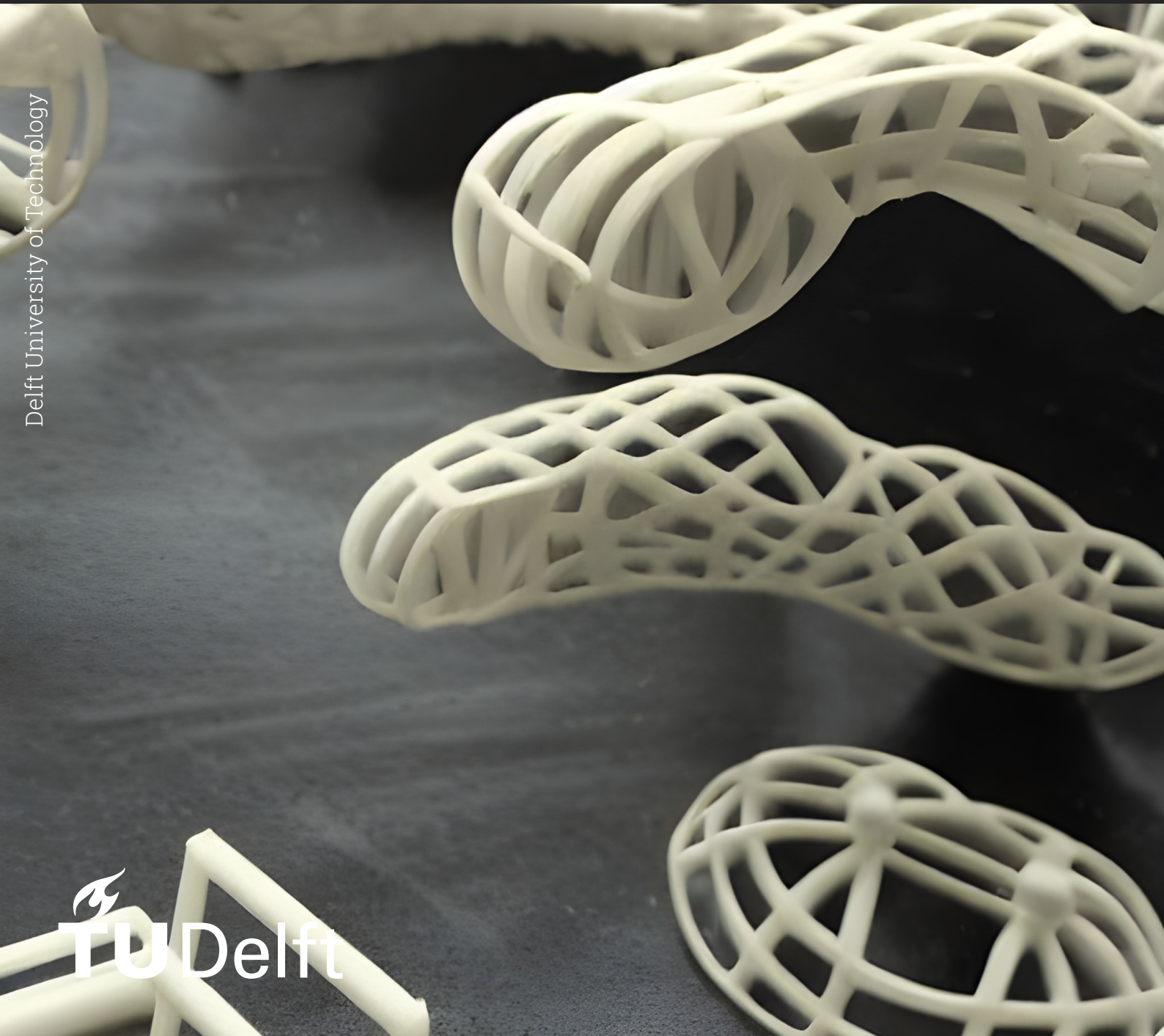
Master Thesis Report

Tanuj Agrawal

TUDelft

# Designing eco-efficient structures using multi-material topology optimization

by

## Tanuj Agrawal

to obtain the degree of Master of Science
at the Delft University of Technology,
to be defended publicly on Wednesday May 29, 2024 at 09:00 AM.

**ŤU**Delft

# Acknowledgements

# Abstract

Designing lightweight aircraft parts to improve fuel efficiency is crucial to meet the aviation sector's goals of reducing $CO_2$ emissions. However, it is also important to ensure that these lightweight parts have a lower $CO_2$ footprint over their entire lifetime. Previous studies have successfully achieved this using topology optimization and low-embodied $CO_2$ composite materials. However, it resulted in structures with lower mechanical properties. To address this limitation, a new framework that uses multi-material fibre-angle topology optimization to optimize fibre-reinforced composite structures is developed in this work. This approach optimizes low-embodied $CO_2$ footprint composites and high-performance, high-embodied $CO_2$ composites in the same structure.

A comprehensive $CO_2$ footprint assessment of the optimized structures is conducted by varying the amount of each of the two materials in the structure. As a result, a series of multi-material composite structures with varying levels of compromise between stiffness and $CO_2$ footprint are obtained. These findings establish an optimization approach that provides more control over tuning the desired objectives of such structures. In addition, an extensive parametric study is conducted to demonstrate the framework's robustness. However, during this analysis, certain limitations of the framework are identified, such as difficulties in optimizing fibres and material modelling. To overcome these limitations, a more robust framework can be developed in the future. Additionally, incorporating stress-based topology optimization into the existing framework can also help in achieving further improved designs.

# Contents

# Nomenclature

## Abbreviations

| Abbreviation | Definition |
|---|---|
| AM | Additive Manufacturing |
| BFRP | Bamboo Fibre Reinforced Polymer |
| $CO_2$ | Carbon dioxide |
| CC1 | Convergence Criterion 1 |
| CC2 | Convergence Criterion 2 |
| CC3 | Convergence Criterion 3 |
| CFAO | Continuous Fibre Angle Optimization |
| CFRP | Carbon Fibre Reinforced Polymer |
| CF | Carbon Fiber |
| DCP | Discrete-Continuous Parameterization |
| DMO | Discrete Material Optimization |
| ESO | Evolutionary Structural Optimization |
| FAO | Fiber Angle Optimization |
| FATO | Fibre Angle Topology Optimization |
| FDM | Fused Deposition Modelling |
| FEA | Finite Element Analysis |
| FEM | Finite Element Method |
| FFRP | Flax Fibre Reinforced Polymer |
| FRC | Fuel Reduction Coefficient |
| FRPC | Fibre Reinforced Polymer Composite |
| GCMMA | Globally Convergent Method of Moving Asymptotes |
| GFRP | Glass Fibre Reinforced Polymer |
| HFRP | Hemp Fibre Reinforced Polymer |
| HSM | Heaviside projection method |
| LM | Low Modulus |
| LCA | Life Cycle Assessment |
| MBB | Messerschmitt-Bölkow-Blohm |
| MMA | Method of Moving Asymptotes |
| MMCAP | Multi-Material Composite Anisotropic Penalization |
| MM-FATO | Multi Material Fibre Angle Topology Optimization |
| MMTO | Multi-Material Topology Optimization |
| NFRPC | Natural Fibre Reinforced Polymer Composite |
| PLA | Poly-lactic Acid |
| SIMP | Solid Isotropic Material Penalization |
| SM-FATO | Single Material Fibre Angle Topology Optimization |
| SMTO | Single Material Topology Optimization |
| TO | Topology Optimization |
| UD | Unidirectional |

# Symbols

| Symbol | Definition | Unit |
| --- | --- | --- |
| $\beta$ | Heaviside projection parameter | - |
| B | Strain-displacement matrix | - |
| C | Compliance or two times strain energy | [N.mm] |
| $D_e$ | Elemental constitutive matrix | [MPa] |
| $D_e^j$ | Elemental constitutive matrix of $j-th$ material | [MPa] |
| $D_g$ | Measure of discreteness | - |
| $E_x$ | Longitudinal tensile modulus | [MPa] |
| $E_y$ | Transverse tensile modulus | [MPa] |
| $f(x)$ | Objective function | - |
| $g_j$ | Linear inequality constraints | - |
| $G_{xy}$ | In-Plane shear modulus | [MPa] |
| $h_{95}$ | DMO convergence value | - |
| $K_e$ | Elemental stiffness matrix | [MPa] |
| $m$ | Number of candidate materials | - |
| $N$ | Number of finite elements | - |
| $\nu_{xy}$ | Major in-plane Poisson's ratio | - |
| $\nu_{yx}$ | Minor in-plane Poisson's ratio | - |
| $\theta$ | Fibre orientation | [radians] |
| $\Omega$ | Design domain volume | - |
| $\Omega_f$ | Filled design domain volume | - |
| $\Omega_1$ | Design domain volume occupied by material 1 | - |
| $\Omega_2$ | Design domain volume occupied by material 2 | - |
| $p$ | Penalization factor | - |
| $\psi$ | Measure of shear stiffness | - |
| $\rho$ | Material Density | [kg/m$^3$] |
| $r_{min}$ | Filter radius | [mm] |
| $T_1$ | Transformation matrix to transform stress matrix of an off-axis laminate | - |
| $T_2$ | Transformation matrix to transform strain matrix of an off-axis laminate | - |
| $U_e$ | Elemental displacement | [mm] |
| $V_f$ | Fibre volume fraction | - |
| $w(x_i)$ | Linear decaying weighting function for filtering | - |
| $w_j$ | Weights for DMO multi-material interpolation | - |
| $x_i^{matj}$ | Material density design variable for $i^{th}$ finite element and $j^{th}$ material | - |
| $\tilde{x}_i^{matj}$ | Filtered material density variable for $i^{th}$ finite element and $j^{th}$ material | - |

# List of Figures

# List of Tables

# Introduction

Businesses globally are increasingly driven towards sustainability, particularly in the aerospace industry. In order to avoid the negative effects of climate change, it is essential that a target to reduce net global $CO_2$ emissions to half of what they were in 2005 is met by 2050. However, achieving these climate change goals in the face of a growing aerospace sector requires a comprehensive decarbonization of the industry [1]. The impact of various measures on projected $CO_2$ emissions for the aviation sector can be observed in Figure 1.1.
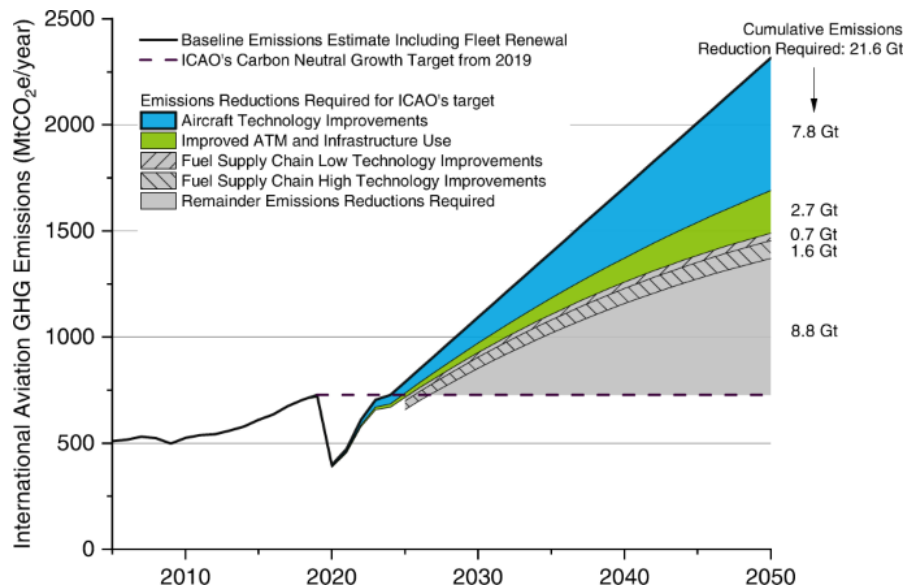


**Figure 1.1:** Projection of the aviation sector's jet-fuel based $CO_2$ emissions, and possible reduction. Aircraft technology improvement and air traffic management can reduce 7.8 and 2.7 gigatons of $CO_2$ emissions of the 21.6 gigatons required to meet the ICAO goal of carbon neutral growth target from 2019 [2].

Projected $CO_2$ emissions in Figure 1.1 clearly show that despite improvements in air traffic management and aircraft technology, a deficit of 8.8 gigatons of $CO_2$ emissions to meet the carbon-neutral growth target would persist. While sustainable aviation fuels or SAFs hold promise, they are not yet scalable or cost-effective. Therefore, the aviation sector must implement quicker-to-the-market solutions to reduce $CO_2$ emissions in the meantime. These solutions include lightweighting, blended fuels, more efficient engines, improved aerodynamics and flight operations [1], [2].

A reduced aircraft weight leads to decreased lift and drag during flight. This lowers the required thrust and, subsequently, jet fuel consumption. For every extra ton of weight saved on an aircraft, a projected 3% to 10% reduction in fuel consumption for short-haul flights and

20% to 25% reduction for long-haul flights can be achieved. Its equivalent impact on reducing the $CO_2$ emissions can be estimated from the fact that combusting a kilogram of fuel releases 3.16 kilogram of $CO_2$ into the atmosphere [1].

Composite materials are increasingly being used in aircraft structures due to their high specific properties. This helps in reducing the weight of the aircraft and, in turn, increases its fuel efficiency [3]. For instance, Boeing 787 extensively utilize fibre-reinforced composites, which make up for almost 50% of its weight. This results in a 20% weight reduction compared to similar models made from heavier metal and leads to fuel efficiency gains of 10-12% [4].

On the other hand, structural optimization approaches like topology optimization can also be used as an effective light-weighting tool. It helps reduce material use and enhance structural performance by redistributing the material in the structure where it is needed. When combined with high-performance composite materials, lightweight designs can be created for aerospace components. This relatively newer practice involves applying these materials to "numerically optimized structures" and using non-conventional manufacturing techniques, such as additive manufacturing (AM), to fabricate them [3].

However, a limitation of composites like carbon fibre-reinforced polymers (CFRP) is their reliance on petroleum-based polymer materials and highly energy-intensive raw materials like carbon fibres. This raises sustainability questions regarding raw material $CO_2$ footprint and end-of-life disposal options when compared to metals that they replace [5].

The work of Almeida [6] proposed an eco-design approach to address this issue. In his work, the concepts of using low embodied $CO_2$ footprint natural fibre-reinforced polymer composites (NFRPCs) and structural optimization were combined to reduce the environmental impacts of synthetic composite structures. The topology-optimized NFRPC structures successfully reduced the $CO_2$ emissions of a part over its lifetime. However, on their own, these structures did not provide the high stiffness required for highly loaded aerospace structures without a mass penalty.

Thus, this thesis aims to find a way to address this limitation of Almeida's [6] work, using its results as a starting point. In this work, multi-material topology optimized structures are hypothesized to design more eco-efficient structures for aviation while achieving good mechanical properties. Multi-material structures are envisioned to combine the high stiffness and low embodied $CO_2$ footprint of CFRP and NFRPC, respectively, to create better-compromised designs that can simultaneously meet the aero-structures' mechanical and eco-efficiency requirements.

To achieve this goal, we define a detailed research scope and direction by reviewing the state-of-the-art regarding multi-material structures for composites and the relevant research gaps in Chapter 2. The design choices and considerations for the required multi-material topology optimization framework for composites based on the state-of-the-art are then evaluated in Chapter 3. Following the design choices established in the previous chapter, Chapter 4 details the computational framework. In Chapter 5, the design of experiments for a parameter-based sensitivity study and eco-efficiency performance assessment is underlined. The results and analysis for the verification tests are then detailed in Chapter 6. In Chapter 7, we discuss the issues and limitations of the framework. Lastly, the conclusions and recommendations for future work are outlined in Chapters 8 and 9, respectively.

# 2

# Background and Research Scope

## 2.1. Introduction to Topology Optimization

Structural optimization, a broader field that encompasses topology optimization, started as simple cross-section size optimization for truss structures in civil engineering applications. It soon evolved into more complex optimization problems, such as optimizing the structural boundary or shape of structures and optimizing the material distribution within a solid block structure. These optimization exercises were termed shape optimization and topology optimization, respectively. Figure 2.1 shows these three primary forms of structural optimization in the order of their development [7].
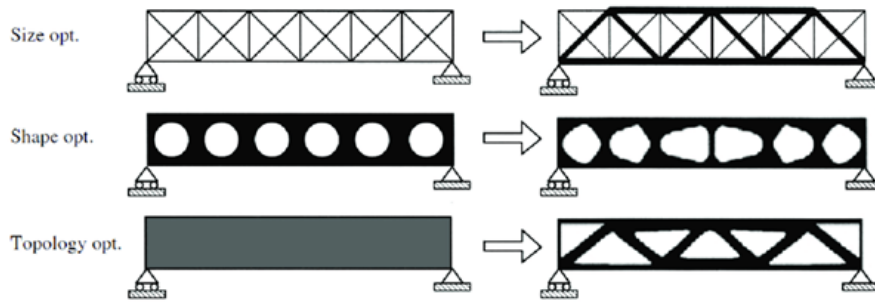


**Figure 2.1:** Structural optimization techniques employed in engineering practice namely, size optimization (Top), shape optimization (Middle), and topology optimization (Bottom) [8].

As seen from Figure 2.1, each of the structural optimization techniques differs from the others in some aspects. The optimization of an object's dimensions, such as its length, width, or depth, falls under size optimization. Shape optimization, on the other hand, focuses on determining the optimal shape of a part by optimizing the openings, often referred to as holes. However, when optimizing the overall geometry of a part, which encompasses both its size and shape, we can term such an optimization exercise as topology optimization [8]. Of all these aforementioned structural optimization techniques, the primary focus of this work and literature review is topology optimization.

Topology optimization (TO) is often employed in engineering applications to optimize the distribution of material in a domain such that the performance of the part is maximized. Numerical optimization algorithms are employed to remove material regions in the part that are not contributing to its overall performance like stiffness or deformation [8]. As a result, implementing topology optimization for complex problems can result in unanticipated topologies. This makes it an effective tool for designing novel and lightweight aircraft structures that can reduce the aerospace sector's carbon footprint.

## 2.1.1. General Optimization Problem

In the most general form, any structural optimization problem, including topology optimization, can be expressed by Equation 2.1.

$$
\begin{array}{lll}
\textbf{minimize} & f(\mathbf{X}) & \text{minimize this objective function} \\
\textbf{Subject to} & \mathbf{X} = (x_1, x_2, ..., x_N)^T, & \text{design variables} \\
& x_i^l \leq x_i \leq x_i^u, \quad i = 1, \ldots, N & \text{bound constraints} \\
& h_j(\mathbf{X}) = 0, \quad j = 1, \ldots, N_h & \text{equality constraints} \\
& g_k(\mathbf{X}) \leq 0, \quad k = 1, \ldots, N_g & \text{inequality constraints}
\end{array}
\tag{2.1}
$$

Where $f(\mathbf{X})$ is the objective function that the optimization algorithm minimizes. The design variable vector represented by $\mathbf{X}$ is the means to change the design during optimization. The $N$ individual design variables $x_i$ of the design variable vector $\mathbf{X}$ define the design space of the optimization problem. In the context of structural optimization, these design variables can represent geometrical dimensions, physical properties like material density, etc., or other physical aspects like fibre orientations.

The design variable $x_i$ is often restricted by an upper bound, $x_i^u$ and a lower bound, $x_i^l$. In most engineering-relevant problems, these design variables are further constrained using $N_h$ equality or $N_g$ inequality constraints $h_j(\mathbf{X})$ and $g_k(\mathbf{X})$. For a feasible solution to exist for any given problem, all such constraints restricting the design space must be satisfied. Numerical optimization algorithms are used to update the design variables while satisfying these constraints to find the best solution. This update of design variables is done through an iterative process, which runs until the stopping criteria are satisfied [9].

## 2.1.2. Optimization Algorithm

Optimization algorithms can be broadly classified into gradient-free and gradient-based techniques depending on how they achieve the best possible solution for a problem. The main difference between the two is the use of gradients to obtain a solution.

A primary drawback associated with the first category of algorithms is the significantly high computational costs, which increase with the number of unknowns or design variables. This is significantly higher than what gradient-based optimization techniques require, given that they are local search algorithms and use gradient information to devise better search directions. This difference in the computational efficiency of both these strategies can also be seen in Figure 2.2a. Consequently, gradient-based approaches are preferred for structural optimization problems with a higher number of design variables [7].

In its simplest form, a gradient-based optimization algorithm optimizes an unconstrained problem by determining a local search direction and the best step size in that search direction. A general representation of how the gradient-based approaches use gradient information to reach a minimum can be visualized from Figure 2.2b. A descent direction is determined using first-order local information (gradient) at the current step. Such a gradient-based search is called steepest-descent or gradient descent. A line search algorithm is then used to determine the suitable step size based on this descent search direction. This step size is proportional to the negative of the function's gradient at the current point and is evaluated iteratively until the stopping criteria are satisfied [7], [10].
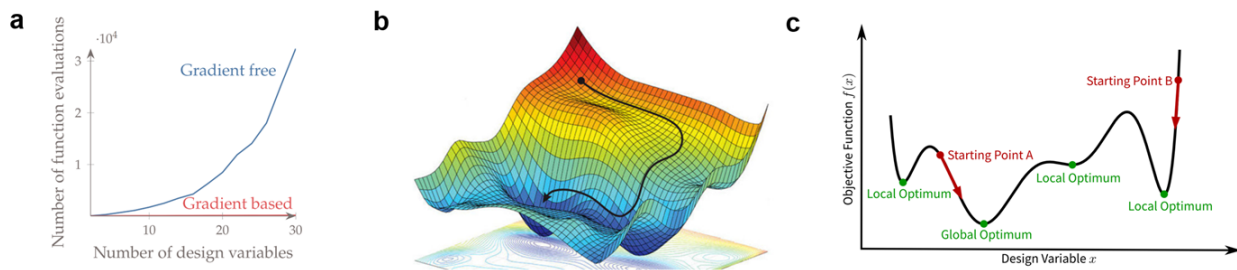
**Figure 2.2:** (a) Plot from [7], showing how gradient-based algorithms scale better with increasing number of design variables, compared to gradient-free optimization approaches due to use of gradient information, (b) The path taken by the optimization algorithm based on the local gradient information at each small step size, effectively allowing it to find the lowest point or minima [10] (c) A multi-modal objective function $f(x)$, can cause the optimization algorithm to optimize for a local minimum or the global optimum based on that initial design variable guesses B and A respectively [9].

Structural optimization problems are often non-convex or multi-modal, i.e., they have multiple locally optimal solutions that are not necessarily the global optimal solution. When solved using optimization algorithms that use local information or gradients, the final solution can depend on the initial guess. Different initial guesses can lead to different results, and the optimization algorithm may converge to either a local minimum or a global minimum based on where it starts [9]. This issue of non-convexity and the quality of the obtained solution, depending on the initial guess, can be further visualized from Figure 2.2c.

Nonetheless, if better solutions are to be achieved using gradient-based approaches that use local search, a multi-start strategy can be used. Where the gradient-based algorithm is run multiple times in parallel for multiple initial guesses. This results in a better solution, which might or might not be the global minimum but better than the solution for evaluating only a single initial guess [7], [9]. Hence, for the scope of this work, we limit our discussions to only gradient-based approaches.

## 2.1.3. Topology Optimization Approaches

The most prominent topology optimization approaches for continuum structures reported in the literature include density-based and boundary-based approaches. Solid isotropic material Penalization (SIMP) and evolutionary structural optimization (ESO) approaches fall under the density-based approach, and the level-set (LS) method can be classified as a boundary-based approach [9]. Figure 2.3 shows an overview of this classification. Of all the approaches mentioned, density-based approaches are generally more widely used. With more than 50 % of commercially available software using density-based approaches [11] for TO. Given their popularity, the scope of discussion is also limited to density-based TO approaches.

The foundation of numerous density-based topology optimization approaches lies in the utilization of discrete design variables, such as those found in Evolutionary Structural Optimization methods. However, Sigmund and Maute [12] highlight that employing density design variables restricted to discrete values, typically 0 or 1, makes it challenging to solve topology optimization problems with large design space. However, continuous design variables allow more efficient use of gradient-based algorithms to obtain convergence for such problems.
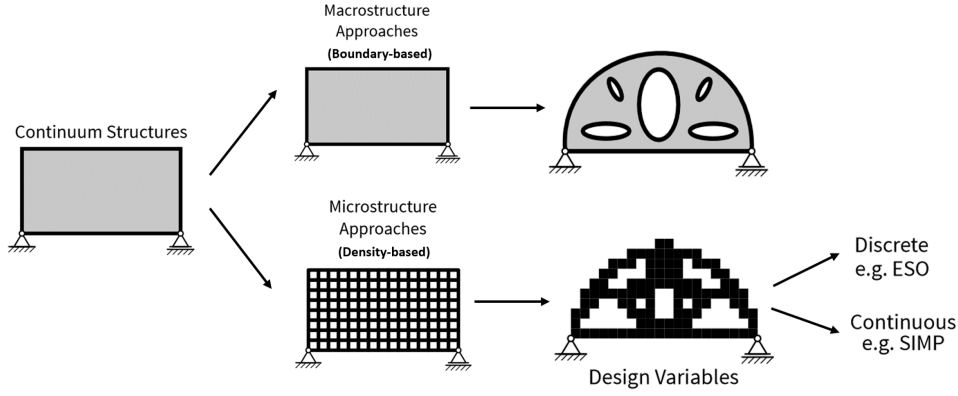
**Figure 2.3:** An overview of basic topology optimization approaches for continuum structures adapted from Lang [9], showing the primary approaches, which include macro-structure or boundary-based optimization and microstructure or density-based optimization approaches. Within density-based optimization approaches, the ESO approach uses discrete design variables, and SIMP uses continuous design variables for topology optimization.

A typical approach to the topology optimization problem involves discretizing the design domain using a finite element method (FEM). When the structure is discretized using $N$ finite elements, the size of holes becomes restricted by this discretization. In such cases, this inherent ill-posedness of the optimization problem is reflected in the numerical solution and is termed mesh-dependency. Achieving a well-posed problem then requires regularization of the topology optimization problem formulation. One popular option involves relaxing the discreteness of the design variable and incorporating intermediate material densities into the problem formulation. As a result, recent research for topology optimization approaches for continuum structures has largely concentrated on formulating optimization problems with continuous design variables. Examples of methodologies utilizing these continuous design variables include the *Homogenization approach* and *Solid Isotropic Material with Penalization* [9].

The *Homogenization approach* assumes a "periodically perforated microstructure", where different microstructures yield varying intermediate densities, for which the mechanical properties are determined using homogenization theory. Alternatively, relaxation can be achieved by utilizing a continuous material density value without microstructure. In that case, mechanical properties are then determined through a power-law interpolation function between "solid" and "void," implicitly penalising intermediate densities to drive the structure towards the desired black-and-white configuration, often termed "0-1" design. This approach is commonly known as *Solid Isotropic Material with Penalization (SIMP)*, where the density design variable $\boldsymbol{\rho}$ is often used to interpolate between the material property $E$ or Young's Modulus of an isotropic material. As a result for a discretized design domain, when $\rho_i = 0$, we have $E(\rho_i) = 0$, and for $\rho_i = 1$, we have $E(\rho_i) = E_0$ for the corresponding discrete element [9], [12].

However, using SIMP can cause numerical challenges like check-boarding patterns with alternating "0-1" densities and mesh dependence of design. To alleviate this ill-posedness of the problem with checker-boarding and mesh dependence, we restrict the design space instead of relaxing it too much through regularization schemes like mesh-independent filtering [9], [12]. While filtering schemes prevent numerical instabilities, they generate many intermediate-density elements in final topologies. These intermediate densities have no physical meaning. They also render the manufacturing processes of the designs complicated and increase costs. From a manufacturing perspective, generating "0-1" solutions at a macroscopic level is always attractive. A way to address this issue is using a thresholding method, where intermediate

densities are explicitly assigned 0 or 1 based on a cut-off value. However, this comes at the cost of a slightly worse or sub-optimal compliance result [13].

## 2.1.4. General Topology Optimization Formulation

A general formulation for a simple density-based topology optimization problem, like SIMP, can be written as,

$$\textbf{minimize} : C(\boldsymbol{\rho}) = \mathbf{U^T K}(\boldsymbol{\rho})\mathbf{U}$$

$$\textbf{subject to} : \begin{cases} \mathbf{K}(\boldsymbol{\rho})\mathbf{U} = \mathbf{F} \\ 0 \le \rho_i \le 1 \quad i = 1, ..., N \\ \frac{V(\boldsymbol{\rho})}{V_0} \le \Omega_f \end{cases} \tag{2.2}$$

Where $C(\boldsymbol{\rho})$ is the structure's compliance defined by the displacement vector $\mathbf{U}$ and global stiffness matrix $\mathbf{K}(\boldsymbol{\rho})$, which is a function of $\boldsymbol{\rho}$. The notation $\boldsymbol{\rho}$ represents the vector of $N$ material density design variables explicitly bounded between 0 and 1. Where 0 is void or absence of material, and 1 is a fully dense material. The values of $\mathbf{U}$ required to calculate the compliance are obtained by solving the static equilibrium equation $\mathbf{K}(\boldsymbol{\rho})\mathbf{U}=\mathbf{F}$. Where $\mathbf{F}$ is the global force vector. The inequality constraint defined for the problem is defined by $V(\boldsymbol{\rho})$ and $V_0$, representing the total material and design domain volumes, respectively. Their ratio is constrained to be less than equal to $\Omega_f$. Where $\Omega_f$ is the user-defined fraction of the design domain that can be occupied by the material densities.

Figure 2.4 illustrates a general optimization flow chart highlighting various steps to be considered for a density-based topology optimized problem, as stated in Equation 2.2.
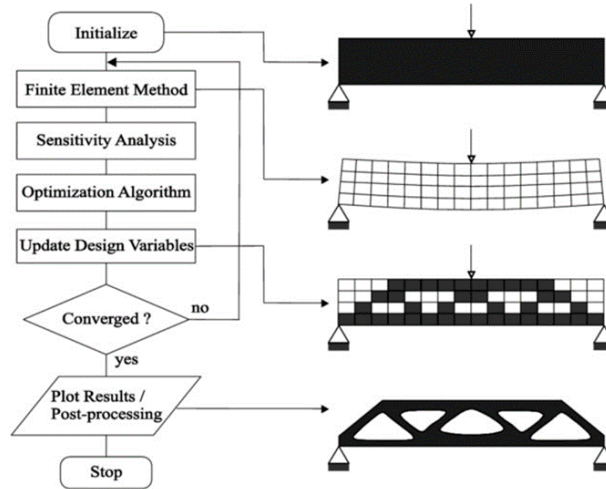


**Figure 2.4:** Steps utilized to solve a density-based topology optimization problem adapted from Bendsoe and Sigmund [14]

A similar iterative process mentioned earlier for a generalized optimization problem is used for density-based TO approaches. Where the design domain is first discretized into $N$ elements. Then, an initial guess is initialized by initializing the design variable $\boldsymbol{\rho}$. Next, the objective is evaluated by utilizing SIMP-like interpolation for material property and finite element analysis (FEA). After that, the objective and constraint gradients with respect to the design variables are calculated. With the help of the gradients, the optimization algorithm is then used to update the design to a better one with smaller objective functions. After each iteration, a check is performed to see if the stopping criteria and constraints are met. If yes, the optimization is stopped, and the results are plotted and processed. If not, then the process is repeated with the new design.

## 2.2. Composites and Topology Optimization

Reducing fuel consumption has been a top priority in the aerospace industry to meet the growing demands while keeping costs in check. Several solutions exist, including improving aerodynamic performance, engine efficiency, and fuel efficiency through better air traffic management and flight plans. Lightweighting is another widely used solution, where heavy metallic components are replaced with lighter materials, such as composites. These materials have high stiffness and low-density properties, which make them ideal for weight reduction [9].

Creating composite materials involves combining two or more materials to obtain a new material with improved properties over those of the individual constituents. Fibre-reinforced polymer composites (FRPCs) are the most common composite materials because of their high stiffness-to-mass and stiffness-to-strength ratios. However, creating FRPCs with specific loads and stiffness requirements can be challenging due to their anisotropic behaviour [9].

The anisotropic behaviour of FRPCs can be seen in Figure 2.5, where the Young's Modulus is evaluated for different layups of a carbon-fibre reinforced epoxy polymer with fibre volume fraction of 60%, along multiple loading directions [9].
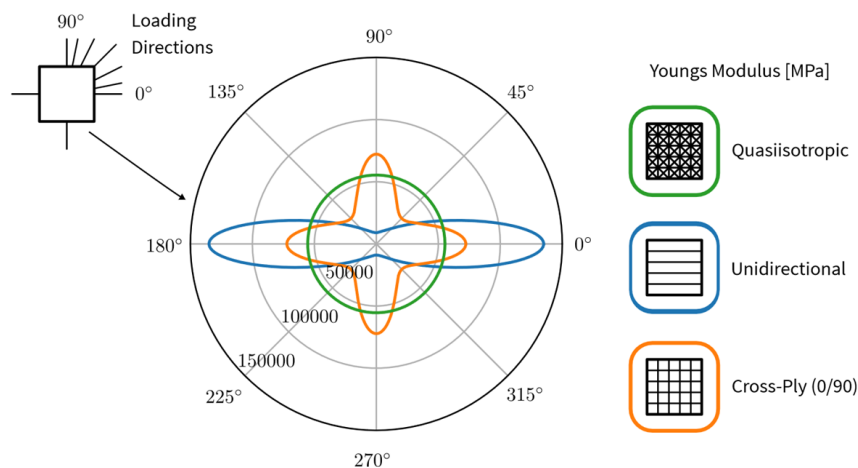


**Figure 2.5:** Polar plot showing the variation of Young's modulus along different directions for quasi-isotropic, unidirectional and cross-ply [0/90] carbon-epoxy composite layups, with the loading direction along the x-direction, or $\theta = 0°$. This highlights the high directionality of composites and the importance of optimal material alignment to achieve maximum mechanical properties [9].

It is evident from the plot that unidirectional layup provides the highest stiffness when the loading direction coincides with the direction of the fibres. Conversely, with more isotropic-like properties, the quasi-isotropic layup is largely unaffected by the loading directions. Ideally, for high-stiffness mass-sensitive applications, such as aviation, it would thus be preferable to employ unidirectional composites tailored to the loading direction to achieve more stiffness with less material. In conclusion, the simultaneous selection of material and orientation is crucial for exploiting the full lightweight potential of composites [9].

Further mass-savings, when using composites in a structure, can be achieved through topology optimization. For example, it has been reported that considerable weight reduction can be attained through "black-metal" solutions, which involve deriving composite structures from former metallic ones through topology optimization [9].

However, "black-metal" solutions often fail to fully exploit the strengths of composite materials, particularly their directional strength along the fibres. Hence, the structure and material must be designed concurrently to produce composite parts tailored to specific loads to achieve true optimality. Unlike "black-metal" designs, which rely on predefined topologies and simplifications in material behaviour, optimal solutions include simultaneous consideration of structure and material without prior assumptions [9].

Figure 2.6 shows the difference in the optimization results of isotropic material, quasi-isotropic and "steered" unidirectional (UD) composite materials. We have tensile modulus $E = 62,000$ MPa for the isotropic case, which is aluminium in this case. For the carbon-epoxy quasi-isotropic laminate, we have $E = 69,671.15$ MPa. Lastly, $E_x = 181,000$ MPa is the tensile modulus along the fibre direction for the steered UD carbon epoxy composite.

For the same mass of all structures, the compliance and maximum displacement magnitude are significantly reduced when the isotropic metallic structure is replaced with composite ones. As seen, the quasi-isotropic solution is 42% stiffer than the aluminium solution. In comparison, the steered unidirectional material solution is 74% stiffer than the aluminium solution and 63% stiffer than the quasi-isotropic one. In addition, the steered unidirectional material solution has a maximum displacement magnitude 73% lower than the aluminium solution and 60% lower than the quasi-isotropic solution [15].
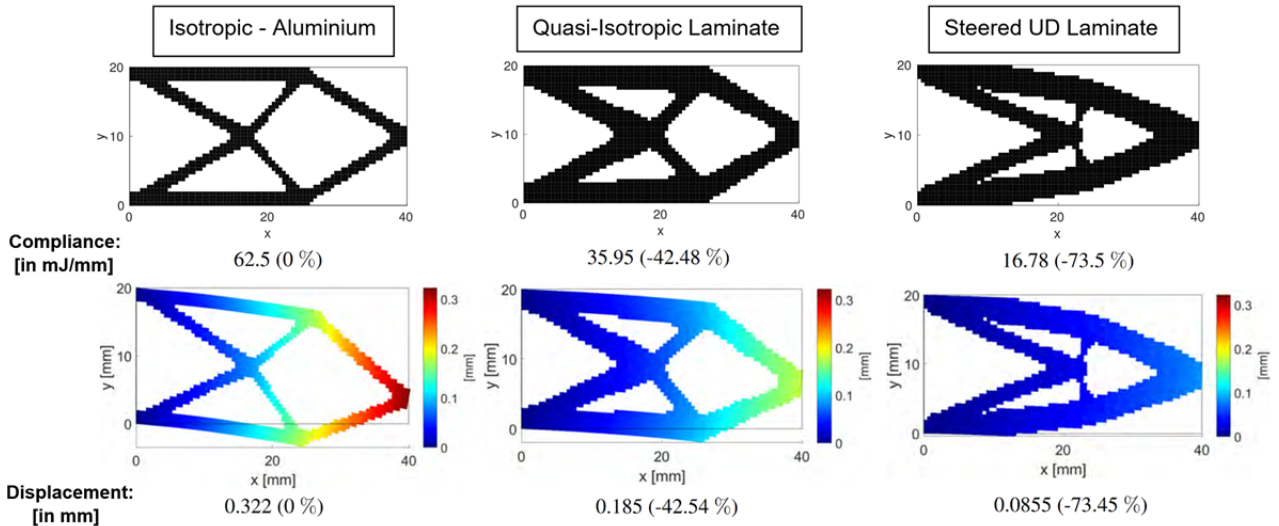


**Figure 2.6:** For three different optimization cases with (Left) aluminium as the isotropic material, (Middle) a carbon-epoxy quasi-isotropic layup, and (Right) a steered Unidirectional carbon-epoxy layup, the compliance and deflection of the three resultant topology optimized structures are reported and compared. Compared to aluminium and a quasi-isotropic layup, the steered UD materials give the best optimization results with 74 and 42% lower compliance and 73 and 60 % less displacement. Steered UD approach to TO benefits from each microstructural element being free to orient itself along the optimal direction [15].

Steered UD laminate in Figure 2.6 achieves this significant improvement through the high design freedom to orient fibre orientations along the most optimal direction. In this case, the fibre orientations are allowed vary throughout the structure, enabling optimal orientation for maximizing stiffness wherever the material is placed in the optimized structure. This steered optimization is achieved using the technique of fibre angle optimization (FAO) applied to the SIMP approach to topology optimization. Hence, such an approach is often used to design topology-optimized composite structures for fabrication through Additive Manufacturing (AM) techniques.

## 2.3. Fibre-Angle Optimization

In the literature on fibre-angle optimization or orientation optimization, several approaches have been developed and reported: Discrete Material Optimization (DMO) [16], Continuous fibre Angle Topology Optimization (CFAO) [17], tensor field variables [18], topological derivative [19], and discrete-continuous parameterization (DCP) [20], [21]. A detailed review of all the approaches mentioned can be further referred to in the review paper by Gandhi and Minak [22]. Of these, CFAO and DMO are the most widely used approaches studied for composite laminate optimization [23] in literature, and hence discussed here.

Continuous fibre angle optimization is an approach that assigns a design variable directly to each finite element, which represents the fibre angle orientation in the orthotropic materials. By relaxing the constitutive stress tensor in the design space, CFAO enables a larger design space. It has been successfully applied to optimize the orientation of stacked laminae in composite structures and achieve minimum-weight designs for laminated composite beams in wind turbine applications as in Blasques and Stolpe [17].

For more non-laminate-based optimization like FRPC structures with oriented microstructures, early use of CFAO was reported by Jia et al. [24], where SIMP was combined with an additional orientation design variable for topology-optimization of highly oriented composite structures. Post that, several other studies like Jiang et al. [25] and Almeida [6] used the CFAO approach in their fibre angle topology optimization (FATO) framework for designing 3D and 2D TO designs with carbon-fibre and natural fibre composites respectively. However, despite CFAO's prowess to generate continuous fibre paths, it is reported to face challenges such as getting stuck in local minima [18]. Hence, alternative ways to deal with local optima problems of CFAO must be explored to optimize composite designs and structures to be built using AM.

Discrete Material Optimization, on the other hand, initially designed for optimizing material angles in stacked composite ply laminates by Stegmann and Lund [16], was also developed to address the challenges associated with the local minima solutions encountered in CFAO. It solved the local minima issues of CFAO by restricting the angle options to a predefined set, commonly including angles like 0, 45, and 90 degrees, and in the process, reducing the risk of inaccurate results. DMO, for FAO, is essentially a multi-material model where each element is assigned $m$ design variables representing $m$ angular orientation. This simplifies the optimization process and improves fibre-orientation optimization within the laminate.

However, despite DMO resulting in locally optimal design without local minima issues, it might not be suitable for continuous fibre-path generation. This is due to the discrete orientation values in each finite element, which makes generating continuous fibre paths difficult. Ideally, one could use more discrete angles to obtain better continuity. However, increasing discrete options would also lead to computational complexity and convergence problems. This computational complexity arises from the DMO approach's need to compute gradients for $m$ design variables per finite element. With $m \times N$ design variables, DMO uses $m$ times the design variables used by CFAO [18].

## 2.4. Eco-design and Topology Optimization

### 2.4.1. Environmental Impact of Composites

High-performance composites such as carbon and glass fibre composites help create lightweight structures that reduce fuel consumption and emissions during an aircraft's use phase. How-

ever, producing these composites requires a significant amount of energy and the matrix used is derived from petroleum-based sources, which impact the environment as well [13]. Regarding manufacturing such composites, additive manufacturing allows for the creation of complex designs, which would be otherwise difficult or impossible to achieve with conventional manufacturing techniques. However, it is an energy-intensive process that causes further environmental impacts. In a nutshell, the environmental impact of these composites is present at every stage of their life cycle, including raw material sourcing, production, manufacturing, use, and end-of-life disposal.

A way to evaluate this impact, often cited in the literature, is Life-cycle Assessment (LCA). LCA is a tool that quantifies and characterizes the environmental impact of commercial products, technologies, or services throughout their entire life cycle. LCA can be used to evaluate the impact of using composite materials on an aircraft. However, to use this environmental impact information of composites for designing more eco-efficient solutions, the concept of eco-design can be implemented. Eco-design is a methodology that incorporates environmental considerations into the design and development of products to minimize their negative environmental effects while ensuring that essential factors like functionality, quality, and cost are not compromised [26]. Thus, LCA can be viewed as a tool that aids in realizing the concept of eco-design for a product by providing the designer and the stakeholders with the potential impact quantification of all the components of the product through their various life-cycle stages [27].

Generally, the LCA of a product or a process can be carried out by evaluating different environmental impact parameters like terrestrial acidification, ozone depletion, land use, water consumption, Global Warming, etc. However, since the data for all such indicators is not well well-documented, it is often impossible to conduct a detailed LCA study. However, given that the aviation sector's growing contribution to the climate change crisis is primarily from jet fuel combustion, often only a carbon footprint assessment is done for eco-design studies that implement LCA for evaluating material choice [13]. Furthermore, materials like composites have significantly more documented $CO_2$ footprint data than other environmental impact parameters.

## 2.4.2. Eco-efficient topology optimized structures

Topology optimization of composite structures can be viewed as an eco-design task in itself, where each kilogram of structural mass saved due to structural optimization results in substantial fuel savings over the operating life of mobility solutions like automobiles, aircraft, launchers, etc. However, it does not directly consider the environmental impact of materials used to optimise the structure. Neither does it consider these materials' manufacturing or processing impact on the part's overall environmental impact.

Since material, process, and design selection aspects of structural design are coupled, the environmental assessment requires a more multidisciplinary design optimization approach to achieve optimum and sustainable results. Where the environmental impact minimization for the structure is achieved while fulfilling the functional and technical requirements [28]. Building upon such an ideology and to eco-design the process of TO in a fast and efficient manner, Duriez et al. [29] developed a method to "simultaneously select the optimal material, process, and design of an additively manufactured structure". The Ashby index was used in their work to achieve this simultaneous material-process-design optimization.

Using the Ashby index allows for decoupling material and topology optimization. This enables individual evaluation of the material and the structure. Thus, by only minimizing the Ashby index in Equation 2.3, the objective function, in this case, $CO_2$ footprint, can also be minimized. This is achieved independent of the other variable terms related to the optimization of topology $(f(V_f)V_f)$ in the objective definition [29] seen in Equation 2.3.

$$CO_2^{\text{tot}} = \frac{LhF}{\delta_{\max}} \frac{\rho}{E} f\left(V_f\right) V_f \times \left(CO_{2,mat}^i + L_{veh} \times CO_{2,veh}^i\right)$$
$$Ashby\ Index = \frac{\rho}{E} \times \left(CO_{2\ mat}^i + L_{veh} \times CO_{2,veh}^i\right)$$

(2.3)

Where $L$ and $h$ represent the length and height of the Ashby beam being optimized. $\delta_{\max}$ is the fixed constraint on the maximum deflection of the beam, and $F$ is the external load applied. The material's Young Modulus and density are $E$ and $\rho$, respectively. The compliance of the optimized topology is represented by $f(V_f)$ for an occupied volume fraction $V_f$. Lastly, the terms in the bracket for the Ashby index are the $CO_2$ intensities for different life-cycle phases of the Ashby beam. It includes $CO_2$ intensity for raw material production $(CO_{2,mat}^i)$ and the part's use phase on a vehicle $(CO_{2,veh}^i)$ over $L_{veh}$ kilometres travelled, respectively.

In their work, Duriez et al. [29] minimize the $CO_2$ impact of a structure, starting by short-listing the best material-manufacturing process pairings from a larger database. This is done by assessing which pair most reduces the $CO_2$ impact index part of the objective function. A Pareto front optimization approach is utilized to evaluate this in multiple steps until a limited number of pairs remain. Then, the topology for the remaining optimal materials and manufacturing pairs is optimized. Lastly, to determine the best material-process-design combination for a given problem, further evaluation of the total $CO_2$ impact for the designs generated for the remaining pairs is done.

However, this study by Duriez et al. [29] is limited to considering isotropic materials manufactured using AM. As a result, in a subsequent study, Almeida [6] extended this eco-design for the TO framework developed to include anisotropic materials. Unlike in [29] though, the $CO_2$ impact in [6] is evaluated only post-optimization and not during the optimization.

## 2.4.3. Limitations of Eco-efficient Topology Optimization Framework
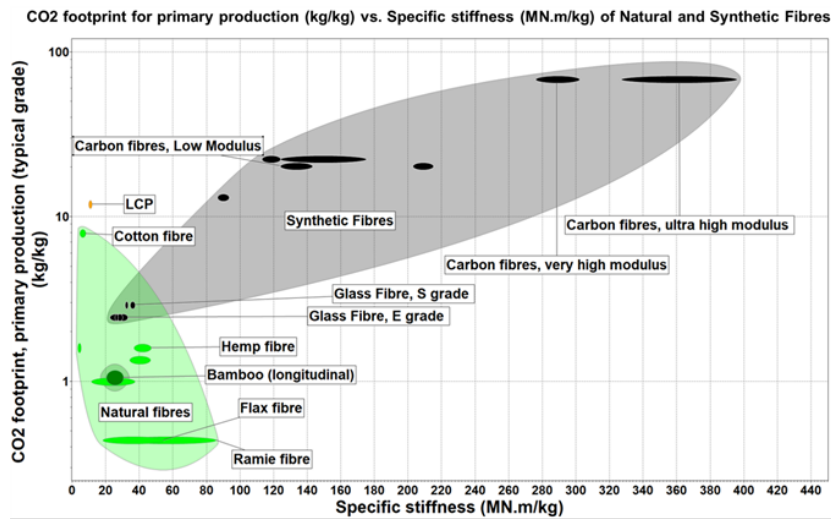


**Figure 2.7:** Ashby plot comparing the natural fibre and synthetic fibre's embodied $CO_2$ footprint and specific stiffness, showing the embodied $CO_2$ footprint of natural fibre being much lower compared to synthetic fibres.

Almeida [6], in his work on single-material topology optimization, looks at optimizing transport structures made from natural fibre-reinforced composites or NFRPCs. The aim is to reduce the environmental impacts of otherwise conventional transport structures designed from petroleum-based polymers and other metallic materials. This is achieved by replacing them with low-density natural fibre-reinforced composites with a low $CO_2$ footprint compared to synthetic fibres, as seen in Figure 2.7.

In an attempt to realise this objective of more sustainable composite structures, SIMP was implemented with CFAO and combined with an LCA-based material selection process. Such an implementation resulted in 50% bamboo fibre in cellulose matrix as the composite material with the lightest weight and the least $CO_2$ footprint. The results for this optimization can be seen from Figure 2.8a.

However, the compliance (24.7 J) for the bamboo-cellulose NFRPC is almost two times of 50% flax fibre in the cellulose matrix (13.4 J). This is despite the intermediate density design variable values for the flax-cellulose composite as seen in Figure 2.8b, which probably results in higher compliance than achievable for an equivalent discrete design. The $CO_2$ impact, on the other hand, is approximately 50% lower for the bamboo-cellulose combination when compared to the flax-cellulose combination.



**a** 50% Bamboo Fibres in Cellulose Matrix   **b** 50% Flax Fibres in Cellulose Matrix

Compliance: 24.692 J
$CO_2$ Footprint: 45,001 kg $CO_2$/kg

Compliance: 13.416 J
$CO_2$ Footprint: 65,505 kg $CO_2$/kg
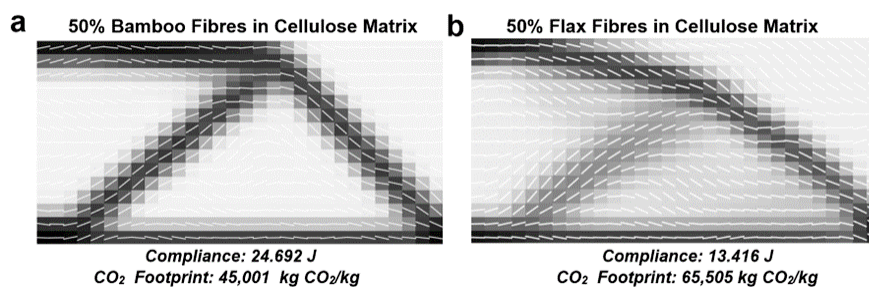
**Figure 2.8:** Topology obtained, along with the compliance and $CO_2$ footprint when optimizing for a composite material constituting (a) 50% bamboo fibres in cellulose matrix, (b) 50% flax fibres in cellulose matrix. The results are reproduced using the CFAO strategy as developed by Almeida [6]. Comparing the $CO_2$ impact and compliance for the two designs, for a stiffness difference of 18 GPa (28.4 - 10.4 GPa) between the two composites, a compliance difference of almost two times, and a $CO_2$ impact difference of approximately 50% is achieved.

The stiffness difference of 18 GPa between the two fibres explains the difference in compliance obtained for the two structures when the same design volume fraction of 0.3 was used. The density of bamboo fibres, on the other hand, is less than half that of flax, i.e., 700 $kg/m^3$ compared to 1470 $kg/m^3$, resulting in a structure with lower mass than flax fibre.

This gain in one objective at the cost of another is unfavourable when the objective is to optimize both the compliance and the $CO_2$ footprint. Such a simultaneous optimization of multiple objectives often requires a trade-off among these objectives. Tools like Pareto Front can help to achieve a smart trade-off without exploring the full range of every parameter.

In aviation, however, stiffness or rigidity requirements trump the eco-design aspect strictly based on functionality. Increasing the stiffness of the bamboo-cellulose structure by increasing its volume fraction could be possible, but that would lead to an increase in mass, which would increase the $CO_2$ footprint of the structure. When looking at aviation, the use phase or the aircraft's operational life contributes the most to carbon emissions [13]. In this case, increasing mass does more harm. The emissions due to the burning of jet fuel to carry 1 kilogram of

extra mass over the aircraft's lifetime would be significantly higher. To emphasise the impact of 1 kilogram of extra mass, Duriez [13] in his work estimated that we could save 25.8 tons of kerosene over a long-distance aircraft's life just by saving 1 kilogram of mass and 3.83 tons of $CO_2$ emissions can be prevented by saving one ton of kerosene.

As established, optimized compliance is also important and must be considered when a specific stiffness is required for part design. Hence, in order to obtain a good compromise between stiffness and minimizing carbon dioxide emissions, it is suggested that studying the effects of a multi-material structure made up of different combinations of natural fibres and synthetic fibres could be beneficial.

## 2.5. Multi-Material Topology Optimization

The motivation to opt for printing multi-material topology optimized structures is supported by the results of the study carried out by Roper et al. [30] and Zuo and Saitou [31]. In the study by Roper et al. [30], a three-material system containing both isotropic and anisotropic materials, i.e. metals and composites, is simultaneously optimized along with the topology to design aircraft seats. This results in a structure with higher specific properties than its single-material topology-optimized counterpart.

The other study on multi-material topology optimization (MMTO) by Zuo and Saitou [31] showed optimization results with an MMTO structure performing worse than a single-material topology optimized (SMTO) structure. This was obtained for a single mass-constrained TO problem. However, it also demonstrated that their MMTO approach can yield beneficial results when optimizing for a system comprising both materials with inferior specific properties and materials with high specific properties. This was true for a multi-constraint optimization case, with cost and mass constraints.
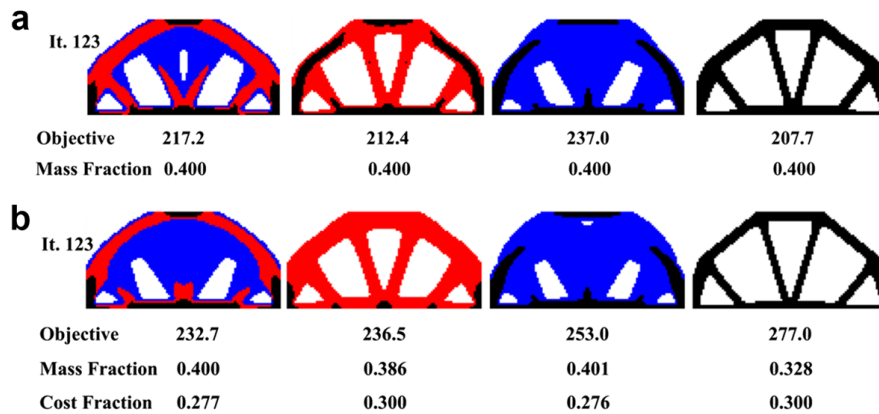


**Figure 2.9:** For a three-material system with stiffness-to-density ratio of $material\,C > material\,B > material\,A$ and cost-to-density ratio of $material\,A > material\,B > material\,C$, (a) Optimizing with mass constraints results in the structure that uses only the stiffest material, C (Right), to have the lowest objective value, while (b) optimizing with mass and cost constraints results in a structure where all three materials (Left) are used to have the lowest objective value [31].

When optimizing for a three-material system material with a stiffness-to-density ratio of $material\,C > material\,B > material\,A$ and cost-to-density ratio of $material\,A > material\,B > material\,C$, with only mass constraints, results in the structure where only the stiffest material C is used to have the lowest objective value of 207.7, and the structure consisting of all three materials to have a higher objective of 217.2. This difference in results for when MMTO performs worse than SMTO can be seen in Figure 2.9a. As expected, a structure with

only the highest stiffness-to-density ratio material for the same mass constraint shows better results. Similarly, optimizing for the same three-material system material but with mass and cost constraints of 0.3 and 0.4, respectively, results in the structure where all three materials are used to have the lowest objective value of 232.7, and the structure consisting of only material C to have a higher objective of 277. This difference in results for when MMTO performs better than SMTO can be inferred from the plots for leftmost and rightmost cases in Figure 2.9b. While the exact reason for this was not justified in their work, we assume that in this particular instance, the superior performance of the MMTO structure in comparison to the SMTO structure could be partially because the SMTO structure has a lower mass fraction of the stiffest material, thus resulting in lower stiffness.

This emphasizes that whether MMTO can outperform SMTO depends on the stiffness of the materials being considered, their spread and the set of objective(s) and constraint(s) for which the problem is being solved. Nonetheless, if we were to optimize for a less extreme case with three materials that have stiffness-to-density ratio according to $material\,C > material\,B > material\,A$ and cost-to-density ratio of $material\,C > material\,B > material\,A$, then an overall lower objective could surely be achieved when mass and cost constraints are used simultaneously. Based on this information, it is hypothesized that we could achieve a better compromise between $CO_2$ footprint and stiffness for a structure by simultaneously optimizing materials that improved either compliance or $CO_2$ footprint by tweaking our objectives and constraints.
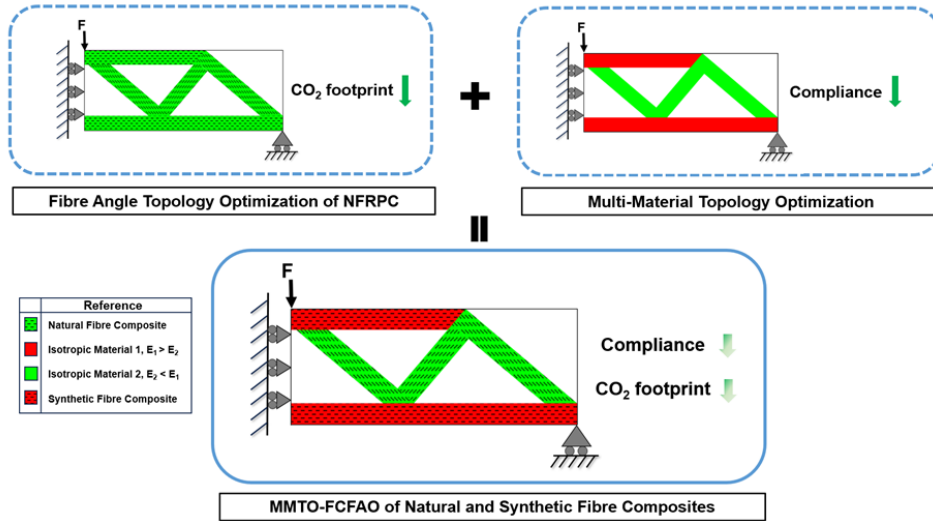


**Figure 2.10:** Hypothesis showcasing the potential benefits of combining the approach of optimizing single natural composite material using SIMP-modified with CFAO, which results in the reduction of $CO_2$ footprint [6], and a multi-material system with multiple constraints that can potentially improve the overall compliance [31]. Combining these approaches has the potential to yield composite structures that effectively minimize both $CO_2$ emissions and compliance simultaneously to a great extent.

This hypothesis can be illustrated in Figure 2.10. It can be seen that optimizing a single natural composite material using SIMP-modified with CFAO approach as done by Almeida [6] allows us to obtain structures with a significantly low carbon footprint. On the other hand, a multi-material system, as developed in the case of Zou and Saitou [31] with multiple constraints on mass and cost, can improve the overall compliance of a structure. If we were to combine such approaches, it could lead to a structure that can substantially reduce both the $CO_2$ footprint and the compliance of a composite structure. However, to implement and prove this hypothesis, it is imperative to develop a framework that can simultaneously optimize multiple materials and fibre angles in the same design domain using topology optimization.

## 2.6. Concurrent Multi-Material Fibre-Angle Topology Optimization

Only limited studies in the literature have applied the concepts of orientation optimization and multi-material topology optimization simultaneously. Two such studies are by Duan et al. [32], and Chandrasekhar et al. [33]. Both the studies also used different optimization techniques, a mesh-based topology optimization and a mesh-free topology optimization approach using neural networks (NN).

The first one is by Duan et al. [32], where a discrete material optimization (DMO) approach is used for both material selection and fibre angle optimization. Two different composite materials, carbon fibre-reinforced polymer (CFRP) and glass fibre-reinforced polymer (GFRP), are used. Three types of design variables per element of the finite element mesh are used to optimise for these two materials. Two of these design variables are used to optimize the macro-scale topology, where one is used to determine if the material exists in the finite element and the other one to determine which material provides maximum stiffness. The last one is to optimize the micro-scale fibre orientations. Together, they determine the macroscopic constitutive element matrix of the $j-th$ element in the $i-th$ layer of a multiple-ply laminate. This two-scale model is combined to form the 'Multi-scale and multi-material composite anisotropic penalization' (MMCAP) approach.

Figure 2.11a,b and c show results of the MMCAP framework for different candidate fibre angles and design domains. 2.11a and b show the results for Messerschmitt-Bölkow-Blohm (MBB) beam and 2.11c for L-shape beam. As seen in Figure 2.11b, with more candidate angles, the topology changes to provide better stress distribution and a more optimal solution. However, due to the smaller number of angles that are used for optimization, non-continuous fibre paths are obtained. As established earlier, increasing the number of candidate fibre directions using DMO significantly increases computational complexity. This complexity, however, can be reduced by using explicit curve functions as described in [34].
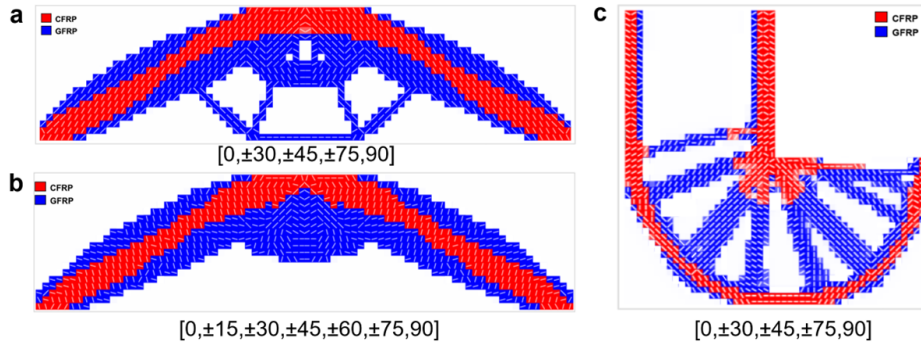


**Figure 2.11:** (a) and (b) Results obtained for an MBB beam optimized multi-material topology obtained for the given set of fibre angles using the two-scale model developed by Duan et al. [32] depicting how more number of candidate fibre orientations, improve the design and stress distribution with less discontinuous fibre sets, (c) Results obtained for L-shaped beam optimized multi-material topology obtained for the given set of fibre angles using with non-optimal fibre orientations and complex manufacturability.

Another study that implemented a form of multi-material topology optimization approach to composite materials is the work by Chandrasekhar et al. [33]. In their work, multiple materials are optimized through an MMTO framework on a macro scale and a continuous fibre-angle optimization approach on a micro-scale. However, this work uses a neural network to capture the matrix topology, fibre orientation, and fibre density instead of assigning design variables to individual elements like in Duan et al. [32].

$$J = 2.08 \; ; \; m^* = 600 \; ; \; V_f^* = 0.25$$
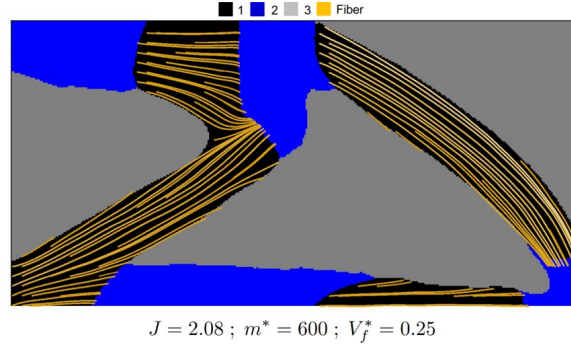
**Figure 2.12:** A continuous fibre angle topology optimization approach based on neural networks, with the use of an extra isotropic phase (2-blue) as done in the study by Chandrasekhar et al. [33], showing the potential of the approach to optimize multi-material structures. Continuous fibre paths with spatially varying fibre densities and isotropic materials at intersections. The long fibres are indicated in yellow, the base matrix is in black, and the voids are in grey.

To obtain multi-material structures with fibre-reinforced material and isotropic matrix, the following topological formulation is used, $\zeta(\mathbf{X}) = ((\rho_{m_1}, \rho_f,), \rho_{m_2}, \ldots, \rho_{m_n}, \rho_{m_\phi})$. Where, from the $n$ matrices to be optimized, only one of the base matrices (M1) is set to be a fibrous matrix and $m_\phi$ as void. The remaining matrices are set as isotropic matrices with matrix densities $\rho_{m_2}, ..., \rho_{m_n}$. For M1 we have $\rho_{m_1}$, $\rho_f$ and $\theta$ as the matrix density, fibre density and fibre orientation design variables, respectively.

Figure 2.12 shows an MMTO structure optimized for a combination of a long fibre-reinforced matrix (M1) and a non-reinforced matrix (M2) with fibre density of $V_f^* = 0.25$ and a maximum allowed mass $m^*$ of 600. As observed, the framework can achieve continuous fibre paths with spatially varying fibre densities, indicated by the yellow lines. This attribute is better for the manufacturability of the optimized parts using AM when compared to the results of the previous study by Duan et al. [32]. Furthermore, an optimized distribution of isotropic material is also observed, highlighted in blue.

## 2.7. Research Scope

As seen from the work of Duriez [13], eco-efficient designs can be achieved by coupling an LCA-based material selection decision-making step with the design optimization step in topology optimization. This approach designed for optimizing isotropic materials at a multi-scale level further opened up opportunities to include orthotropic materials like composites and assess their impact on the environment. This was explored in the work of Almeida [6]. However, obtaining an eco-efficient TO design using only NFRPCs that also meet structural requirements like high stiffness is an uphill task. This is true especially when using only single materials that are either low density and low $CO_2$ impact or low density and high $CO_2$ impact. As a result, it is hypothesised that an overall better design can be achieved by combining multiple materials within the same structure, leading to lower carbon emissions of a component over its lifetime and a sufficiently high stiffness.

It was determined that doing so would require a framework that optimizes fibre orientations as done in [6], while distributing a combination of multiple materials in the same structure as done in [30]. However, not many multi-material topology optimization studies in literature studies incorporate both anisotropic material properties and fibre path generation steps in the optimization phase. Ones that do consider it [16], [32], [33] however, are not optimized to integrate continuous fibre paths in an all-anisotropic multi-material topology optimization study.

Interestingly, the study by Chandrasekhar et al. [33] comes closest to solving a real-life multi-material topology optimization problem. It optimizes for a mix of isotropic and anisotropic continuous fibre composite materials like in most aircraft and space vehicles, which are not all composite structures. However, the approach used in their study to obtain an optimized solution differs from other mesh-based topology optimization (TO) approaches. Instead of using the traditional method with finite element mesh, neural networks were employed. This approach has the potential to provide crisp topology boundaries by implicit filtering and quicker convergence for simple TO problems. However, the added complexity of working with neural networks is foreseen to cause issues when modifying the framework to meet the objectives of this work.

Based on the context and supporting literature, it is safe to assume that an easy-to-implement, gradient-based, unified framework for MMTO and fibre angle optimization is lacking. While Duan et al. [32] meets some of these requirements, it does not optimize structures with continuous fibre paths. A continuous and well-optimized fibre path is often necessary to avoid stress concentrations in the optimized structure. The same also allows more design freedom for optimizing the topology itself owing to the exploitation of the anisotropic properties of the material in all directions [22]. Hence, combining a continuous fibre angle topology optimization approach with a multi-material TO approach can be deemed a promising step in realizing new design avenues where integrated, topology-optimized, multi-material designs greener aerospace structures.

With this information and review of the state-of-the-art, we can formulate research sub-questions for this work that help us to answer the main research question, ***How can multi-material optimization be applied to design eco-efficient composite structures?***
1. How can a multi-material topology optimization framework be coupled with a fibre orientation optimization model to obtain manufacturable designs?
2. What impact does using multiple composite materials in the same structure have on the compliance and $CO_2$ emissions over its lifetime?

Where the first question helps us address the research gap identified concerning the lack of an MMTO framework that optimizes fibre orientations. The second question helps us to determine the validity of using multi-material systems to address the $CO_2$ footprint of optimized structures.

To answer these questions, a more in-depth review of existing approaches to multi-material topology optimization and fibre angle optimization is required. Furthermore, some design choices for the building blocks of a topology optimization framework must be made. This includes design choices for objectives, constraints, finite elements method, regularization schemes, optimization algorithms, and the material interpolation scheme. These choices can be made based on some basic requirements for a good optimization framework such as, functionality, robustness, computational efficiency and ease of use.

# 3

# Optimization Framework Requirements and Choices

## 3.1. Optimization Framework Design Requirements

The primary objective of the framework is to optimize the topology and orientations of multiple orthotropic materials simultaneously for thin 2D structures in order to minimize compliance or maximize stiffness. We assume that we can achieve this objective fairly by combining existing models. However, designing structures that can be easily produced using AM techniques is not straightforward, and we need to define such requirements in more detail.

In order to meet the AM reproducibility or manufacturability aspect, the design obtained from the developed framework must be easy to manufacture without significantly altering the optimized topology. A basic manufacturability criterion of the optimized design is assumed to be met if we can maintain fibre angle continuity throughout the structure, avoid material mixing at the interfaces between multiple materials, and ensure a minimum feature size for each material at the end of the optimization. Assuming that these manufacturing criteria can be incorporated within the framework, it is also essential to evaluate the computational efficiency of our framework, an attribute essential for a good topology optimization framework.

The framework's computational efficiency is determined by its scalability in terms of increasing design variables for optimization. Hence, to have comparable or acceptable optimization times for the coupled framework, we must consider this requirement in all our design choices from the outset. Nonetheless, the framework must be robust to varying inputs and evaluation criteria, regardless of the computational efficiency. The overall computational prowess of the framework is viewed as something that can be bettered with subsequent modifications to the framework, provided that all other requirements outlined are met sufficiently.

In this work, we define robustness as the ability of the framework to provide repeatable or reproducible convergence of results when optimized for different initial guesses. Hence, as a requirement, the optimization results must converge for all primary input variations, such as domain size, number of finite elements, material properties, and feature size inputs.

Lastly, the framework must be easy to implement and easy to use. This is another important trait of a good topology optimization algorithm. The user should be able to give minimum inputs to the system without performing extensive parameter tuning and still achieve an acceptable output that can be worked with directly at the end of optimization.

19

Based on these established requirements of functionality, efficiency, robustness, and ease of use, we can dive deeper into the literature to make design trade-offs for different aspects of topology optimization, such as optimization algorithms, filters, interpolation schemes, penalization approaches, constraints, objective definitions, etc., and make design considerations to ensure that the aforementioned requirements can be met.

# 3.2. Design Choices for Framework Development

A robust, functional, efficient and easy-to-implement framework combining fibre angle optimization and multi-material topology optimization is required as established. Several design choices must be considered to build such a framework. However, given that some of the requirements mentioned earlier can conflict, literature and intuition-based trade-offs must be conducted to evaluate these factors and make design choices for all the necessary building blocks of a topology optimization problem described earlier in Section 2.1. This exercise might not result in the best possible solution, but it would definitely help us develop a good framework design that tries to address all the requirements appropriately.

## 3.2.1. Optimization Objective and Constraints

The most rudimentary design choice for the optimization process involves deciding the objective and constraints crucial to designing the rest of the framework components. As stated earlier in one of the research objectives, we need a topology-optimized structure with high stiffness or low compliance and a low $CO_2$ footprint. Both low compliance and low $CO_2$, as objective parameters, conflict because, more often than not, for existing engineering materials, one comes at the cost of the other. This was also seen from the Ashby plots in Section 2.4. As a result, a trade-off, in this case, could be to fix one of these as the objective function and optimize the other parameters through constraints. This would not give the optimal solution for both minimum compliance and minimum $CO_2$ design but ensure a more optimal solution than currently possible with the framework described in the work of Almeida [6].

The compliance C to be evaluated can be given by the material's global stiffness matrix **K** and displacement vector **U** as shown in Equation 3.1. This representation is the same as derived in the work of Stegmann and Lund [16] for the TO of composite materials.

$$C = \mathbf{U}^{\mathrm{T}}\mathbf{K}\mathbf{U} = 2 \times strain\ energy \tag{3.1}$$

Once compliance is chosen as the optimization objective, for our constrained optimization, the required constraints can be either volume or mass constraints. We established that a low overall structural mass and significantly higher specific stiffness of the materials within the structure is key to obtaining a lower $CO_2$ footprint. This low mass for a high-performance requirement directly translates into using low-density, high-stiffness materials. The high specific stiffness means that, overall, less material is required in the design space. We can also reduce the mass by further restricting the occupiable design space. Combining these, higher mass minimization and higher performance can be simultaneously achieved by maximizing low-density, high-stiffness materials within this less-occupied space.

A simple and effective way to distribute these high-specific stiffness materials is by adjusting the volume parameters of different materials in the design space. In doing so, we can ensure that a low-density material occupies the maximum volume within the occupiable domain. However, since not all high-specific stiffness materials have a low material carbon footprint, for instance, carbon-fibres as seen from the Ashby plots in Section 2.4, volume constraints can

allow us to manually allocate some share of this occupiable design space to materials with not necessarily the best specific stiffness but with the lowest embodied $CO_2$ footprint. By having that freedom, we can attempt to evaluate material combinations and proportions that can give us both high stiffness and low $CO_2$ footprint.

There are three ways to apply the volume constraint, as illustrated in Figure 3.1b-d. The first method uses a single volume constraint to control all candidate materials, allowing each material to be placed anywhere within the design domain following all materials are available to be optimized throughout the domain as illustrated in Figure 3.1a (Left). On the other hand, the second method uses individual volume constraints for each material, where each material is only available for optimization within an exclusive subdomain of the entire design domain following the material domain restriction as seen in Figure 3.1a (Right). The third and final method uses individual volume constraints for each material, but again, each material is available for optimization throughout the entire design domain.
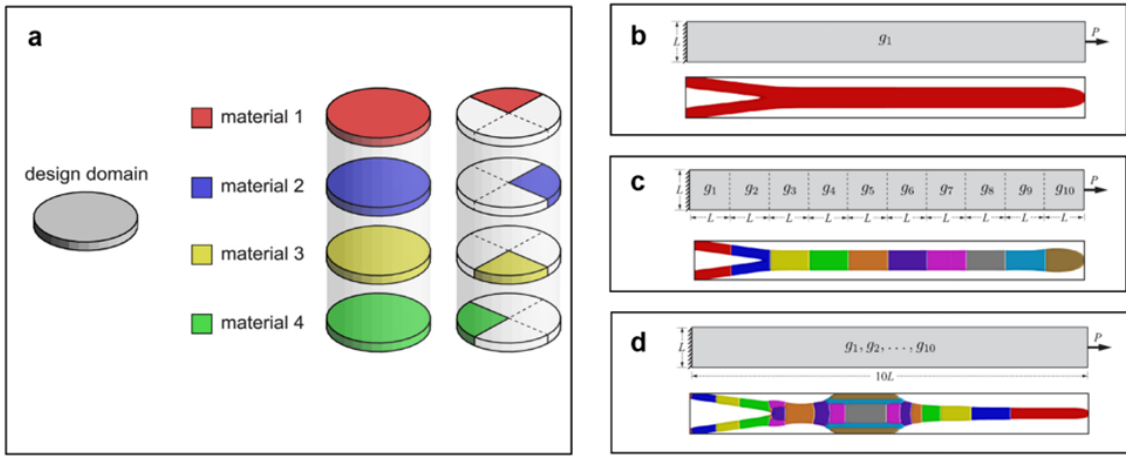


**Figure 3.1:** (a) For an MMTO problem, the material can be optimized in the design domain with all the materials being allowed to occupy the entire design domain or with each material occupying a specific sub-domain in the design. For a load case where a cantilever beam is subjected to an axial load, the MMTO results obtained, when using (b) a global volume constraint where the materials are allowed to exist throughout the design space, only the stiffest material is chosen. When using (c) 10 equal volume constraints for each material, and each material allowed to occupy separate sub-domains, similar topology to (b) are achieved but with fixed material in different regions. Lastly, when using (d) 10 equal volume constraints but with all materials allowed to occupy the entire design domain, give less intuitive and different material distribution and topology [35].

In the context of this work, the optimizer should be free to choose where each material should be placed rather than having it predefined by the user, as done in the second case shown in Figure 3.1c. This gives us more design freedom to generate less intuitive designs without excessive user control, like in Figure 3.1d.

An argument for and against mass constraints can be understood from the findings of an MMTO study by Gao et al. [36]. Their work showed that mass constraints give better results than volume constraints and are more relevant to engineering problems. However, this is only when compliance minimization is considered. When using only mass constraint, it is possible that with conflicting objective optimization, only one optimal material appears in the final result. Given that this work aims to evaluate how much improvement in overall $CO_2$ footprint can be achieved by including varying amounts of material with low embodied $CO_2$ footprint, such a consequence is not desirable.

Hence, an informed decision to persist with volume constraints is taken. From literature and practice, volume constraints are often easy to implement, and the resultant framework can be verified better as we can generate more data on the optimization's evolution for different volume fractions of different materials in the same structure. Thus, considering volume constraints gives us more control over tuning the obtained $CO_2$ footprint of the optimized structure while simultaneously checking the compliance evolution.

Alternatively, simultaneous minimization of mass and compliance could also be realised through a multi-objective topology optimization approach using Pareto fronts similar to the work done by Duriez, [13]. Nonetheless, this work does not explore this approach because the number of optimizations needed to be evaluated to obtain meaningful results is expected to be quite high.

Having decided on the primary objective and constraints for our optimization approach, we must decide on the approach to each of the two individual components of the multi-material fibre angle topology optimization (MM-FATO) framework. Once we make a choice, we will have the design variables that the optimization algorithm will work with to minimize the objective function of the MM-FATO framework.

## 3.2.2. Fibre Angle Optimization Scheme
Fibre angle optimization, as seen earlier, allows users to optimize orthotropic materials more efficiently compared to a simple material optimization with no orientation or fibre angle optimization. By optimizing fibre orientations as design variables, improved results with better optimization of the highly directional orthotropic material along the path of maximum strain can be achieved.

As seen previously, between CFAO and DMO, continuous fibre angle optimization or CFAO is a better approach to optimize such independent design variables for fibre orientations. The advantage of this approach is its potential to generate designs with spatially continuous fibre orientation, which is essential for AM reproducibility [22]. Duan et al., [32], one of only a few studies that implement fibre angle optimization for structures consisting of multiple orthotropic materials, in their work, use the Discrete Material Optimization or DMO approach proposed by Stegmann and Lund [16]. However, the designs obtained using their approach resulted in discontinuous and difficult-to-fabricate designs when AM is considered. As a result, CFAO for fibre angle optimization is discussed further and selected for optimizing fibre angles in this work.

CFAO, however, also comes with its own shortcomings. As frequently reported, these include the susceptibility of the approach to fall into local minima given its high dependence on the initial guess of orientation design variable. This issue can be addressed in multiple ways for this work. First, a filtering approach can reduce the chances of some orientation design variables falling into local minima at the start and during optimization. Second, the issue specific to strong influence on an initial guess can be further addressed by the use of a combination of multi-start and parallelization approaches for a uniform fibre field initial guess, which essentially acts as a global search strategy with multiple start points [7], [37]. Hence, if measures are taken to address the shortcomings, CFAO can be a suitable approach to FATO and produce manufacturable designs.

The simplest implementation for CFAO, which is easy to reproduce, is the one by Jiang et al. [25]. In their work, they use the polar representation for fibre orientation $\theta$, with the

bounds of $\pm 2\pi$ essentially allowing the fibre orientation to orient in any direction within the design space without any restrictions. However, as understood from the work of Nomura et al. [38], using such design variables might be an issue when fibre angle filtering is applied to the design variables. This orientation filtering, similar to density filtering, modifies a single orientation vector based on a linear weighted average of the neighbouring orientations in a fixed radius to obtain smoothly varying fibre orientations. Such smoothly varying fibre angles ensure a more continuous fibre path that can be readily manufactured using Automated Fibre Placement and Fused Deposition Modelling (FDM) techniques for continuous fibre-reinforced composites. This fibre smoothing can be seen from the difference in orientations at intersections that are loaded in shear between Figure 3.2a (Left) without filtering and Figure 3.2a (Right) with filtering.

This issue of incompatibility with filtering is highlighted by Nomura et al. [38] and is called $2\pi$ ambiguity. This means that, for two angles separated by $2\pi$, although they are physically the same, they are still separated by a phase of $2\pi$ in the actual design space. This can lead to erroneous optimal designs achieved, as seen from Figure 3.2b. Furthermore, if two adjacent design variables have $\theta$ with a phase difference of $2\pi$, then on filtering, this would result in an erroneous fibre angle of $\theta \pm \pi$ [38] This can also be understood from Figure 3.2c. Jiang et al. [25], in their work, did not implement any filtering and hence could avoid such an issue. However, given the benefits of implementing it and having a more generic implementation that allows for the use of in-optimization filtering without the issue of $2\pi$ ambiguity, the solution to it suggested in the work of Nomura et al. [38] and Duriez [13] can be implemented.
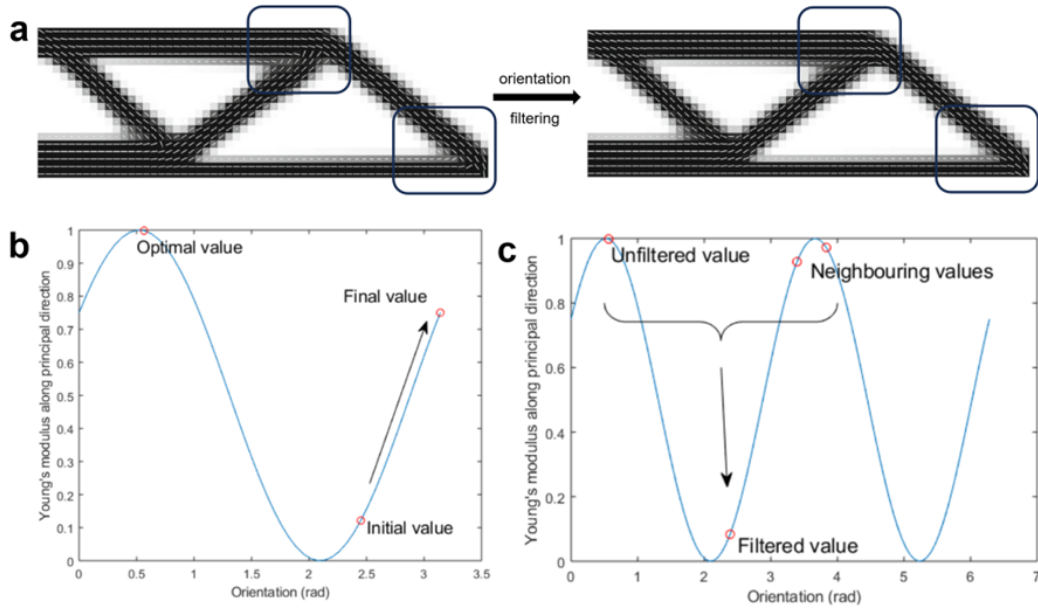


**Figure 3.2:** (a) Orientation filtering smooths non-continuous fibre orientations in regions of topologies where features with varying load path intersect or in the shear-loaded regions. (b) Periodic function like $\theta$ for orientation optimization can cause optimized results to have $2\pi$ periodicity in relation to the optimal value, depending on the initial guess, and (c) simple filtering for orientations that have neighbours with $2\pi$ periodicity will create filtered orientations with $\pi$ difference causing fibre path discontinuities [13], [39].

This suggested approach involves using Cartesian representation for the fibre orientations instead of the Polar representation, where two orientation variables $cos\theta$ and $sin\theta$ are used, which can be used to obtain the orientation in polar form using Equation 3.2. Although in most cases, as noted by Nomura et al. [38], modifying the range for optimization of $\theta$ to be $[-\pi, \pi)$, could suppress the issue, it would also prohibit design changes across the prescribed bounds due to the non-physical gap at the extremes, potentially causing local minima.

$$\theta = arctan\left(\frac{sin\theta}{cos\theta}\right) \tag{3.2}$$

The thesis of Almeida [6] used as a preceding work to the current thesis also uses CFAO, where instead of using a single fibre orientation, the Cartesian components of the design variable $\theta$ were used. The results from such an implementation indicated compatibility with in-optimization filtering, bolstering confidence in using such an approach.

In conclusion, with such a design variable definition, we can achieve simultaneous optimization of topology and orientation that results in overall smooth fibre orientations.

### 3.2.3. Material Interpolation Scheme

After fixing the approach to fibre angle optimization, the next step is to decide on the multi-material interpolation scheme. One of the primary goals of a multi-material topology optimization exercise is to distribute $'m'$ candidate materials within a design domain such that the resulting structure best minimizes the objective. We can achieve this target at the elemental level by computing the objective function as a weighted sum of the $'m'$ design variables corresponding to the $'m'$ candidate materials. In practice, it is implemented by a weighted sum of the variable term within the compliance definition, i.e., the elemental constitutive matrix $\mathbf{D_e}$, for the $'m'$ candidate materials, as shown in Equation 3.3.

$$\mathbf{D}_e = \sum_{j=1}^{m} w_j \mathbf{D}_e^j = w_1 \mathbf{D}_e^1 + w_2 \mathbf{D}_e^2 + \cdots + w_m \mathbf{D}_e^m, \quad 0 \leqslant w_j \leqslant 1 \tag{3.3}$$

The weights, in our case, can be seen as representative of the $'m'$ design variables. Consequently, we can replace the $j-th$ weight $w_j$ with $x_e^{matj}$ in Equation 3.3. These continuous design variables $x_e^{matj}$ during optimization are treated as artificial variables, where they take values between zero and one to ensure no material contributes more than the actual physical material property or contributes negatively, which does not hold any physical meaning. However, at the end of the optimization, the material cannot exist as an intermediate value since such a material property might not be reproducible in real life. To that end, a power-law-based variable penalization is employed to push the material design variables to 0-1 in the pursuit of obtaining more discrete designs that make sense [16]. This gives us a revised interpolation scheme expressed by Equation 3.4. Such an interpolation scheme falls under MMTO's 'Discrete Material Optimization' (DMO) branch [16], which will be further referred to as DMO1.

$$\mathbf{D}_e = \sum_{j=1}^{m} (x_e^{matj})^p \mathbf{D}_e^j = (x_e^{mat1})^p \mathbf{D}_e^1 + (x_e^{mat2})^p \mathbf{D}_e^2 + \cdots + (x_e^{matm})^p \mathbf{D}_e^m, \quad 0 \leqslant x_e^{matj} \leqslant 1 \tag{3.4a}$$

$$\sum_{j=1}^{m} x_e^{matj} \leq 1 \tag{3.4b}$$

Such a formulation, however, as seen in Equation 3.4b, also requires additional constraints for the weights [40]. It is fair to assume that such an additional constraint for the desired continuous fibre angle optimization framework with multi-materials could potentially over-constrain the design space. This limitation might lead to sub-optimal designs and significant difficulties with convergence.

In the work of Sigmund and Torquato [41], and later confirmed in a subsequent review by Stegmann and Lund [16], another limitation of the DMO1 material interpolation formulation

was identified. The effectiveness of DMO1 in obtaining desirable results is limited by its ability to push the design variables to their 0-1 bound limits. When implemented in the form shown in Equation 3.4, the weights are independently varying, causing material mixing where multiple materials can co-exist in the same element as all weights simultaneously contribute to $\mathbf{D_e}$.

To improve upon it, Sigmund and Torquato [41], formulated a simultaneous topology and multiple material optimization scheme, which extends SIMP to accommodate multiple materials. Referred to in this study as e-SIMP, the expression for interpolating three material phases, with one being void, can be written as shown in Equation 3.5. Here, $x_0^{top}$ is responsible for scaling the entire contribution of the elemental constitutive matrix $\mathbf{D_e}$, which moves between the two constitutive matrices $\mathbf{D_e^1}$ and $\mathbf{D_e^2}$ calculated for the two material phases.

$$\mathbf{D}_e = \left(x_0^{top}\right)^{\mathrm{P}} \left(\left[1 - \left(x_e^{mat1}\right)^{\mathrm{P}}\right] \mathbf{D}_e^1 + \left(x_e^{mat1}\right)^{\mathrm{P}} \mathbf{D}_e^2\right), \quad 0 \leqslant x_e^{matj} \leqslant 1 \qquad (3.5)$$

DMO1, unlike this e-SIMP formulation, does not link the weights to more than one constitutive matrix, which limits its capability to push all the design variables to discrete 0-1 values simultaneously. In e-SIMP, the term $(1-x_e^{matj})$ associates the material selection design variable $x_e^{matj}$ to multiple constitutive matrices. This linking ensures that an increase in one of the weights automatically reduces the weights of the other constitutive matrices, resulting in weights close to the design variable bounds of 0-1. Extending this formulation to four phases, three material phases, and one void phase, we get the formula in Equation 3.6, where $0 \leqslant x_e^{matj} \leqslant 1$.

$$\mathbf{D}_e = \left(x_0^{top}\right)^{\mathrm{P}} \left(\left[1 - \left(x_e^{mat1}\right)^{\mathrm{P}}\right] \mathbf{D}_e^1 + \left(x_e^{mat1}\right)^{\mathrm{P}} \left[\left[1 - \left(x_e^{mat2}\right)^{\mathrm{P}}\right] \mathbf{D}_e^2 + \left(x_e^{mat2}\right)^{\mathrm{P}} \mathbf{D}_e^3\right]\right)$$
$$= \left(x_0^{top}\right)^{\mathrm{P}} (\underbrace{\left[1 - \left(x_e^{mat1}\right)^{\mathrm{P}}\right] \mathbf{D}_e^1}_{w_1} + \underbrace{\left(x_e^{mat1}\right)^{\mathrm{P}} \left[1 - \left(x_e^{mat2}\right)^{\mathrm{P}}\right] \mathbf{D}_e^2}_{w_2} + \underbrace{\left(x_e^{mat1}\right)^{\mathrm{P}} \left(x_e^{mat2}\right)^{\mathrm{P}} \mathbf{D}_e^3}_{w_3}) \qquad (3.6)$$

In both cases, e-SIMP and DMO1, the number of design variables remain the same for $'m'$ materials. This does not allow the computational efficiency to be a good comparative measure. However, from the literature [16], we can also derive a limitation of e-SIMP. It is applicable only to a lower number of candidate materials. The reason for this is not exclusively highlighted in studies, but assuming it is true when more materials must be optimized, another DMO scheme, DMO2, can be used. This approach to multi-material interpolation is expressed in Equation 3.7, and the equation for a three-material interpolation can be seen in Equation 3.8. This approach, unlike DMO1, does not require explicit constraints on weights as suggested in [40]. In order to have "physically meaningful results", the summation of all weights adding up to one must be evaluated for DMO schemes. However, this is not necessary to be done during optimization and can be evaluated post-optimization [40].

$$\mathbf{D}_e = \sum_{j=1}^{m} \underbrace{\left[\left(x_e^{matj}\right)^{\mathrm{P}} \prod_{\substack{k \neq j \\ k=1}}^{m} \left[1 - \left(x_e^{matk}\right)^{\mathrm{P}}\right]\right]}_{w_j} \mathbf{D}_e^j \qquad (3.7)$$

$$\mathbf{D}_e = \underbrace{\left(x_e^{mat1}\right)^{\mathrm{P}} \left[1 - \left(x_e^{mat2}\right)^{\mathrm{P}}\right] \left[1 - \left(x_e^{mat3}\right)^{\mathrm{P}}\right] \mathbf{D}_e^1}_{w_1} + \underbrace{\left(x_e^{mat2}\right)^{\mathrm{P}} \left[1 - \left(x_e^{mat1}\right)^{\mathrm{P}}\right] \left[1 - \left(x_e^{mat3}\right)^{\mathrm{P}}\right] \mathbf{D}_e^2}_{w_2}$$
$$+ \underbrace{\left(x_e^{mat3}\right)^{\mathrm{P}} \left[1 - \left(x_e^{mat1}\right)^{\mathrm{P}}\right] \left[1 - \left(x_e^{mat2}\right)^{\mathrm{P}}\right] \mathbf{D}_e^3}_{w_3}$$

$$(3.8)$$

Similar to the term $(1 - x_e^{matj})$ in Equation 3.5, the term $\left(1 - x_e^{matk}\right)$ in Equation 3.7, implies that an increase in $x_e^{matj}$, corresponds to a decrease in the all other weights, helping push the design to a more 0-1 result. This scaling or decrease in all other weights, however, in this case, is different from what e-SIMP achieves, as seen from both Equations. For DMO2, the scaling can be better visualized in Figure 3.3a-b.
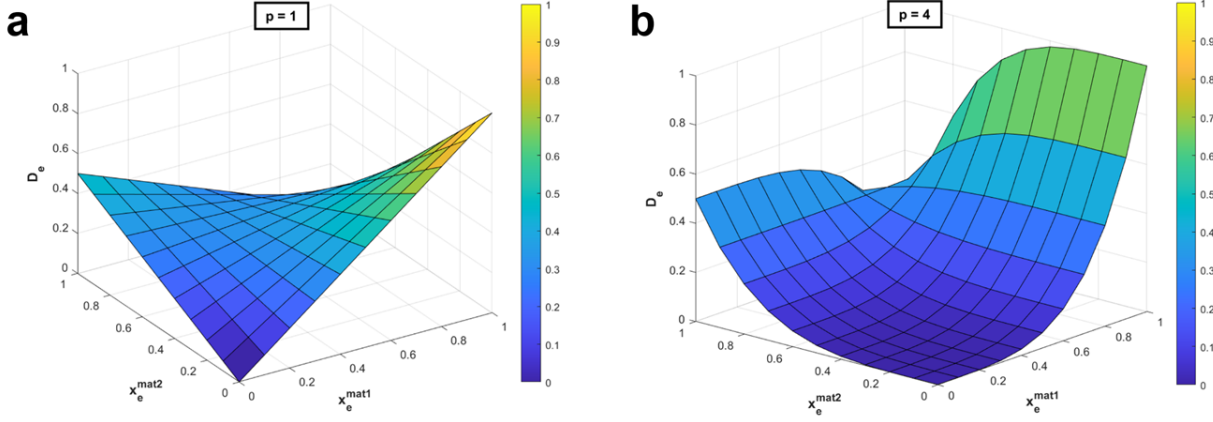


**Figure 3.3:** (a) DMO2 plot with penalty factor p = 1, shows that it penalises material mixing of $x_e^{mat1}$ and $x_e^{mat2}$ when both are fully dense, i.e., effective constitutive matrix value of the element $D_e$ value would become zero. However, it does not penalise material mixing for intermediate values. While (b) DMO2 plot with p = 4 shows that it penalises material mixing of $x_e^{mat1}$ and $x_e^{mat2}$ both when fully dense and with intermediate values.

In the plots shown in Figure 3.3a and b, two materials with arbitrary $D_e^1 = 1$ and $D_e^2 = 0.5$ are considered. $x_e^{mat1}$ and $x_e^{mat2}$ are the material selection design variables for DMO2. When the penalization factor is equal to one, as seen in 3.3a, it is observed that the interpolation function value for the arbitrary $D_e$ goes to zero when both materials are fully dense, significantly penalising material mixing. However, the same is not the case for intermediate densities when the penalty is one. Only when higher penalization is applied like p = 4, as seen in Figure 3.3b, the mixing of intermediate densities is also penalised, indicated by the flatness of the surface representing $D_e$ when both design variables have intermediate values lower than 0.5 [42]. This shows the effectiveness of this type of weight formulation for multi-material interpolation in reducing both intermediate densities and material mixing.

Such a definition of the weights in DMO2, despite being satisfactory in generating close-to 0-1 designs, does not guarantee a sum of weight functions to be less than equal to one. This violates the physical meaning of having more than 100% material in a single element. As a fix for this issue, DMO3 was proposed, where the weights are scaled by the sum of all weights during optimization. Doing so, however, limits the capability of the material interpolation approach to penalise values to 0-1 as much as DMO2, which can result in a topology with a significant amount of intermediate densities [40].

However, from the work of Sanders et al. [35], it was understood that DMO2, on implementation, does not produce a lot of elements with the sum of weights greater than one. These are limited to interfaces, and with some post-processing, this limitation can be mitigated fairly easily. As a result, DMO2 is still preferred over DMO3 in order to obtain more discrete designs at the cost of slight non-adherence to the condition stated in Equation 3.4b.

The results before and after post-processing results from DMO2 can be seen in Figure 3.4a and b, where the heuristic post-processing approach is seen to completely remove all material-mixing and a non-physical result where the total density of an element is greater than one.

In elements with such an issue which, as observed in Figure 3.4a are all along the interfaces, the design variable of the material with the largest contribution to the elemental density $\rho_e$ is assigned a density equal to $\min(\rho_e, 1)$, while all the other design variables for other materials are assigned a density of zero. The effect of such a post-processing step on the structures compliance and the volume fraction of each material would still need to be evaluated post-optimization [35].
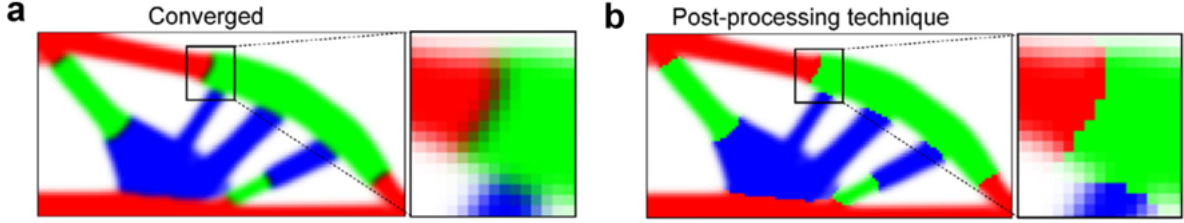


**Figure 3.4:** (a) Converged elements with total material density $\rho_e^T > 1$, can be (b) post-processed to have $\rho_e^T = min(\rho_e, 1)$, where $\rho_e$ corresponds to the material with the highest DMO weight $w_j$ [35].

A limitation of the DMO2 approach, which is not reported often, is the order in which the materials used are interpolated. This was understood from preliminary testing on the MMA-modified implementation of PolyMat by Sanders et al. [42]. It was observed that only when a decreasing order of material stiffnesses was used for multi-material interpolation did the optimization converge to well-defined topologies without premature convergence. This issue was also highlighted in a recent work by Li et al. [43]. It was shown in their work that sufficient penalization, as seen in Figure 3.3, cannot be achieved when using the reverse order of material properties. As a result, while the DMO2 scheme is the preferred choice for this work, design variables are defined such that stiffness for the material defined by $x_e^{mat1} >$ stiffness of the material defined by $x_e^{mat2}$ and so on.

## 3.2.4. Optimization Algorithm Choice

Once we have decided on the interpolation scheme and chosen the design variables for the optimization, the next step is to select an optimization algorithm that minimizes the compliance for these selected design variables. For a two-material system, we have four design variables per finite element. As a result, for a mesh with $N$ number of such elements, the number of design variables becomes $N \times 4$ or $N \times (m + 2)$ for $m$ materials. This implies that for large-scale optimization, the number of design variables would scale significantly, reiterating the exclusion of non-gradient-based approaches. As a result, we limit our options to choosing gradient-based algorithms only.

Two prominent optimization algorithms for structural topology problems often cited in the literature are the Method of Moving Asymptotes (MMA) and the Globally Convergent Method of Moving Asymptotes (GCMMA). These methods operate through sequential convex approximation techniques and can easily accommodate multiple linear inequality constraints [44]. Both the algorithms are also open-source and readily available to use on MATLAB. They have also been used in commercial topology optimization software, prompting the extension of this framework on commercial software.

In a benchmark study by Rojas and Stolpe [44], GCMMA was observed to obtain better designs and required fewer iterations than MMA, with better numerical performance. In their work, this improvement in numerical performance compared to MMA was attributed to the additional measures implemented in GCMMA to ensure theoretical global convergence. Contrary to this, GCMMA in another study by Alcazar [45] is described as slower than MMA. The

literature shows that optimization convergence rates do vary based on the method used and the proximity of the initial design point to the optimum. MMA has been observed to rapidly converge from distant initial points but may slow near the optimum. This is because it uses monotonous approximation functions. Conversely, non-monotonous approximation methods such as GCMMA yield stable solutions with good initial guesses but may be slow when starting from poor initial guesses [46]. However, the quality of the initial guess is often unknown for large design spaces with several constraints. As a result, GCMMA could potentially have slower convergence for our application. Nonetheless GCMMA is an effective alternative when MMA cannot achieve stable solutions. A more in-depth comparison of both algorithms can be referred to from the works of Rojas and Stolpe [44], and Zuo et al. [46].

MMA is the preferred optimization algorithm for this work because it has been widely implemented in the literature. Besides, it has been demonstrated to converge fast in some FAO studies [21], [37]. This is foreseen to be beneficial for troubleshooting issues.

## 3.2.5. Regularization Approach

The importance of regularization schemes like filtering in obtaining mesh-independent, checkerboard-free designs has been well-defined in the literature [47]. For the design variables in our work, which include both fibre orientations and density design variables, regularization of both types of design variables is paramount to obtain a mesh-independent topology design with smooth fibre orientations.

### Filters for density design variables

In order to avoid numerical instabilities during optimization, several filtering schemes for density design variables have been implemented and discussed in the literature, of which the most popular ones include sensitivity filters and density filters [12].

The sensitivity filter modifies element sensitivity values by a weighted average of the sensitivities of all elements within a user-defined radius $r_{min}$. The density filter, on the other hand, defines the physical density of an element as a weighted average of the design variables in a neighbourhood of radius $r_{min}$ as seen from Figure 3.5a [12].

Both the sensitivity and density filters are perfectly capable of maintaining the minimum feature size in the optimized topologies, enabling more manufacturable designs without thin geometric features. However, both generate substantial grey transition regions between solid and void regions. This issue can be solved for both cases by reducing the filter radius once sufficient convergence of density design variables is achieved. Additionally, projection-based schemes have been proposed to overcome the problem of grey-scale images associated with density filtering methods [12].

For projection methods like the Heaviside projection method (HSM), the projected density design variables are obtained through a smoothed Heaviside function. The smoothness of this function can be controlled by a continuation approach to achieve a stable convergence. This is done by gradually increasing the steepness of the function, which is controlled by the parameter $\beta$. The increase in the discreteness of the design variable before and after projection for different values of $\beta$ can be seen in Figure 3.5b. As $\beta$ increases, so does the discreteness of projected design variables. Such a projection method only ensures discrete solutions, where the grey scale results from the density filtering. As a result, when used in conjunction with density filtering, HSM can result in more discrete results [12].
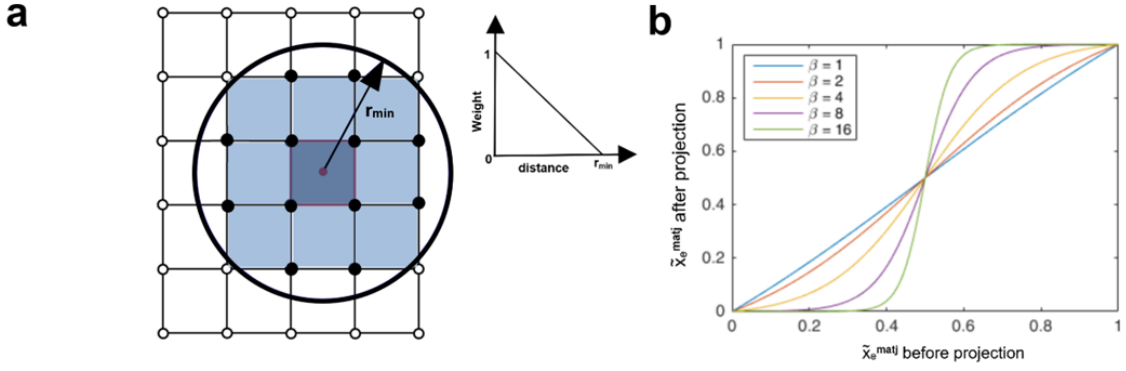
**Figure 3.5:** (a) A linear weighted average type density filter for densities with filter radius $r_{min}$ used for obtaining mesh-independent checkered board free designs. (b) For discrete designs, a linear to exponential projection of density variables using HSM can be achieved by increasing projection parameter $\beta$ [9], [48].

In recent literature on multi-material TO [32], [49], [50] to achieve discrete results, a density filter in addition to the HSM scheme is used as the preferred regularization scheme. Hence, the same is considered a tested regularization scheme for the current work. Such a combined density filter plus HSM filtering scheme can also reduce the number of iterations required for convergence to more discrete designs. This would be beneficial for this framework as well in terms of achieving better computational efficiency [47].

As suggested by Sigmund [47], the volume of the material must ideally be preserved before and after filtering. When using only a density filter or sensitivity filter, volume preservation is always achieved as long as the volume constraints are adjusted to use the filtered densities as well [12]. However, issues with significant volume changes can occur for HSM, given that it is a non-volume preserving regularization technique. As a result, the impact of HSM on optimized results from our framework will need to be assessed. This is done by determining how much the final volume deviates from the set volume constraints and if it is significant.

### Smoothing fibre orientation design variables

As seen earlier in Section 3.2.2, when using CFAO, fibre discontinuities can occur in certain regions of the design domain. To deal with these discontinuities, fibre smoothing is often carried out on the fibre orientation design variables using regularization schemes, similar to density filtering [37]. These fibre discontinuities are usually observed either in tension-compression regions where the principal stresses are equal in magnitude and the opposite direction or in regions with significantly low stress where the individual material orientation does not impact the stiffness of the overall structure [51].

For the first type of discontinuities, in-optimization filtering can be a viable choice, which is also implemented by Schmidt et al. [37] in their work on CFAO for 2D and 3D structures. In their work, all the individual fibre angles are filtered or smoothed with respect to the orientation of their neighbours within a filter radius. This filtering is done at each optimization step from the start of the optimization. However, as noted, tuning the overall optimization, including densities and fibre angles, to accommodate the in-optimization filtering step can be difficult as the instabilities and oscillations obtained due to such a step are quite high if not treated well [37].

For the second type of discontinuity, however, a heuristic approach of matching the fibre orientation to its neighbours at the element level can be carried out like done in the work of

[51], where only the fibre orientation which does not match the immediate neighbours is modified and not the neighbouring elements. This is done only after the densities have converged to a large extent so that overall convergence is not affected much due to this in-optimization heuristic update of the discontinuous fibre angles. Additionally, we can filter the fibre angles post-optimization through convolution and using a set of update criteria as done in the work of Qiu et al. [21].

In the work of Stragiotti [10] on filtered-CFAO, a Gaussian filter with a kernel of 11x11, as shown in Figure 3.6a, was used for obtaining smooth fibre orientations by filtering all elemental fibre orientations throughout the optimization. The kernel, as shown in Figure 3.6b, moves along the 2D data, multiplies the value of elements under it with the respective value of Gaussian weight over those elements, and sums the results as the single value, which then becomes the filtered fibre orientation of that element. The disadvantages of this approach in their study was a slightly slow convergence and higher objectives.
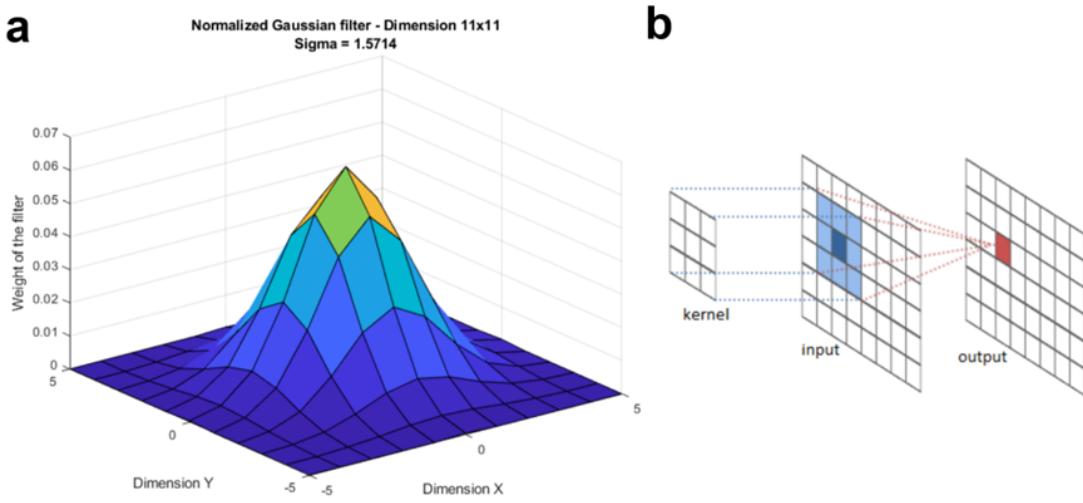


**Figure 3.6:** (a) Gaussian filter kernel with size of 11x11 and $\sigma = y_{dim}/7$, (b) sliding across a mesh, determining each element's value based on neighbouring element's value scaled by the filter value in the distribution plot from (a), for that element [10].

The same Gaussian filter was also used in the preceding work for this thesis Almeida [6], which filtered fibre orientations to give smooth fibre paths. As a result, in our work, we also choose the Gaussian filter as a simple yet effective in-optimization fibre angle filtering strategy.

$$4$$

# Computational Model

## 4.1. Concurrent Multi-Material and Fiber-Angle Topology Optimization Framework

### 4.1.1. Formulating the MM-FATO Problem

Considering all the design requirements and choices, an MM-FATO problem for a two-material system is derived, and the same can be expressed as Equation 4.1.

$$\text{Find } \mathbf{X} = \left\{ \mathbf{x^{mat1}}, \mathbf{x^{mat2}}, \cos(\boldsymbol{\theta}), \sin(\boldsymbol{\theta}) \right\}$$

$$\text{minimize } C(\mathbf{X}) = \mathbf{U}^T \mathbf{K}(\mathbf{X}) \mathbf{U} = \sum_e^N \mathbf{U_e^T} \mathbf{K_e}(\mathbf{x_e}) \mathbf{U_e}$$

$$\text{Subject to: } \begin{cases} \mathbf{K}(\mathbf{X})\mathbf{U} = \mathbf{F} \\ 0 < x_i^{mat1}, x_i^{mat2} \leq 1, \quad i = 1, 2, ..., N \\ -1 \leq cos(\theta)_i \leq 1, \quad i = 1, 2, ..., N \\ -1 \leq sin(\theta)_i \leq 1, \quad i = 1, 2, ..., N \\ g_j = \left( \dfrac{\sum_{i=1}^N v_i \times x_i^{matj}}{\sum_{i=1}^N v_i} \right) \leq \Omega_j, \quad j = 1, 2 \end{cases} \quad (4.1)$$

Where $\mathbf{x^{mat1}}$ and $\mathbf{x^{mat2}}$ are the two material density design variable vectors for materials one and two. These, along with the two fibre orientation design variables $\cos(\boldsymbol{\theta})$ and $\sin(\boldsymbol{\theta})$, make up the continuous design variable array that will be updated by MMA to minimize compliance $C(\mathbf{X})$. The displacement vector $\mathbf{U}$ is calculated using the force-displacement relation $\mathbf{K}(\mathbf{X})\mathbf{U} = \mathbf{F}$, where $\mathbf{F}$ is the design-independent load vector, and $\mathbf{K}(\mathbf{X})$ is the global stiffness matrix. Since an elemental topology optimization is carried out where DMO is extended with CFAO, a finite element mesh discretizes the design domain $\Omega$ into $N$ elements. This essentially reduces the compliance calculation to the summation of the resultant elemental compliance values represented by elemental stiffness matrix $\mathbf{K_e}$, a function of the design variable vector for each element $\mathbf{x_e}$ and elemental displacement vector $\mathbf{U_e}$.

This framework implements two types of constraints. The first constraint is the linear inequality volume constraint $g_j$, defined for each material, where $j = 1, 2$. During the optimization, this constraint maintains the total volume fraction occupied by each material density design variable equal to or below a user-prescribed fraction $\Omega_j$. This total volume is obtained by summing all the elemental density design variable values $x_i^{matj}$ and multiplying it by the volume of the $i - th$ element $v_i$. The occupied fraction is then calculated by dividing the obtained value by the design domain's total volume. Although not highlighted, the constraint definition

has a *tilde* sign over the design variable. This means that the filtered density design variables are used to calculate the total volume occupied by a given design variable and the constraint itself, which ensures volume preservation as suggested by Sigmund [47]. Similarly, compliance is evaluated using the filtered material density design variables as well.

The second type is the standard bound or box constraints. The material density design variables can take any values between 0 and 1, indicating the absence or presence of material in an element. The lower value of $x_i^{mat1}$ and $x_i^{mat2}$ is considered non-zero with a value of $1 \times 10^{-3}$ in this work to avoid singularities. For fibre orientation design variables, bound constraints are chosen as simple box constraints. This is simplified from the equality constraint underlined in Nomura et al. [38]. Such an implementation is done only to maintain ease of defining the bounds for the optimization algorithm in a similar format to the material selection design variables. This simplification for polar to Cartesian, and from Cartesian and a simplified Cartesian definition can be seen in Figure 4.1.
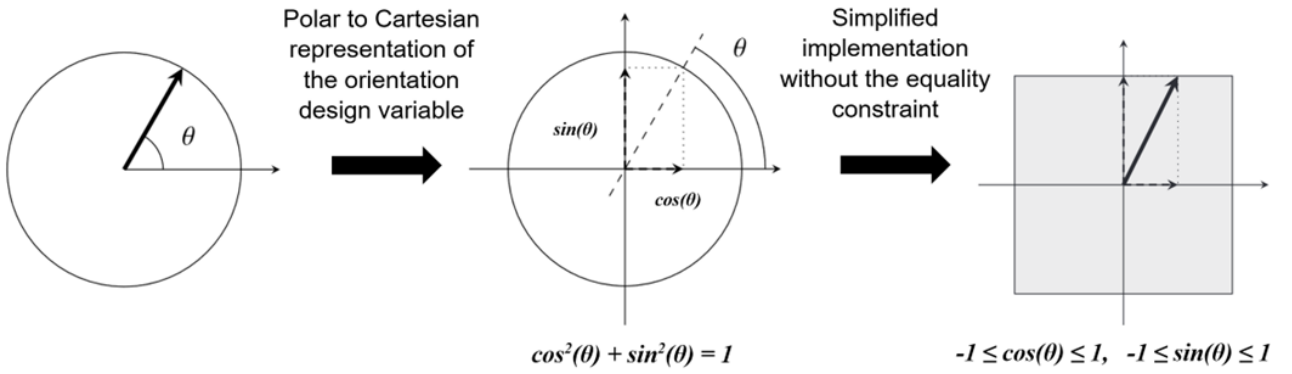


**Figure 4.1:** Modifying the fibre angle orientation design variable from Polar, $\theta$ to Cartesian representation with an equality constraint bounding the components. For ease of implementation, it is simplified as Cartesian components of $\theta$ equal to $cos(\theta)$ and $sin(\theta)$, bounded by box constraints $-1 \leq cos(\theta) \leq 1$ and $-1 \leq sin(\theta) \leq 1$ [38].

## 4.1.2. Initial Guess - Design Variables

The design variables, $x_i^{mat1}$ and $x_i^{mat2}$ used for the DMO2 approach for this framework, are to be initiated with the same values. Starting with a balanced guess is the fairest approach, as it avoids preconceived bias towards specific materials. It is important to avoid this, as even a small change in design variables could cause a strong preference for a particular material during optimization [16].

The fibre orientations, on the other hand, can be defined either uniformly or randomly. Both approaches have their own advantages and disadvantages. The number of iterations and evaluations required to obtain the best solution with the uniform guess is quite high in continuous fibre angle optimization studies [6]. Still, it has the best potential to give the most optimal solution using a gradient-based approach, at least for less complex problems regarding loads and design domain shape. On the other hand, a random orientation field as an initial guess could avoid the high computational costs at the cost of a slightly worse local minimum [37]. The work by Schmidt et al. [37] reported some results for random orientations as an initial guess that gave more consistent compliance results despite slight changes in topology for multiple trials. The results obtained for random initial guesses were close to the best uniform initial guess evaluated in their work. Nonetheless, a more extensive assessment of both initial guesses in the context of MM-FATO must be considered. Hence, a detailed evaluation is done later in Section 6.1.1.

### 4.1.3. Filtering Design Variables

**Filtering density design variables**

A simple Heaviside projection scheme with continuation, as given in Equation 4.2, was applied to an MMA-modified version of PolyMat [42] to regularize the topology and obtain more discrete designs. However, the same could not achieve stable results, even with low values for $\beta$ as a limit when continuation is applied or when applied throughout with fixed $\beta$.

$$\bar{x}_e^{matj} = 1 - e^{-\beta\tilde{x}_e^{matj}} + \tilde{x}_e^{matj}e^{-\beta} \tag{4.2}$$

As a result, for the final MM-FATO framework, only a density-based filter is implemented, which averages the material densities of the $i-th$ element $x_i^{matj}$ using a linear convolution filter with filter radius $r_{min}$ [42]. The density filter can be mathematically expressed by Equation 4.3 [47],

$$\tilde{x}_e^{matj} = \frac{\sum_{i \in N_e} w\left(\mathbf{x}_i\right) x_i^{matj}}{\sum_{i \in N_e} w\left(\mathbf{x}_i\right)}; \qquad w\left(\mathbf{x}_i\right) = 1 - \left\|\mathbf{x}_i - \mathbf{x}_e\right\| / r_{min} \tag{4.3}$$

Where $N_e$ defines the number of elements in the neighbourhood of element $e$ defined by filter radius $r_{min}$. $\mathbf{x_i}$ is the centroid of the $i-th$ element in the neighbourhood of element $e$, and $x_e$ is the centroid of element $e$. $w(\mathbf{x_i})$ is a "linearly decaying weighting function" of $i-th$ element.

Since implementing HSM during optimization did not provide stable convergence for our framework, alternative approaches can be evaluated to save some computational effort. As we know, despite being widely used in topology optimization problems and producing mesh-independent and checkered-board-free designs, density filters take significantly more iterations to converge. Furthermore, this can also be seen in Figure 4.2a.
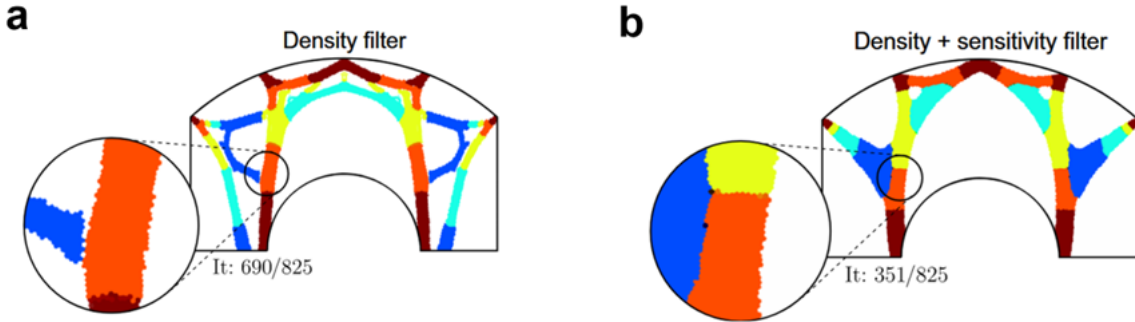


**Figure 4.2:** (a) The topology obtained when using only a density filter that takes 690 iterations and has gaps at material interfaces once the filter is turned off. (b) Topology obtained when using density plus sensitivity filter takes only 351 iterations and has better interfaces on turning the filter off [42].

Hence, to reduce the higher computation time associated with using only density filters, a combination of sensitivity and density filters was implemented in Sanders et al. [42]. The number of iterations was halved when such a combination was used, as seen from Figure 4.2a and b. This filtered sensitivity for the combined scheme is expressed in Equation 4.4. Using both together results in a quicker convergence with significantly better multi-material interface renderings, as also observed from Figure 4.2b.

$$\frac{\widetilde{\partial C}}{\partial x_e^{matj}} = \frac{\sum_{i \in N_e} w\left(\mathbf{x}_i\right) \tilde{x}_i^{matj} \frac{\partial C}{\partial x_i^{matj}}}{\tilde{x}_i^{matj} \sum_{i \in N_e} w\left(\mathbf{x}_i\right)} \tag{4.4}$$

However, given that MMA is being used for our framework, unlike the Zhang-Paulino-Ramos update scheme used in the work of Sanders et al. [35], it is worth implementing both variations for our work and seeing the impact of using these two filter combinations for the MM-FATO framework. This is evaluated further in Section 6.2.1.

## Filtering fibre orientation variables

From a preliminary assessment, using the Gaussian filter to filter fibre orientation during the optimization process resulted in significantly high oscillations. These oscillations could not be substantially subsided through general MMA parameter tuning or a separate MMA move limit update for material density design variables and fibre orientation design variables as suggested by Schmidt et al. [37] to stabilize in-optimization filtering with MMA. A visual comparison of results when filtering for fibre orientation is done during gradient update for a single material FATO approach using *fmincon* as done by Almeida [6], and the framework developed in this work can be referred from Figure 4.3.
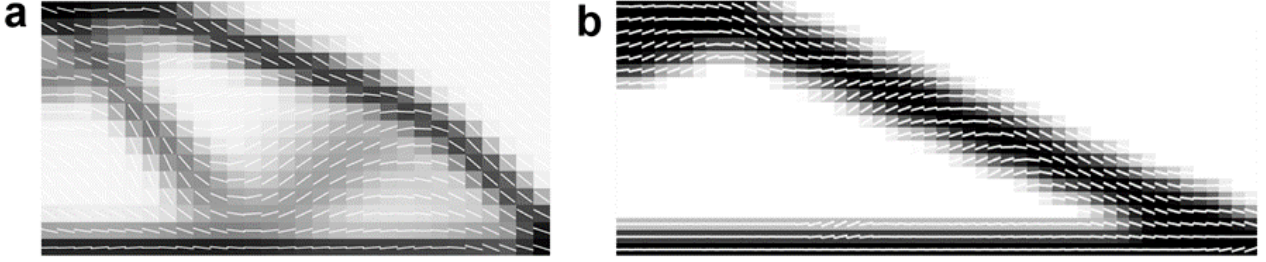


**Figure 4.3:** (a) Smooth fibre orientations along the loading paths obtained at convergence with *fmincon* implementation of CFAO, when in-optimization Gaussian filtering is used, whereas (b) with the MMA implementation of the same in-optimization filtering, oscillations cause fibre orientations to be aligned away from load path in some regions.

As a result, although it is important to filter design variables during the continuation process to keep non-convexity in check and ensure that the local fibre orientations are not stuck in local minima, [52], in this work, fibre orientation filtering is only carried out in the post-processing stages to avoid an unstable optimization.

In their work, Qiu et al., [21] also implemented orientation filters only in the post-optimization stages. However, they filter the fibre orientations for 10 iterations once the density design variables have largely converged. After that, the fibre angles are allowed to be updated by the optimization algorithm and filtered simultaneously, but without the sensitivities corresponding to the orientation design variables being filtered. Nonetheless, preliminary tests determined that a single post-processing step for fibre angles could also provide acceptable fibre continuity.

The Gaussian filter, as utilized by Stragiotti [10], during another set of preliminary analyses, only worked for regular design domains and faced difficulties in implementation when modified to accommodate for filtering angles across non-designable domain or passive regions in the domain. The results for this issue can be referred to in Appendix A. Given this limitation, an alternate convolution filter similar to the one used for the density filter is proposed for the MM-FATO framework. The angles are further scaled by the corresponding element's total material density $(\sum_{j=1}^{m} x_i^{matj})$ to reduce the impact of orientations of the void elements. The mathematical representation for this filter can be referred to from Equation 4.5.

$$\tilde{\theta}_e = \frac{\sum_{i \in N_e} w_\theta\left(\mathbf{x}_i\right) \sum_{j=1}^{m} x_i^{matj} \theta_i}{\sum_{i \in N_e} w_\theta\left(\mathbf{x}_i\right) \sum_{j=1}^{m} x_i^{matj}}$$
$$w_\theta\left(\mathbf{x}_i\right) = 1 - \left\|\mathbf{x}_i - \mathbf{x}_e\right\| / r_{cur}$$

(4.5)

## 4.1.4. Finite Element Analysis

### Material Model

The fibre-reinforced polymer material in this work is modelled as a linear elastic transverse isotropic material. This is because the direction along the reinforced fibres, which is along the x-axis, is much higher than the stiffness along the other directions. In this case, the material's stiffness in all transverse directions to the fibre orientation is assumed to be the same. This linear transverse isotropic elastic material is modelled using the constitutive matrix $\mathbf{D}$ in Equation 4.6.

$$\mathbf{D} = \begin{bmatrix} \frac{1}{E_x} & \frac{-\nu_{yx}}{E_y} & \frac{-\nu_{yx}}{E_y} & 0 & 0 & 0 \\ \frac{-\nu_{xy}}{E_x} & \frac{1}{E_y} & \frac{-\nu_{zy}}{E_y} & 0 & 0 & 0 \\ \frac{-\nu_{xy}}{E_x} & \frac{-\nu_{yz}}{E_y} & \frac{1}{E_y} & 0 & 0 & 0 \\ 0 & 0 & 0 & \frac{2(1+\nu_{yz})}{E_y} & 0 & 0 \\ 0 & 0 & 0 & 0 & \frac{1}{G_{xy}} & 0 \\ 0 & 0 & 0 & 0 & 0 & \frac{1}{G_{xy}} \end{bmatrix}^{-1} \tag{4.6}$$

Based on the requirement of modelling for thin 2D structures and simplifying the modelling for the transversely isotropic model, a plane stress condition is assumed. As a result, the thickness direction will have dimensions significantly smaller than the other two dimensions and only in-plane elements of the elasticity tensor will be evaluated. The reduced form of the constitutive matrix based on this assumption is represented by the matrix in Equation 4.7. $E_x$, $E_y$ are tensile modulus corresponding to the two principal directions, $\nu_{xy}$ and $\nu_{yx}$ being the major and minor Poisson's ratios in $xy$-plane, and $G_{xy}$ as the in-plane shear modulus.

$$\mathbf{D_0} = \begin{bmatrix} \frac{E_x}{1-\nu_{xy}\nu_{yx}} & \frac{\nu_{xy}E_y}{1-\nu_{xy}\nu_{yx}} & 0 \\ \frac{\nu_{xy}E_y}{1-\nu_{xy}\nu_{yx}} & \frac{E_y}{1-\nu_{xy}\nu_{yx}} & 0 \\ 0 & 0 & G_{xy} \end{bmatrix} \tag{4.7}$$

The relation $\nu_{xy}E_y = \nu_{yx}E_x$ is considered to ensure symmetry of the constitutive matrix. Furthermore, the shear modulus $G_{xy}$ in Equation 4.7 follows the standard transverse isotropic definition resulting in $G_{xy} = \frac{E_x}{2(1+\nu_{xy})}$.

The elasticity matrix in Equation 4.7 is orientated along the x-axis, representing the direction of the fibre. When spatially orienting the materials in the design domain along an arbitrary fibre orientation $\theta$, this elasticity matrix can be transformed using the transformation matrices $\mathbf{T_1}$ and $\mathbf{T_2}$ as shown in Equations 4.8, 4.9 and 4.10. $\theta$ in this transformation is assumed to be the angle obtained by rotating the material anti-clockwise from the positive x-axis.

$$\mathbf{T_1}(\theta) = \begin{bmatrix} cos^2\theta & sin^2\theta & 2cos\theta sin\theta \\ sin^2\theta & cos^2\theta & -2cos\theta sin\theta \\ -cos\theta sin\theta & cos\theta sin\theta & cos^2\theta - sin^2\theta \end{bmatrix} \tag{4.8}$$

$$\mathbf{T_2}(\theta) = \begin{bmatrix} cos^2\theta & sin^2\theta & cos\theta sin\theta \\ sin^2\theta & cos^2\theta & -cos\theta sin\theta \\ -2cos\theta sin\theta & 2cos\theta sin\theta & cos^2\theta - sin^2\theta \end{bmatrix} \tag{4.9}$$

$$\mathbf{D}(\theta) = \mathbf{T_1}^{-1}(\theta) \cdot \mathbf{D_0} \cdot \mathbf{T_2}(\theta) = \begin{bmatrix} D_{11} & D_{12} & D_{13} \\ D_{12} & D_{22} & D_{23} \\ D_{13} & D_{23} & D_{33} \end{bmatrix} \tag{4.10}$$

To compute the compliance, we must calculate the global stiffness matrix $\mathbf{K}$ and the displacement vector $\mathbf{U}$ of the design domain for any given loads and boundary conditions. In this work, only single-load cases are examined. However, extension to multiple loads can be done by treating each load case separately to calculate the stiffness matrices and a weighted sum of the compliance can be obtained as done by Andreassan et al. [53] for an isotropic material topology optimization.

Given that we discretize the design domain into finite elements for optimization, we must assemble the global stiffness matrix and the displacement vector from the stiffness matrix and displacement of individual elements in the finite element mesh. Thus, the details for the finite element mesh used must be defined first before detailing the stiffness matrix assembly and compliance calculation.

### Finite Element Mesh

The current study explores a simple rectangular design domain for the multi-material-fibre-angle topology optimization framework. The most effective way to mesh such a design domain is to use simple and computationally efficient quadrilateral elements, which in our case is the 4-node quadrilateral element. These elements generate a uniform mesh for the given design space, where the loads and boundary conditions will be applied. Doing it this way also allows for a fair and simplistic comparison of our model's resultant designs and objectives against other reported studies in the literature. An overview of the quadrilateral mesh element used to generate a uniform mesh for a simple half-MBB-beam load case can be seen in Figure 4.4a. For an example mesh size of 4 x 3, Figure 4.4b shows the column-wise node numbering used [53].
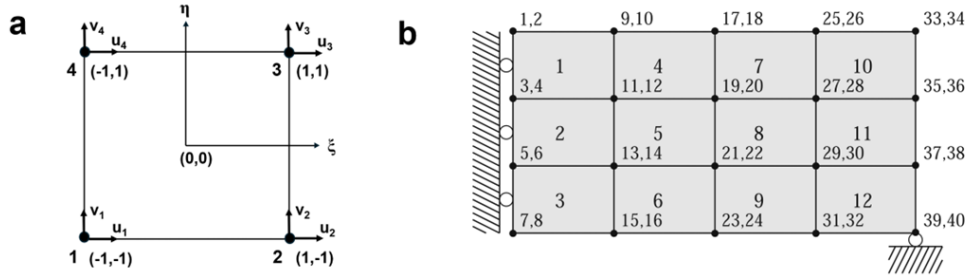


**Figure 4.4:** For an example of a simple half-MBB-beam load case, the domain is uniformly discretized with (a) 4-node quadrilateral finite elements that have 2 degrees of freedom (dof) at each node. (b) Node numbering for each dof from the top left node to the bottom right is the same as used in [53].

As seen in Figure 4.4a, the 4-node quadrilateral mesh element has four nodes with two dofs each for displacements $u$ and $v$ in the $\xi$ and $\eta$ directions. As a result, a total of eight dofs per element are obtained. For such an element, we define four bi-linear shape functions corresponding to each node as shown in Equation 4.11 [54]. The B-matrix or the strain-displacement matrix, as seen in Equation 4.12 [54], is characterized by the gradients of the shape functions that relate the in-plane strains to the eight displacements corresponding to each dof of the quad-element as seen in Figure 4.4a.

$$N_1 = \tfrac{1}{4}(1-\xi)(1-\eta) \quad N_2 = \tfrac{1}{4}(1+\xi)(1-\eta) \quad N_3 = \tfrac{1}{4}(1+\xi)(1+\eta) \quad N_4 = \tfrac{1}{4}(1-\xi)(1+\eta) \tag{4.11}$$

$$\mathbf{B} = \begin{bmatrix} \frac{\partial N_1(\xi,\eta)}{\partial \xi} & 0 & \frac{\partial N_2(\xi,\eta)}{\partial \xi} & 0 & \frac{\partial N_3(\xi,\eta)}{\partial \xi} & 0 & \frac{\partial N_4(\xi,\eta)}{\partial \xi} & 0 \\ 0 & \frac{\partial N_1(\xi,\eta)}{\partial \eta} & 0 & \frac{\partial N_2(\xi,\eta)}{\partial \eta} & 0 & \frac{\partial N_3(\xi,\eta)}{\partial \eta} & 0 & \frac{\partial N_4(\xi,\eta)}{\partial \eta} \\ \frac{\partial N_1(\xi,\eta)}{\partial \eta} & \frac{\partial N_1(\xi,\eta)}{\partial \xi} & \frac{\partial N_2(\xi,\eta)}{\partial \eta} & \frac{\partial N_2(\xi,\eta)}{\partial \xi} & \frac{\partial N_3(\xi,\eta)}{\partial \eta} & \frac{\partial N_3(\xi,\eta)}{\partial \xi} & \frac{\partial N_4(\xi,\eta)}{\partial \eta} & \frac{\partial N_4(\xi,\eta)}{\partial \xi} \end{bmatrix} \tag{4.12}$$

## Calculating compliance

Once we have the strain displacement matrix defined in Equation 4.12, we can calculate the stiffness matrix using the relation in 4.13 that relates the strain-displacement matrix and the material constitutive matrix to the stiffness matrix.

$$\mathbf{K_e} = \int_{\Omega_e} \mathbf{B^T D_e}(\theta)\mathbf{B} \ \mathrm{d}\Omega_e; \qquad \mathbf{K} = \sum_{i=1}^{N} \mathbf{K_e} \tag{4.13}$$

A simple integration of all the elemental stiffnesses calculated using the formulation in Equation 4.13 gives us the global stiffness matrix. The displacement is calculated using the $\mathbf{F} = \mathbf{KU}$ relation for force and displacement. Using $\mathbf{U}$ and $\mathbf{K}$ obtained, the compliance $\mathrm{C} = \mathbf{U^T KU}$ is easily calculated. In MATLAB, this implementation for the assembly of the stiffness matrix and calculation of compliance is the same as done in the 88-line code of Andreassen et al. [53] using sparse and Cholesky factorization for improving computational efficiency.

Since DMO2 material interpolation scheme [16] is the choice of a material interpolation scheme for MM-FATO framework, the elemental constitutive matrix defining $\mathbf{K_e}$ can be defined as in Equation 4.14. For $j - th$ material, the corresponding elemental constitutive matrix $\mathbf{D_e^j}$ is a function of $\theta$ obtained by taking the tan inverse of the two orientation design variable values for that element.

$$\mathbf{D_e}(\theta) = \sum_{j=1}^{m} \left(x_e^{matj}\right)^p \prod_{\substack{k \neq j \\ k=1}}^{m} \left(1 - \left(x_e^{matk}\right)^p\right) \mathbf{D_e^j}(\theta); \qquad i = 1, \cdots, N \tag{4.14}$$

However, for the multi-material interpolation scheme, the constitutive matrix is different for different material properties being considered and at the same time, for fibre angle optimization, fibre orientations are also spatially varying across elements in the design domain. This results in assembling the stiffness matrix for medium-scale or large-scale problems with a higher number of mesh elements, a computationally expensive task. Furthermore, this cost increases with increasing candidate materials and mesh elements. This is still a limitation of using the DMO2 interpolation scheme when considering the computational cost. Nonetheless, such a formulation offers a simple and robust implementation.

## 4.1.5. Sensitivity Analysis

Since, for this framework, a gradient-based optimization algorithm is used to minimize the objective function, gradients, or sensitivities of the objectives and constraints with respect to the design variables is essential. The effectiveness of the gradient-based optimization algorithm, which in our case is MMA, is highly dependent on providing accurate gradients [7]. As a result, all the gradients used in this work are calculated using adjoint sensitivity analysis. Equations 4.15-4.24 show all the gradients for the objective function and constraints with respect to the four design variables.

$$\frac{\partial \mathrm{C}}{\partial \mathbf{X}} = -\mathbf{U^T} \frac{\partial \mathbf{K}}{\partial \mathbf{X}} \mathbf{U} = -\left(\mathbf{U_e^T}\right) \frac{\partial \mathbf{K}_e}{\partial \mathbf{X}} \mathbf{U_e} \tag{4.15}$$

$$\frac{\partial \mathbf{K_e}}{\partial \mathbf{X}} = \int_{\Omega_e} \mathbf{B^T} \frac{\partial \mathbf{D_e}}{\partial \mathbf{X}} \mathbf{B} \ \mathrm{d}\Omega_e \tag{4.16}$$

The sensitivities of the objective function with respect to the density design variables $x_e^{matj}$, where $j = 1, 2$ can then be expressed as shown in Equations 4.17-4.20,

$$\frac{\partial \mathbf{D_e}}{\partial x_e^{matj}} = \frac{\partial \mathbf{D_e}}{\partial \tilde{x}_e^{matj}} \frac{\partial \tilde{x}_e^{matj}}{\partial x_e^{matj}} \tag{4.17}$$

Where,

$$\frac{\partial \mathbf{D_e}}{\partial \tilde{x}_e^{mat1}} = p \left( \tilde{x}_e^{mat1} \right)^{p-1} \left( 1 - \left( \tilde{x}_e^{mat2} \right)^p \right) \mathbf{D_e^1} - p \left( \tilde{x}_e^{mat1} \right)^{p-1} \left( \tilde{x}_e^{mat2} \right)^p \mathbf{D_e^2}, \tag{4.18}$$

$$\frac{\partial \mathbf{D_e}}{\partial \tilde{x}_e^{mat2}} = -p \left( \tilde{x}_e^{mat2} \right)^{p-1} \left( \tilde{x}_e^{mat1} \right)^p \mathbf{D_e^1} + p \left( \tilde{x}_e^{mat2} \right)^{p-1} \left( 1 - \left( \tilde{x}_e^{mat1} \right)^p \right) \mathbf{D_e^2}, \tag{4.19}$$

and,

$$\frac{\partial \tilde{x}_e^{matj}}{\partial x_e^{matj}} = \frac{w\left(\mathbf{x}_i\right)}{\sum_{i=1}^N w\left(\mathbf{x}_i\right)}; \qquad w\left(\mathbf{x}_i\right) = 1 - \left\| \mathbf{x}_i - \mathbf{x}_e \right\| / r_{min} \tag{4.20}$$

The sensitivities of the objective function with respect to the orientation design variables $\theta_e$, can be further expressed as shown in Equations 4.21-4.23,

$$\frac{\partial \mathrm{C}}{\partial \cos(\theta)} = \frac{\partial \mathrm{C}}{\partial \theta_e} \times \frac{\partial \theta_e}{\partial \cos(\theta)}; \qquad \frac{\partial \mathrm{C}}{\partial \sin(\theta)} = \frac{\partial \mathrm{C}}{\partial \theta_e} \times \frac{\partial \theta_e}{\partial \sin(\theta)}, \tag{4.21}$$

Where,

$$\frac{\partial \mathrm{C}}{\partial \theta_e} = -\mathbf{U_e^T} \left\{ \int_{\Omega_e} \mathbf{B^T} \left( \frac{\partial \mathbf{T_1}\left(\theta_e\right)^{-1}}{\partial \theta_e} \mathbf{D_0} \mathbf{T_2}\left(\theta_e\right) + \mathbf{T_1}\left(\theta_e\right)^{-1} \mathbf{D_0} \frac{\partial \mathbf{T_2}\left(\theta_e\right)}{\partial \theta_e} \right) \mathbf{B} \, \mathrm{d}\Omega_e \right\} \mathbf{U_e}, \tag{4.22}$$

and,

$$\frac{\partial \theta_e}{\partial \cos(\theta)} = -\frac{\sin(\theta)}{(\cos^2((\theta)) + \sin^2((\theta)))}; \qquad \frac{\partial \theta_e}{\partial \sin(\theta)} = \frac{\cos(\theta)}{(\cos^2(\theta) + \sin^2(\theta))} \tag{4.23}$$

Lastly, the sensitivities of volume constraints used with respect to the density design variables can be seen in Equation 4.24.

$$\frac{\partial g_j}{\partial x_e^{matj}} = \frac{\partial g_j}{\partial \tilde{x}_e^{matj}} \frac{\partial \tilde{x}_e^{matj}}{\partial x_e^{matj}}; \qquad \frac{\partial g_j}{\partial \tilde{x}_e^{matj}} = \frac{1}{\sum_{i=1}^N v_i * \Omega_j} \tag{4.24}$$

The $(\tilde{x})$ over the density design variables indicates filtered values. Since filtered density design variables are used to calculate the compliance and volume constraints, the sensitivities must be calculated with respect to filtered sensitivities as well.

For gradient-based approaches, calculating sensitivities, along with the assembly of the global stiffness matrix, is one of the most computationally expensive tasks during the optimization. For the implementation of MM-FATO in this work, computing sensitivities for each material design variable includes calculating the elemental stiffness matrix $'m'$ number of times for $'m'$ material design variables, further increasing the base computational time required.

However, the stiffness matrix calculated for deriving compliance earlier cannot be reused directly for sensitivity calculations. Given the way the $\mathbf{D_e}$ matrix is calculated for stiffness matrix, the individual constitutive matrix elements $\mathbf{D_e^1}$ and $\mathbf{D_e^2}$ are unavailable to carry out the calculation required in Equations 4.18 and 4.19. To that end, a template approach to stiffness matrix calculation similar to the one used by Chandrasekhar et al. [33] is implemented to facilitate this exercise. Doing so assumes that the computational costs are kept at the minimum computation required to calculate and assemble the sensitivities for the given objective and design space.

For brevity, the calculation and assembly of these sensitivities are not explained in detail here. However, an explanation of how this approach is used for MM-FATO implementation in MATLAB can be referred to from Appendix B.

## 4.1.6. Optimization algorithm

The method of moving asymptotes or MMA, is the optimization algorithm of choice for the new MM-FATO framework. The MATLAB codes mmasub.m and subsolve.m written by Svanberg [55] are used to update the material selection and fibre angles design variables iteratively in order to minimize compliance.

Several inputs besides the design variables must be provided to the mmasub.m routine for solving the problem. The most obvious ones required to solve a simple optimization formulation include the optimization objectives, design variable vector, both the bound and volume constraints for the design variables and the analytically derived gradients for objective and constraint with respect to all the design variables. For this work, only first-order gradients or sensitivities are passed to the MMA algorithm. While second-order derivatives or the Hessian can be provided to the optimization algorithm for more accurate results, the computation costs of calculating outweigh the benefits. They are hence not derived [45].

However, the formulation that MMA solves differs from the standard optimization formulation. Hence, additional input from the user is required. The formulation of the optimization problem that MMA solves can be written as shown in Equation 4.25.

$$
\begin{aligned}
\textbf{minimize} \quad & f_0(X) + a_0 z + \sum_{i=1}^{m}\left(c_i y_i + \tfrac{1}{2}d_i y_i^2\right) \\
\textbf{Subject to:} \quad & f_i(X) - a_i z - y_i \leq 0, & i = 1, \ldots, m \\
& \alpha_j \leq x_j \leq \beta_j, & j = 1, \ldots, N \\
& y_i \geq 0, & i = 1, \ldots, m \\
& z \geq 0,
\end{aligned}
\tag{4.25}
$$

Where, $f_0(X)$ and $f_i(X)$, are all differentiable and continuous functions with respect to design variables $x_i$ in $X$. Furthermore, $y_i,...,y_m$ and $z$ are the artificial variables used to solve min-max or least square problem types. Since in this work, we do not need such a formulation, we set the indices corresponding to these artificial variables to standard values as described in [56].

To solve only for $f_0(X)$, we require $y_i$ variables to become zero. This is done by setting $c_i$ to a large number, say 1000, as suggested by the author [56]. Doing so makes the $y_i$ variables "expensive" and, as a result, are assigned negligible values by the optimization algorithm. The rest of the indices are assigned as follows: $a_0 = 1$, $a_i = 0$, and $d_i = 0$ for each $i$ based on the default values in [56]. Once the artificial variables are dealt with, we have the natural design variables, $x_1,...,x_N$, which are required to solve the standard non-linear programming equation $f_0(X)$. These design variables are bound between $\alpha_j^{(k)}$ and $\beta_j^{(k)}$.

MMA, being a convex approximation algorithm, uses the supplied gradient information to determine the convex approximation functions $\tilde{f}_j^{(k)}$, which replace the $f_0(X)$ functions. The curvature of these convex sub-problems is primarily influenced by two parameters, the lower and upper asymptotes, $L_i$ and $U_i$, which are updated every iteration depending on information for the design variables from previous iterations. As a result, the values of these asymptotes are critical in determining the MMA optimization speed, direction, and quality of the minimum. More information on the details of these approximation functions can be referred to from the original MMA documentation by Svanberg [55].

An illustration of how the two asymptotes control a single variable two-iteration optimization process can be referred to from Figure 4.5. As observed in Figure 4.5a, with the initial definition of the asymptotes, the curvature of the approximate function is defined by the blue

line. Since the minimum of the approximation is lower than the optimal or objective for iteration one, in the next iteration, the asymptotes are shifted such that the new approximations are moved closer to the objective, which can be seen by the red line. The solution after the first iteration can be visualized from 4.5b, and given that a minimum is achieved, no further iterations are required [57].
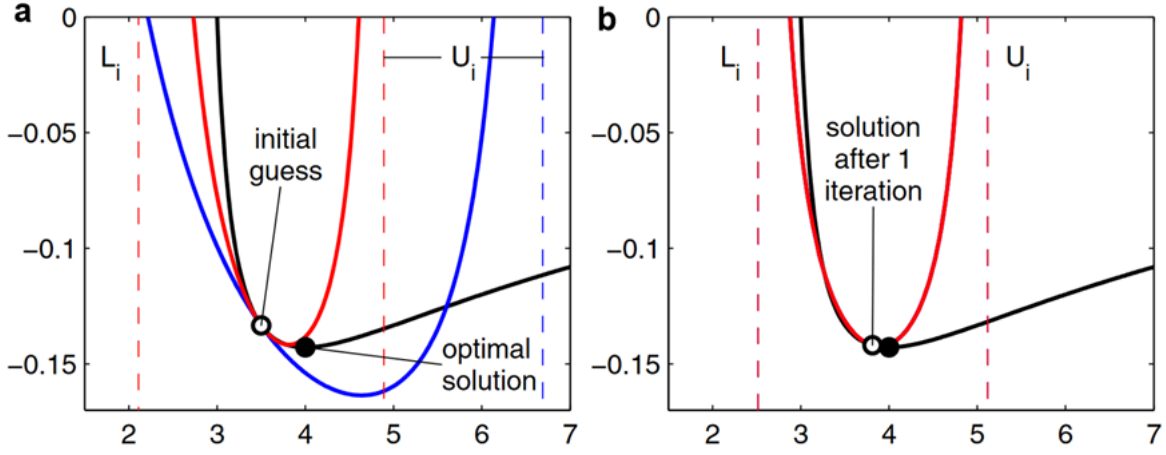


**Figure 4.5:** (a) For a two-iteration optimization problem, from the zeroth to the first iteration, the moving asymptotes of MMA $L_i$ and $U_i$ that control the curvature of the approximation function shown in blue move the initial guess of the optimization problem initially above the optimum solution, closer to the optimum solution. It does so by moving $U_i$ and modifying the curvature of the approximation function, shown in red. As a result, (b) shows the current solution after iteration 1 as approximately equal to the optimum solution [57].

The asymptotes for every iteration $L_j^{(k)}$ and $U_j^{(k)}$ are updated heuristically depending on whether the process is oscillating or moving monotonously and slowly. If the process oscillates i.e., $(x^k - x^{(k-1)})(x^{(k-1)} - x^{(k-2)}) < 0$, the asymptotes are defined such that they come closer to the current iteration value $x^k$. Conversely, if the process is moving monotonously and slowly, i.e., $(x^k - x^{(k-1)})(x^{(k-1)} - x^{(k-2)}) > 0$, the asymptotes are defined such that they move away from the current iteration value $x^k$.

The update of these asymptotes, considering the variations in the process progression with iterations, can be implemented as shown in Equations 4.26,4.27, and 4.28.

For first two iterations i.e., at $k = 0$, and $k = 1$, asymptotes are defined as,

$$L_j(k) = x_j^{(k)} - s_{ini}\left(x_j^{max} - x_j^{min}\right); \qquad U_j(k) = x_j^{(k)} + s_{ini}\left(x_j^{min} - x_j^{min}\right) \qquad (4.26)$$

Where, $s$ or $s_{ini}$ is the coefficient between zero and one, here, $s = 0.5$ as a standard, and $x_j^{min}$, $x_j^{max}$ are the lower and upper bounds of the design variable, $x_j$.

For all further iterations, i.e., $k > 2$, the equations to select the asymptotes change. When oscillations occur, and the optimization must be stabilized, we have the asymptotes defined as,

$$L_j(k) = x_j^{(k)} - s_{slow}\left(x_j^{(k-1)} - L_j^{(k-1)}\right); \qquad U_j(k) = x_j(k) + s_{slow}\left(U_j^{(k-1)} - x_j^{(k-1)}\right) \qquad (4.27)$$

Where $s$ or $s_{slow}$ is the coefficient between zero and one that moves the asymptotes closer to the current iteration value $x_j^{(k)}$. As a standard, this is set to $s_{slow} = 0.7$ [55].

When slow and monotonous convergence occurs, and the optimization must be relaxed, we have the asymptotes defined as,

$$L_j(k) = x_j^{(k)} - s_{fast}\left(x_j^{(k-1)} - L_j^{(k-1)}\right); \qquad U_j(k) = x_j^{(k)} + s_{fast}\left(U_j^{(k-1)} - x_j^{(k-1)}\right) \qquad (4.28)$$

Where $1/s$ or $s_{fast}$ is the coefficient that moves the asymptotes further away from the current iteration value $x_j^{(k)}$. As a standard, this is set to $s_{fast} = 1.2$ [55].

Besides the asymptotes to control the curvature of approximation functions, a move limit $'move'$ is defined to control the step size of the design variables. These move limits are directly applied to the design variable and their bounds. They control the smooth progression of the optimization. The implementation of the move limit for the design variables can be seen in Equation 4.29, where, as a standard, it is set to 0.5.

$$\begin{aligned}\alpha_j^{(k)} &= \max\left\{x_j^{\min}, l_j^{(k)} + 0.1\left(x_j^{(k)} - l_j^{(k)}\right), x_j^{(k)} - 0.5\left(x_j^{\max} - x_j^{\min}\right)\right\}, \\ \beta_j^{(k)} &= \min\left\{x_j^{\max}, u_j^{(k)} - 0.1\left(u_j^{(k)} - x_j^{(k)}\right), x_j^{(k)} + 0.5\left(x_j^{\max} - x_j^{\min}\right)\right\},\end{aligned} \qquad (4.29)$$

Here, $\alpha_j^{(k)}$ and $\beta_j^{(k)}$ determine the overall design variable step size and are assigned the maximum and minimum values from the set of three constraining expressions in Equation 4.29.

As a result, there are four important parameters for MMA that can directly impact the optimization characteristics, namely $s_{ini}$, $s_{slow}$, $s_{fast}$, and $move$. Tuning these parameters for best results is study and application-dependent. Hence, ascertaining which combination gives the best possible results for the MM-FATO framework requires further investigation and the same is done in Section 6.1.1.

## 4.1.7. Convergence Criteria

In any optimization problem, it is imperative to have a stopping point for the optimization algorithm. Ideally, the algorithm should stop when the objective function does not change significantly with further iterations or the change in design variables driving the objective between subsequent iterations is negligible or under acceptable tolerance. When that happens, we consider the model converged to acceptable results. Hence, for the current model, we define convergence criterion 1 (CC1) along similar lines, where MMA is assumed to have converged to a result if, between the two latest iteration steps $k$ and $k-1$, the relative change $R$ for each design variable $x_j$ to their bound constraints ($\overline{x}_j$ and $\underline{x}_j$) is below 1% or an absolute value of 0.01. The change $R$ can be mathematically expressed using the formula in Equation 4.30.

$$R = \left(\frac{x_j^k - x_j^{k-1}}{\overline{x}_j - \underline{x}_j}\right) \forall x_j \in \mathbf{X}; \qquad \mathbf{X} = \left\{\mathbf{x^{mat1}}, \mathbf{x^{mat2}}, \cos(\theta), \sin(\theta)\right\} \qquad (4.30)$$

When using discrete material optimization for multi-material interpolation, the goal is to have a single candidate material exist per element. This is considered to be achieved only when all the elements in the mesh have one of the material weights to be greater than the Euclidean norm of all the other material weights. These are the weights defined in Equation 4.14 for multi-material interpolation in Section 4.1.4. This implies that only if all the elements in the defined mesh satisfy this condition can the design be considered to converge satisfactorily.

Building upon this ideology, for this work, attainment of CC1 alone is deemed unsatisfactory, and we also define a DMO convergence criterion 2 (CC2) similar to the one defined by Stegmann and Lund [16], which first checks if each element has either one of the material

weights ($w_j$) greater than the Euclidean norm of all the weights for that element within a tolerance value $\epsilon$ of 95%, which can be expressed by Equation 4.31

$$w_j \geq \epsilon\sqrt{w_1^2 + w_2^2 + \cdots + w_m^2} \tag{4.31}$$

If such a weight exists for an element, that element is flagged as converged. The total number of flagged elements is then divided by the total number of elements in the mesh to derive the DMO convergence, $h_\epsilon$, as shown in Equation 4.32. When DMO convergence reaches the value one, i.e., all elements in the mesh are converged according to Equation 4.31, the optimization is considered to have successfully converged.

$$h_\epsilon = \frac{N_c}{N} \tag{4.32}$$

Where $N_c$ is the number of converged elements. So, in our case, if the DMO convergence denoted by $h_{95}$ achieves total convergence, i.e. $h_{95} = 1$, it means that each element in the mesh has a single material weight that contributes more than 95% to the Euclidean norm of all the material weight factors for that element. This implies that only one material is selected for each element, ensuring multi-material convergence.

Defining CC1 and CC2 lays the ground for the primary stopping conditions that we employ for our framework. Another criterion for convergence, convergence criterion 3 (CC3), is used to check discreteness, i.e., if the penalization has sufficiently pushed intermediate densities to 0-1. Discreteness in this work is defined as a quantitative evaluation of the 0-1 nature of the design. For instance, if the total number of elements with filtered densities greater than 0.2 and less than 0.9 is lower than 30 % or 0.3, the design is considered acceptable greyness. To express it as the design's discreteness or $D_g$, we can use Equation 4.33.

$$D_g = \frac{\sum_{i=1}^{N}\left(0.9 \leq \sum_{j=1}^{m} \tilde{x}_i^{matj} \leq 0.2\right)}{N} \times 100\% \tag{4.33}$$

A penalty continuation approach is used in this work to allow for a smooth transformation of the design space from convex to non-convex, which addresses the non-convexity resulting from the penalization of intermediate densities [58]. The optimization, as a result, starts with a penalty factor of one and keeps continuing in step sizes of 1 or 0.3 until all the convergence criteria, CC1, CC2, and CC3, are met. Since we start at low penalization values, which might be insufficient, CC1 is expected to be met at the end of each penalty step, but CC2 and CC3 are not. As a result, only when sufficient penalization step has been reached, and most intermediate densities are penalised enough to reach 0-1 densities, is the DMO convergence criterion close to one and/or discreteness convergence criterion CC3 met.

As a result, when implementing the convergence criteria for penalty continuation in MAT-LAB, the design variables are updated every iteration based on the soft convergence criteria CC1. When CC1 is met, a fixed penalty step size updates the penalty, and only at the end of each penalty step or before the start of a new penalty step are the design variables checked for CC2 and CC3.

Such an approach gives some flexibility in case no penalty continuation is implemented. Where the same implementation holds except for the continuation of the penalty step when CC1 is met. As a result, once CC1 is met, CC2 and CC3 are also determined, but most certainly, CC2 and CC3 might not be met when using a fixed penalty step. Nonetheless, for high enough penalty factors, high discreteness can still be achieved.

## 4.2. Evaluating Discreteness Post-Convergence

Using a density filter means that a significant number of intermediate values in the final design are still persistent along the perimeter of the optimized structure. Since the projection approach for discrete designs does not work well during optimization, in this work the preferred approach is the continuous reduction of the filter to improve discreteness. The density filter radius is reduced by 10% of the original value after CC2 or CC3 is met and till the value of the filter radius reaches one [47].

For the filter radius reduction approach, at every step of filtering, only CC1 is evaluated. If it is met, the density radius value is reduced by 0.1, and the optimization process is repeated using the new filter radius. Once the filter radius reaches a value of one, thresholding of the density design variables can be applied where elements with density values less than 0.5 are assigned a value of zero, and elements with density values greater than 0.5 are assigned a value of one. This approach can result in significantly higher discreteness while ensuring the overall convergence of all design variables within the design space.

However, this continuation approach to filter radius reduction adds many additional iterations to the optimization process. Provided sufficient convergence of density design variables is achieved, turning off the filter directly at the end instead of reducing it could also lead to the attainment of discrete designs with a significantly lower number of iterations. This was also done by Sanders et al. [42]. However, The same was found insufficient for many MM-FATO cases during a preliminary assessment. Removing the filter directly resulted in some unexpected void elements in unexpected regions. These void elements were observed in random topology regions surrounded by fully dense elements, which is undesirable. Hence, such an approach is not recommended to obtain discrete results with MM-FATO.

As an alternative, the Heaviside Projection method or HSM is also proposed to be implemented as a post-convergence update scheme. It can potentially provide more discrete designs than those obtained with the use of only a density filter and its subsequent reduction. For this work, the Heaviside projection parameter $\beta$ in Equation 4.2 is applied using a continuation approach, starting from 1 and increasing by a factor of 2 each time CC1 is met [47], [48]. However, the value of $\beta$ is limited to 16. For a number of trials on the MMA-modified version of PolyMat [42], 16 was found to be the most stable value for $\beta$. With any further increase, significant instabilities in the optimization process were observed. A comparative study to assess the performance and suitability of both discretization schemes for obtaining discrete results with MM-FATO is carried out later in Section 6.2.2.

## 4.3. Overview of Optimization

The MM-FATO framework developed in this work is depicted in Figure 4.6. The optimization process involves the following steps:

1. User provides parameters required for optimization.
2. An initial guess solution is generated using an array with a random or uniform angle field and equally weighted material density design variables.
3. Box constraints are assembled as an array with respect to the design variables.
4. Material density design variables are filtered to obtain mesh-independent results and prevent numerical instabilities like checkered boarding.
5. DMO multi-material interpolation scheme is used to determine the contribution of each material to the element constitutive matrix. This data, along with the FEM data for

the input load case, is used to calculate the compliance of the design domain.

6. MMA then uses the sensitivities of the objectives and volume constraints, the design variable array, compliance value, and all the constraints to determine the updated design variables that minimize the objective function. The sensitivity heat map in Figure 4.6 shows the process of determining which elemental design variables will reduce compliance the most.

7. The MMA results are then checked for convergence criteria CC1, CC2, and CC3. If CC1 is not met, the process is rerun with the current iteration's results as an updated design for the next iteration.

8. Once CC2 or CC3 is met, the filter reduction scheme for better discreteness highlighted in Section 4.2 is implemented. These steps are shown in the block of steps on the right side of Figure 4.6.

9. Lastly, if all convergence criteria are met, the results are post-processed for material mixing and smoothing fibre orientation, the latter of which is discussed in Section 4.1.3. The final illustration in Figure 4.6 visualizes this process.
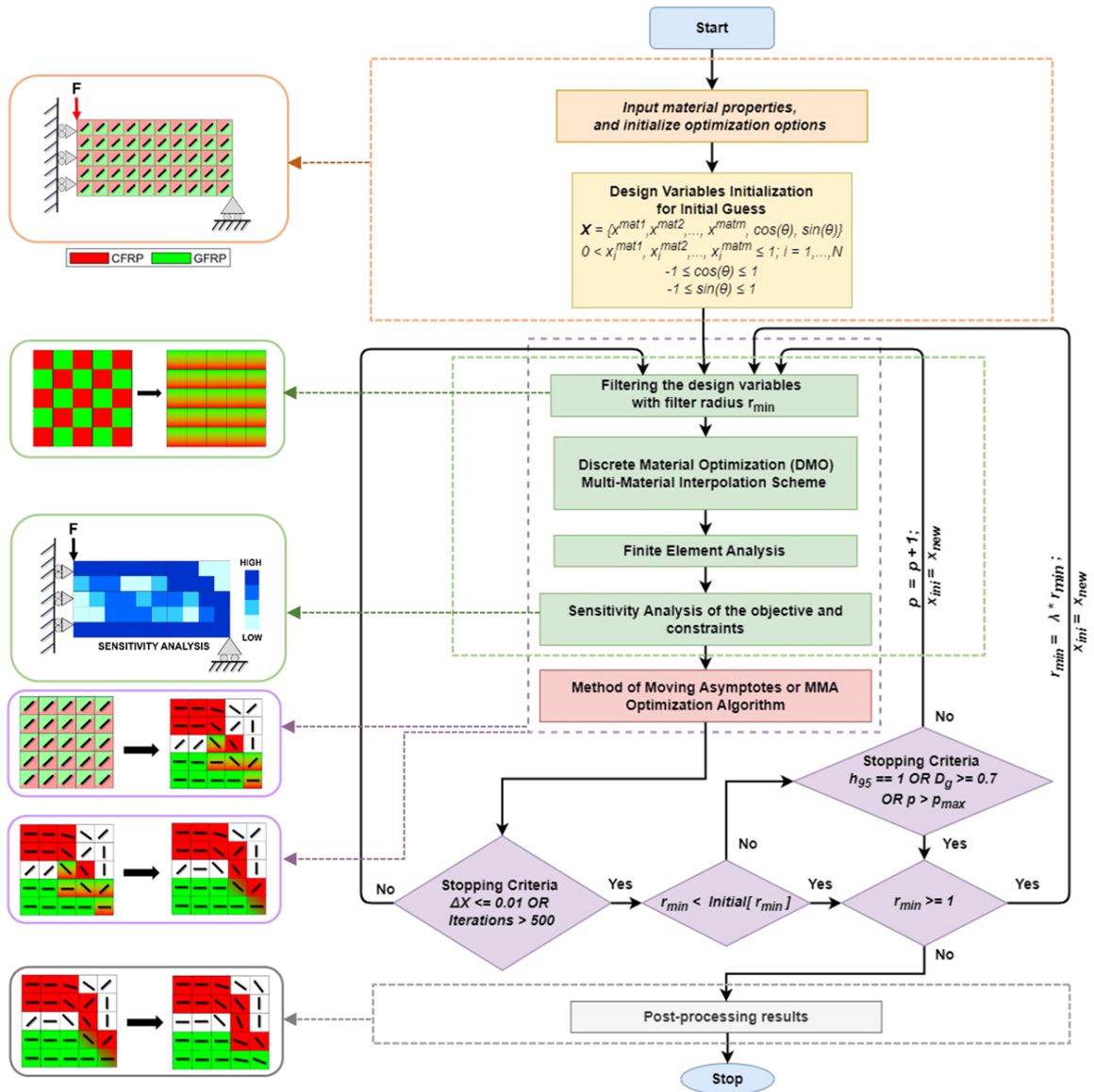


**Figure 4.6:** Flowchart illustrating the iterative process of MM-FATO. Important steps include user input, design initialization, filtering, FEA analysis for objective calculation, calculating sensitivities for MMA update, checking convergence criteria, discreteness improvement step, and lastly, post-processing of results.

<div style="text-align: right; font-size: 3em;">5</div>

# Framework Verification Tests

The MM-FATO framework discussed in the previous chapter is implemented in MATLAB. However, to test the framework's robustness, an extensive parametric study is conducted as a verification test. The goal is to assess the quality of optimized topologies and convergence achieved for varying input parameters and variations in the framework. All the different experiments designed for the parametric study, along with the methodology for assessing eco-efficiency, are detailed in this chapter. The results of both parametric and eco-efficiency studies are then detailed in the next Chapter 6.

## 5.1. Baseline Setup

A standard baseline setup is designed and described in this section. Unless stated otherwise, this is used for all the experiments and their results detailed in the upcoming sections. This setup evaluates an MBB beam with length, $L = 100$ mm and width, $W = 20$ mm. However, given the symmetry of the design domain, only the symmetric right half, termed the half-MBB beam load case, is solved to generate results. Symmetry causes the domain size to reduce to $L = 50$ mm and $W = 20$ mm for further optimization. This implication with the load and boundary conditions for the MBB beam can be seen in Figure 5.1a. As observed, a point load $F = 1000$ N acts at the top-left corner of this symmetric simply supported beam. The design domain is further discretized by 4-node quadrilateral mesh elements where each element has a side length, *elSize* of 1 mm.
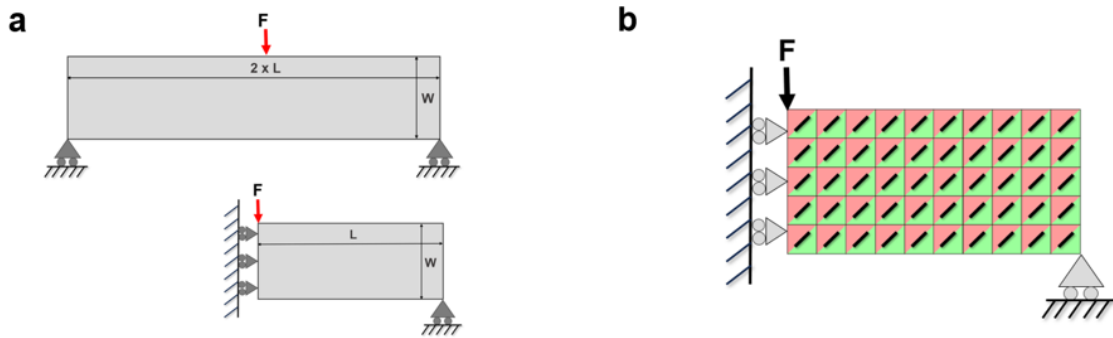


**Figure 5.1:** (a) A 50 x 20 mm design domain with loads and boundary condition used for result generation in this section, (b) Discretized form of design domain with 50 x 20 elements or element size of 1 mm, and a uniform angle field along with equal design volume fractions of the two materials of 0.2 as an initial guess.

As a standard, only two materials, carbon-fibre-reinforced polymer (CFRP) and glass-fibre-reinforced polymer (GFRP), are considered for optimization. These properties are indicated in Table 5.1 and are directly adapted from Duan et al., [32].

**Table 5.1:** The standard material properties for unidirectional composite materials, CFRP and GFRP, retrieved from existing literature. These properties have been utilized previously by Duan et al. [32] to evaluate the MMCAP model and are adopted for the parametric analysis in the forthcoming sections.

| Material | $E_x$ $(MPa)$ | $E_y$ $(MPa)$ | $\nu_{xy}$ | $\nu_{yx}$ | $G_{xy}$ $(MPa)$ | $\rho$ $(Kg/m^3)$ |
|----------|---------------|---------------|------------|------------|------------------|-------------------|
| CFRP | 90000 | 6500 | 0.30 | 0.0217 | 6500 | 1800 |
| GFRP | 30000 | 9500 | 0.28 | 0.0887 | 4500 | 2100 |

The occupied design volume fractions for CFRP and GFRP materials are fixed at $\Omega_1$ 0.1 or 10% for CFRP and $\Omega_2$ 0.2 or 20% for CFRP. An equal value of 0.2 is the initial guess for both density design variables. A uniform angle field with an angle of 45° is the initial guess for the two material design elements as seen in Figure 5.1b. However, a random orientation field with each mesh element having randomly aligned fibre as an initial guess is also considered for certain tests.

For filtering the density design variables, a density filter with radius $r_{min} = 2$ mm is used. A penalty continuation approach is applied where the initial penalty is set to one, and the penalty is increased until the maximum penalty of six is reached, with a step size of one. 500 is the limit set for the maximum number of iterations per penalty step for stopping criteria. The design variables are updated using the standard empirical MMA parameters from Svanberg [56] and are used as a starting point for the parametric study. This implies a move limit *move* of 0.5 and factors $s_{init}$, $s_{slow}$, and $s_{fast}$ equal to 0.5, 0.7, and 1.2, respectively.

Furthermore, the optimization steps for density filter reduction to improve discreteness are not considered for any of the presented results unless stated otherwise. For post-processing, fibre-angle filtering is done with a filter radius 1.5 times the density filter radius $r_{min}$, and the post-processing step mentioned in Section 4.2 is implemented to avoid material mixing.

An overview of all the standard input parameters used for the MM-FATO framework can be seen from Table 5.2. All the computations reported in this work are performed on a 64-bit Windows 11 laptop with an AMD Ryzen 7 5800H @ 3.2 GHz CPU and 16 GB of SSD RAM.

**Table 5.2:** Input parameters used for the MM-FATO implementation and their standard values

| Input Parameter | Default values used for the parameter |
|-----------------|----------------------------------------|
| $\Omega_f$ | Allowed volume fraction to be occupied in the design domain by both materials. |
| $\Omega_1, \Omega_2$ | Allowed volume fraction of material one and two in the design domain, 0.1 and 0.2 respectively. |
| $evalIter$ | Maximum Number of Iterations per penalty step = 500. |
| $r_{min}$ | $r_{min} = 2$ to limit the minimum feature size to 2 mm for an element size of 1mm. |
| $r_{cur}$ | $r_{cur} = 3$ to smooth fibre orientations, considered as $1.5 \times r_{min}$. |
| $p$ | DMO penalty factor, updated after soft convergence criteria is met, $(p_0 = 1; \Delta p = 1; p_{\max} = 6)$. |
| $nelx, nely$ | $(50, 20)$ finite mesh elements along $x$ and $y$ directions respectively. |
| $elSize$ | Single element side length along $x = y = 1$ mm. |
| $c_i$ | Coefficient for the artificial variable $y$ equal to 10000. |
| $move$ | Step size or move limit of 0.5 for design variables in the MMA solver. |
| $s_{init}$ | Initial factor of 0.5 for determining the lower and upper asymptote position. |
| $s_{slow}$ | Factor of 0.7 to tighten the asymptotes post three major MMA iterations. |
| $s_{fast}$ | Factor of 1.2 to relax the asymptotes post three major MMA iterations. |
| $lambda$ | Density filter reduction factor = 0.9 used for obtaining more 0-1 designs |
| $voidThr$ | Threshold for the percentage of elements below a filled density of 0.2 |
| $filledThr$ | Threshold for the percentage of elements above a filled density of 0.9 |
| $thresh$ | Overall greyness threshold of 0.3 below which obtained designs are acceptable |
| $\beta$ | Projection parameter for Heaviside projection of density variables |

## 5.2. Design of experiments for parametric study

### MMA empirical parameters

As established previously, MMA requires a significant amount of input from the user to solve the problem at hand. Several of these parameters need further tuning to obtain feasible solutions and a numerically stable optimization process for this problem. Some guidelines to fine-tune the MMA parameters have been laid down in the original [55] and subsequent modified [56] MMA documentation. These guidelines are used as a starting point to determine the best parameter combination before further heuristic evaluation.

The input parameters that needed to be adapted for our work include the objective function, the index $c_i$ corresponding to the artificial variable $y$, and the empirical parameters $move$, $S_{init}$, $S_{fast}$, and $S_{slow}$. Following the guidelines stated in [56], the objective function in this work is scaled by $1 \times 10^{-3}$ to ensure that the condition $0 < f_0 < 100$ is satisfied. Similarly, $1 \times 10^6$ as the value for $c_i$ was found suitable to achieve negligible values of the artificial variable $y_i$ after a trial-and-error exercise.

However, implementing the baseline combination of MMA parameters, oscillations in the order of $10^2$ for the intermediate results were observed during the first 5-10 iterations. Such an initial behaviour is undesirable because it can lead to optimization difficulties for certain initial guesses. As a result, the baseline MMA parameters are not considered to create a more robust framework. As a heuristic experiment in this work, the empirical parameters are modified to see which combination gives the best possible solution for Equation 4.25. For this hit-and-trial scheme, we define five combinations of the empirical MMA parameters.

In the first set, we only reduce the *move* parameter to limit the amount the design variables can move from their current value and not run into infeasible solutions. It is reduced to a moderate 0.1 to see if a feasible solution can be achieved and to evaluate the quality of the local optima. In the second set, we reduce the $s_{init}$ factor to bring the asymptotes closer to the design variable, creating a conservative bound only for the first few iterations. In the third set, we reduce both the initial bound by taking asymptotes closer using $s_{init} = 0.1$ and the step size by limiting the move limit of the design variable *move* to 0.1. For the fourth set, we further reduce the move limit *move* to 0.05 to get a more conservative step size while keeping the rest of the parameters the same as the baseline. For the most conservative combination, which is the fifth and final set, all the parameters are set to a minimum where $move = 0.05$, $s_{init} = 0.1$, $s_{fast} = 1.1$ and $s_{slow} = 0.1$.

For the CFAO approach chosen, the initial guess has a significant impact on the optimization results. Hence, the five MMA parameter combinations are evaluated for two different initial guesses, random orientation field and uniform orientation field. The results for this set of experiments are reported in Section 6.1.1.

### Material Property

To better understand the implications of using different material properties on the MM-FATO framework, a parametric study for varying material properties that define the material's anisotropy is carried out. This is done on a single material fibre angle topology optimization (SM-FATO) framework first to understand the isolated impact of the fibre angle optimization approach on the results.

To understand the limitations and the scope of the current CFAO implementation on the final fibre orientations for the SM-FATO framework, we evaluate the effect of changing the ratio of longitudinal to transverse stiffness ($E_x/E_y$) and the impact of varying the shear modulus ($E_x/G_{xy}$) of the composite on the optimized results. To also consider the effect of material stiffness in this evaluation, two materials, CFRP with higher stiffness and GFRP with lower stiffness, from Table 5.1 are used as a baseline.

To further understand the influence of in-plane shear modulus $G_{xy}$ on CFAO and the obtained topology, we evaluate the shear stiffness of the material. The measure used to determine the shear stiffness of the material is defined by $\psi$ [59], [60], and can be expressed as shown in Equation 5.1.

$$\psi = \frac{E_x}{1 - \nu_{xy}\nu_{yx}} + \frac{E_y}{1 - \nu_{xy}\nu_{yx}} - 2\frac{\nu_{xy}E_y}{1 - \nu_{xy}\nu_{yx}} - 4G_{xy} \tag{5.1}$$

Where, $\psi \geq 0$: Shear weak material, $\psi < 0$: Shear strong material, & $\psi = 0$: Isotropic material. An in-depth review of the parametric study results evaluated for variations in material properties is reported in Section 6.1.2.

### Convergence Study

To evaluate the convergence of the topologies obtained using MM-FATO, an investigation of the convergence quality by examining the impact of fixed penalization scheme and penalty continuation scheme on the convergence characteristics like DMO convergence $h_{95}$ and discreteness $D_g$ is necessary.

An important parameter to assess for convergence study is the penalty step. The step size dictates the increase in convexity during the optimization. Ideally, we want the penalty step to be as small as possible to have a smooth convex to non-convex transformation. This is per the recommendations underlined in the work of [58] as well. The study reiterates through experiments how a smaller step size of 0.1-0.3 is beneficial when using penalty continuation.

However, when a very small step size is selected, it is often observed that the number of iterations increases significantly. To avoid this, a balance between iterations and quality of results in terms of topology, $h_{95}$ and greyness must be maintained. Hence, we limit the minimum step size that will be evaluated to a moderate value of 0.3. Results of the convergence study are detailed in Section 6.1.4.

### Mesh Dependency

The quality of the finite element mesh used directly impacts topology optimization results. Finer meshes generate better results due to higher data points, contributing to more accurately evaluating the objective function and state variables. However, refining the mesh beyond a certain point may not improve accuracy or local optima and increase computation costs.

With increasing mesh size, an increase in the computation time per iteration of the MMA solver is expected, given that increased elemental stiffness matrix assemblies must be carried out, which is one of the most computationally intensive tasks in the MATLAB implementation. Therefore, it is imperative to determine a mesh size that balances computational efficiency and accuracy.

The MM-FATO framework includes a density filter to ensure mesh-independent results, and to test the efficacy of the same, results are evaluated for four mesh sizes with increasing re-

finement. This includes mesh sizes of 50 x 20, 80 x 32, 100 x 40 and 200 x 80. The detailed results obtained are detailed in Section 6.1.5.

# 5.3. MM-FATO and Eco-efficiency

To answer the second sub-research question from Section 2.7, an eco-efficiency assessment of the optimized structures obtained from MM-FATO is carried out. Where the $CO_2$ footprint and compliance results for MM-FATO will be evaluated and compared to those from the SM-FATO framework. This SM-FATO approach is similar to the one developed by Almeida [6]. However, to achieve a meaningful comparison between both frameworks, we modify the SM-FATO approach of Almeida [6] to use MMA instead of *fmincon*. This section details the methodology for assessing the eco-efficiency of results achieved using the MM-FATO framework.

## 5.3.1. Database for $CO_2$ footprint evaluation

To assess the $CO_2$ footprint of composite materials that can be created using AM, a database similar to one by Almeida [6] is created. This database contains a mix of bio-based and oil-derived matrices and natural and synthetic fibres. This study considers two matrices and six fibres. Their properties are obtained and reported directly from "Granta Edupack." The database of these constituent materials and their properties can be seen in Table 5.3.

**Table 5.3:** Material property table for a mix of natural and synthetic fibres that can be used with two commonly available matrices for fabricating composites

| Type | Material | $\rho$ $(Kg/m^3)$ | $E$ $(GPa)$ | $G$ $(GPa)$ | $\nu$ | $CO_2^{mat}$ $(Kg/Kg)$ |
|---|---|---|---|---|---|---|
| **Fibres** | Bamboo | 700 | 17.5 | 1.29 | 0.39 | 1.0565 |
| | Flax | 1470 | 53.5 | 1.41 | 0.355 | 0.44 |
| | Hemp | 1490 | 62.5 | 1.6 | 0.275 | 1.6 |
| | Carbon High Modulus | 2105 | 760 | 340 | 0.105 | 68.1 |
| | Carbon Low Modulus | 1820 | 242.5 | 105 | 0.105 | 20.3 |
| | S-Glass | 2495 | 89.5 | 33 | 0.22 | 2.905 |
| **Resins** | PLA | 1260 | 3.45 | 1.245 | 0.39 | 2.28 |
| | Epoxy | 1255 | 2.41 | 0.86 | 0.399 | 5.94 |

For all the possible combinations of matrix and fibres from Table 5.3, the equivalent composite material properties are analytically calculated. Empirical formulas, such as the Rule of Mixtures (ROM) and Inverse Rule of Mixtures (IROM) for continuous fibre composites, are used to determine mechanical properties like longitudinal and transverse tensile modulus, $E_x$ and $E_y$, shear modulus, $G_{xy}$, density, and major Poisson's ratio, $\nu_{xy}$. $\nu_{yx}$ or minor Poisson's ratio is calculated based on the correlation between longitudinal and transverse tensile modulus for a transverse isotropic material, $E_x \times \nu_{yx} = E_y \times \nu_{xy}$. These calculations can be referred to from Equations 5.2-5.3. Where the subscript $m$ is used to indicate matrix property, the subscript $f$ is used to indicate fibre property and the volume fraction $V_f$ is set to 0.4 in this study for the fibres.

Rule of Mixtures for $E_x$ = Longitudinal Stiffness, and $\nu_{xy}$ = Major Poisson's Ratio,

$$E_y = E_f V_f + E_m \left(1 - V_f\right); \qquad \nu_{xy} = \nu_f V_f + \nu_m \left(1 - V_f\right) \qquad (5.2)$$

Inverse Rule of Mixtures for $E_y$ = Transverse Stiffness, and $G_{xy}$ = In-Plane Shear Modulus,

$$\frac{1}{E_y} = \frac{V_f}{E_f} + \frac{(1 - V_f)}{E_m}; \qquad \frac{1}{G_{xy}} = \frac{V_f}{G_f} + \frac{(1 - V_f)}{G_m} \tag{5.3}$$

## 5.3.2. Calculating $CO_2$ footprint

To calculate the carbon footprint of the resultant SM-FATO and MM-FATO designs, we make use of the Ashby material index derived in the work of Duriez et al. [61]. In their work, it was derived to evaluate the carbon footprint of a simple Asbhy beam. Like in [61], in this work as well, we only consider the footprint of the material production and the use phase for the optimized beam for simplicity. The calculations for the total $CO_2$ footprint of the structure with a given material combination, considering the two life-cycle phases, are detailed in this section. However, it is important to note that the impacts of other phases, such as end-of-life and manufacturing, are significant and must be considered for more representative results of $CO_2$ footprint.

For the embodied $CO_2$ footprint of the material, we define $CO_2^{mat}$, calculated as shown in Equation 5.4.

$$CO_2^{mat} = M \times CO_{2mat}^i \tag{5.4}$$

Where, $CO_{2mat}^i$ is the $CO_2$ intensity of the composite material derived using Equation 5.5.

$$CO_{2mat}^i = \frac{CO_{2,f}^i \rho_f + CO_{2,m}^i \rho_m}{\rho_{mat}} \tag{5.5}$$

In Equation 5.4, M represents the structure's mass under consideration, given by $M = v_e \times x_e \times \rho_{mat}$. Where $v_e$ is the single mesh element volume, $x_e$ is the volume occupied by one of the material density design variables, and $\rho_{mat}$ is the density of the composite material implied by the material density design variable occupying $x_e$. $\rho_{mat}$ can also be derived using ROM as expressed by Equation 5.6.

$$\rho_{mat} = \rho_f V_f + \rho_m (1 - V_f) \tag{5.6}$$

To evaluate the $CO_2$ footprint of the structure concerning its use phase, $CO_2^{use}$ is used. It measures the carbon footprint in $kg$ $CO_2$ emissions generated to transport a structure with mass $M$ on a long-haul aircraft over its service life of 25 years. $CO_2^{use}$ is defined according to Equation 5.7 [61].

$$CO_2^{use} = M \times CO_2^{veh} = M \times CO_2^{fuel} \times FRC \tag{5.7}$$

Where $CO_2^{veh}$ represents the kilograms of $CO_2$ emitted when transporting a kilogram of the structure over the aircraft's service lifetime of 25 years. Represented by $CO_2^{fuel}$, which is kilograms of $CO_2$ emitted by burning a kilogram of jet fuel, and the fuel reduction coefficient or $FRC$, which is the amount of jet fuel burnt to transport a kilogram of this structure over its lifetime of 25 years. For this work, $FRC$ is assumed to have a value of 4800 kilograms of jet fuel consumption per kilogram of the structure over 25 years. This is based on the $FRC$ value reported in the LCA study by Deng [62], which equals 17.2-21.2 tons/(100kg*year) of jet fuel for a long-haul aircraft. Similarly, a value of 3.16 kg $CO_2$/kg jet-fuel was determined for $CO_2^{fuel}$ [1].

In conclusion, when considering only the material and use phase of the structure, the total $CO_2$ footprint of the structure, $CO_2^{tot}$, can be expressed as shown in Equation 5.8.

$$CO_2^{tot} = CO_2^{mat} + CO_2^{use} = M \times \left( CO_{2mat}^i + CO_2^{veh} \right) \tag{5.8}$$

### 5.3.3. Design of experiments for $CO_2$ impact study

A simple design of experiments is chosen to evaluate any possible improvement in the total $CO_2$ footprint of a topology-optimized structure with multiple composite materials. For the two-material optimization, one of the materials is fixed as the material with the desired compliance, for instance, some volume fraction of carbon fibres in the PLA (poly-lactic acid) matrix. The second material chosen is one of the natural fibres from the same Table 5.3 in the same matrix.

Two variations are considered for result generation with the current implementation of MM-FATO. The first includes MM-FATO results obtained by varying the fibre volume fraction of the multi-material system. The second includes MM-FATO results obtained by varying the ratio occupied fraction by materials 1 and 2 in the design domain, $\Omega_1/\Omega_2$. The first variation is intended to improve the structure's compliance by increasing the fibre volume fraction. The second variation is intended to achieve a profile of how the different ratios of the volume occupied in the design domain by the two materials affect the carbon footprint and compliance. In all cases, the total occupied volume fraction by both materials is kept the same, i.e., $\Omega_f = 0.3$. The MM-FATO results are then compared with the SM-FATO ones that were achieved using the same fixed value for the occupied volume fraction, $\Omega_f$.

Lastly, the MM-FATO results are compared to the SM-FATO results obtained using the $\Omega_f$ values that give the lowest $CO_2$ footprint. A lower $\Omega_f$ would imply lower mass, leading to a lower overall $CO_2$ footprint for the optimized structure when Equation 5.8 is used. The results for these experiments and their implication on the eco-efficiency of optimized structures are detailed in Section 6.4.2.

# 6

# Results and Analysis

In this section, the framework is verified for robustness. This is done by assessing how variations in the input parameters affect the optimization results obtained. The output parameters evaluated primarily include the obtained topology and objective function values for each combination of input parameters tested. Intermediate outputs are also evaluated for preliminary analysis results but are specific to the test case and not generalized here.

Once we have verified the framework for robustness, the framework's performance is also analyzed. One of the objectives was to test the hypothesis that using multiple composite materials can produce structures with more rigidity and a lower overall $CO_2$ footprint. To assess this objective, the achieved compliance and $CO_2$ footprint results are compared to the results of the modified filtered-CFAO framework of Almeida [6].

## 6.1. Parametric Study for Input Parameters

For the parametric study, we first evaluate the MMA empirical parameters. The influence of these parameters is evaluated for two different initial guesses, namely, uniform orientation field initial guess and random orientation field initial guess. Once we have finalized a set of MMA parameters, we assess the frameworks sensitivity to material properties. This is done by evaluating the impact of varying $E_x$,$E_y$ and $G_{xy}$ values on the optimized topologies. We also determine the limiting occupied volume fractions $\Omega_1/\Omega_2$ of each material that can be used for the MM-FATO framework. Next, convergence parameters like discreteness and DMO convergence are evaluated for varying penalization parameters such as step size and maximum penalty factor. Lastly, we conduct a mesh-refinement study to see the effectiveness of the filtering scheme in reducing mesh dependency.

### 6.1.1. Influence of MMA Solver Parameters

**Uniform Orientation Field as Initial Guess**

To ascertain which MMA empirical parameter combination works the best for the MM-FATO framework, the impact of varying the parameters for a uniform orientation field is studied first. For the five combinations stated earlier, the compliance before and after post-processing and the iterations taken for each combination for an initial angle of 45° is reported in Table 6.1.

For trial 1, results in Table 6.1 show that changing the *move* parameter to 0.1 gives the best result in terms of compliance or objective function achieved, with a value of 17.0 N.m. However, the number of iterations taken is higher compared to other trials. Specifically, trial

4 has the lowest number of iterations for a smaller move limit of 0.05. This lower iteration can be attributed to the limited step size of the fibre angle design variables, which leads to more controlled convergence to a local minimum.

**Table 6.1:** Values for compliance and iterations for MM-FATO framework using the MMA empirical parameter combinations 1-5, and a uniform orientation field with $\theta = 45°$ as an initial guess.

| Trial | $move$ | $S_{init}$ | $S_{fast}$ | $S_{slow}$ | $f(x)$ **(N.m)** | $\tilde{f}(x)$ **(N.m)** | **Iterations** |
|---|---|---|---|---|---|---|---|
| 1 | 0.10 | 0.5 | 1.2 | 0.7 | 17.0 | **20.2** | 1487 |
| 2 | 0.50 | 0.1 | 1.2 | 0.7 | 26.3 | 33.7 | 1285 |
| 3 | 0.10 | 0.1 | 1.2 | 0.7 | 24.1 | 29.9 | 1578 |
| 4 | 0.05 | 0.5 | 1.2 | 0.7 | 24.1 | 30.1 | **1270** |
| 5 | 0.05 | 0.1 | 1.1 | 0.1 | 26.4 | 32.3 | 1315 |

*\* f(x) are compliance results before post-processing, and $\tilde{f}(x)$ are compliance values after post-processing*

However, to avoid premature convergence, a moderate step size should be considered for the design variables. Another reason to avoid smaller step sizes is to prevent the over-influence of initial angle guesses on the optimized results. Due to the small initial step size, the solver may follow a sub-optimal local minimum path. Hence, always reducing step size is not ideal. However, for this framework, both the move limit values of 0.1 and 0.05 give acceptable results.

Having established the MMA parameter combination 1 as the one that gives the lowest compliance for an initial angle of 45°, we also assess other uniform angle field values as initial guesses. The non-convexity of the CFAO optimization results in different local minima based on the initial guess. This makes it imperative to determine if a better local minima exists for the same MMA parameter combination. If it does exist, then we must also determine the improvement in the optimized results. The same MMA parameter combination 1 is further evaluated for eight other initial uniform angle fields to assess this. The results for compliance before and after post-processing are reported for all the nine angles, including 45°, which can be seen in Table 6.2.

**Table 6.2:** Values for compliance and iterations for MM-FATO framework for different uniform orientation fields, with angles between -90° and +90° as an initial guess. All results are generated using MMA empirical parameter combinations 1. Where, $move = 0.1$, $S_{init} = 0.5$, $S_{fast} = 1.2$, and $S_{slow} = 0.7$.

| Parameters | $-90°$ | $-70°$ | $-45°$ | $-30°$ | $0°$ | $30°$ | $45°$ | $70°$ | $90°$ |
|---|---|---|---|---|---|---|---|---|---|
| $f(x)$ **(N.m)** | 18.88 | 17.58 | 16.78 | 16.68 | **16.57** | 17.86 | 17.05 | 19.33 | 17.82 |
| $\tilde{f}(x)$ **(N.m)** | 24.19 | 21.56 | 19.62 | 19.96 | 19.52 | 21.90 | 20.20 | 23.31 | 21.88 |
| **Iterations** | 1365 | 1311 | 1608 | 1487 | 1503 | 1197 | 1487 | 1604 | 1856 |

As seen in Table 6.2, with varying initial angles, the compliance varies but is still overall lower than what is achieved using other MMA parameter combinations. Of all the limited initial angles tested, the initial angle field with all the angles assigned a value of zero gives the lowest compliance. For a simple load case like the one once considered, it is easier to trace a load path for loads and support and have an average initial orientation along the same lines, which could potentially give better results. However, for more complex load cases, a multi-start or global search strategy with multiple runs with different initial guesses is the only viable option when considering a uniform angle field.

A better local optimum can be obtained by simultaneously evaluating more varied initial guesses. This would mean increased computational costs for such a global search. However, using parallelization and clusters can significantly reduce computational time.

### Evaluating the post-processed results

As observed in the results so far, the values of compliance obtained after post-processing are higher than before post-processing. To understand the difference between the compliance achieved before and after post-processing, we determine what contributes more significantly, namely, the fibre smoothing or the removal of material mixing at the interface. The same can be visualized in Figure 6.1.
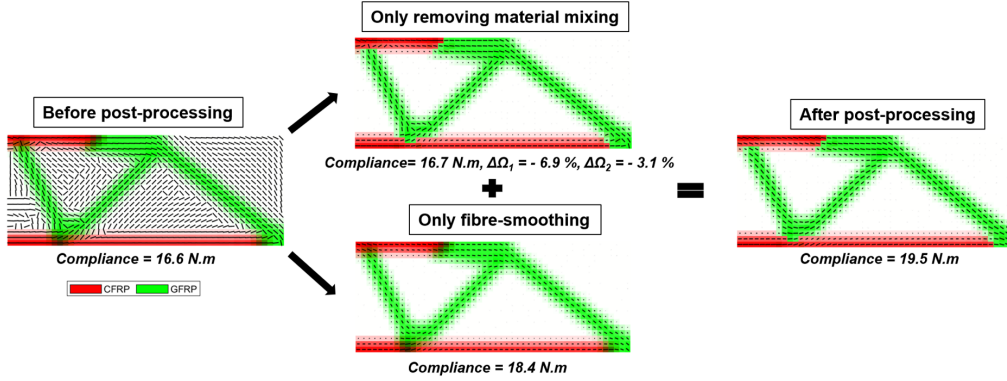


**Figure 6.1:** Post-processing the obtained topology at the end of convergence for material mixing and smoothing the fibre angles adds to the compliance. A total increase in compliance of 17.8 % is observed, of which the fibre smoothing contributes the most due to changes in the optimal orientations for less-optimal but more continuous ones.

As expected, the material mixing does not increase the compliance significantly. It was expected to increase the stiffness overall, given that removing material mixing is penalised in the DMO2 approach according to Figure 3.3, causing a less stiff interface. However, The slight increase can be attributed to a slight lowering in the design volume fraction of the two materials by approximately 6.4 % and 3 %. This is due to a decrease in the value of elemental densities from greater than one in the interface elements to one. Fibre smoothing, on the other hand, majorly causes the increase in compliance. This can be explained by the modification of fibre orientations at the intersection of individual beams with material loaded in shear, where the optimizer oriented fibres such that the structure has the lowest compliance. When slight modifications to many such fibres are done to obtain continuity, the intersections probably become weaker in shear, reducing the stiffness of the overall structure.

### Random Orientation Field as Initial Guess

To gain further insights into the characteristics of the *move* parameter for this framework, we repeat the trials for a random angle field as an initial guess. Such an initial guess reduces the high dependence of CFAO on initial orientations. Further, it can obtain more repeatable results every new optimization run, as discussed in Section 4.1.2. This exercise will use three different random orientation fields as starting points. The compliance and iterations to convergence for the three optimizations with different starting points at each empirical parameter combination are averaged and reported in Table 6.3.

We can observe from Table 6.3 how, as the more conservative the MMA parameters get, the less standard deviation in the compliance results is achieved. The obtained compliance

**Table 6.3:** Values for averaged compliance and iterations and the standard deviations for MM-FATO using the five MMA empirical parameter combinations 1-5. Three different instances of the random initial field for fibre orientations were used for averaging per trial 6-10, corresponding to the parameter combinations 1-5.

| Trial | $move$ | $S_{init}$ | $S_{fast}$ | $S_{slow}$ | Average $f(x)$ (N.m) | Average Iterations | $\pm$SD $f(x)$ |
|-------|--------|-----------|-----------|-----------|----------------------|--------------------|----------------|
| 6 | 0.10 | 0.5 | 1.2 | 0.7 | 18.9 | 1850 | 1.5 |
| 7 | 0.50 | 0.1 | 1.2 | 0.7 | 19.3 | 1386 | 2.3 |
| 8 | 0.10 | 0.1 | 1.2 | 0.7 | **17.8** | 1535 | 1.7 |
| 9 | 0.05 | 0.5 | 1.2 | 0.7 | 18.2 | 1698 | 0.7 |
| 10 | 0.05 | 0.1 | 1.1 | 0.1 | 18.3 | 1605 | 0.4 |

*\* f(x) or compliance results are reported for unfiltered fibre angles, i.e., before post-processing.*

is observed to have a standard deviation in the range of $\pm2.3$ to $\pm0.4$ over different MMA empirical parameter combinations, from the least to the most conservative. Keeping in line with the requirements of robustness and less sensitivity to initial guess, the more conservative combination of MMA empirical parameters might be a better solution. Furthermore, using a more conservative combination does not influence the number of iterations as per the results in Table 6.3, which is beneficial in terms of the computational efficiency of the framework. However, too small of a step size can be detrimental to the quality of local optima achieved [7]. Hence, it should not be reduced below 0.1 or 0.05 as a recommendation.
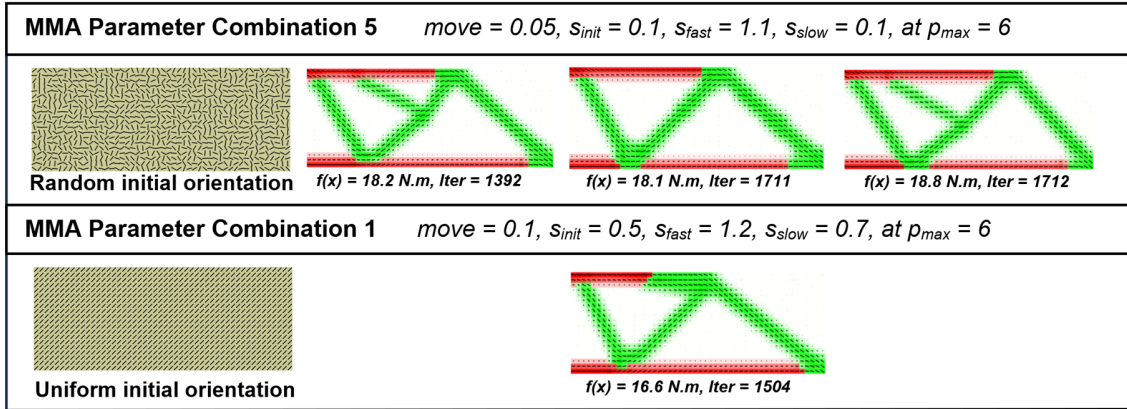


**Figure 6.2:** Comparing the topologies and compliance obtained for the three trials with random orientation field as an initial guess to the topology for the uniform orientation field initial guess at 0°. 0° uniform angle field gives the lowest compliance overall using a different MMA parameter combination.

On further evaluating the results for Trial 6-10, it was found that the topology obtained for the three different random orientations trials, at the same MMA parameter combination, differ to some extent. To provide a better understanding of the topologies obtained from three different initial guesses for the MMA empirical parameter combination, please refer to Figure 6.2. For this exercise, combination one, which had the lowest compliance in the previous trial at a starting angle of 0°, and the most conservative combination five for the random orientation field are illustrated.

The difference in topologies for even the most conservative approach when using random starting angles can be attributed to the non-convexity in the fibre optimization framework itself. This could occur when penalty continuation is applied to reduce starting non-convexity, but filtering or regularising the fibre orientation design variables is not done as recommended [52].

However, as observed in Figure 6.2, the topology obtained with random orientation for a moderate maximum penalty size of six gives manufacturable topologies with slightly sub-optimal local minima compared to a uniform guess design, i.e. an increase in -8.34% in the objective value. The benefit, however, is in the computational time, where three trails with random orientation angles with average iterations per run of 1605 compared to nine optimization runs for uniform orientation filed as an initial guess with iterations per run of 1504 are required.

Hence, in the context of this work, the more conservative empirical parameter combination where $move = 0.05$, $S_{init} = 0.1$, $S_{fast} = 1.1$, and $S_{slow} = 0.1$ for a convergence tolerance of 1%, with random orientations as initial guess is deemed satisfactory to provide more robust and computationally efficient optimization results. However, ways to reduce the variation in topology and compliance when using random starting guesses must be explored.

## 6.1.2. Material Property Influence

Five different ratios are considered for each material when evaluating the $E_x/E_y$ ratio for the two materials. Table 6.4 reports the compliance obtained for these five ratios.

**Table 6.4:** Compliance obtained for five $E_x/E_y$ ratios each for two base materials, CFRP and GFRP with different shears stiffness and longitudinal stiffness

| Material | $E_x$ (GPa) | $E_y$ (GPa) | $E_x : E_y$ | $f(x)$ (N.m) | Material | $E_x$ (GPa) | $E_y$ (GPa) | $E_x : E_y$ | $f(x)$ (N.m) |
|---|---|---|---|---|---|---|---|---|---|
| | 90 | 6.5 | 13.9:1 | **5.7** | | 30 | 2 | 15:1 | **16.3** |
| | 90 | 15 | 6:1 | 6.9 | | 30 | 5 | 6:1 | 23.5 |
| **CFRP** | 90 | 30 | 3:1 | 8.3 | **GFRP** | 30 | 9.5 | 3.2:1 | 25.0 |
| | 90 | 45 | 2:1 | 9.8 | | 30 | 15 | 2:1 | 22.0 |
| | 90 | 90 | 1:1 | **5.5** | | 30 | 30 | 1:1 | **16.6** |

$E_x : G_{xy} = 13.9{:}1$ for CFRP and $E_x : G_{xy}{=}6.7{:}1$ for GFRP, and f(x) or compliance results are reported for unfiltered fibre angles, i.e., before post-processing.

From the table, we have two ratios that give significantly lower compliance than other ratios for CFRP and GFRP. One of them is with the highest ratio between $E_x$ and $E_y$. This aligns with better results for the transverse isotropic model, where the longitudinal stiffness is significantly higher than the transverse stiffness. Figure 6.3 (Left) shows the topologies obtained for this case for both materials. On the other extreme, for the ratio of 1:1, lower compliance is achieved despite the fibre orientations being not continuous and alternatively aligned 90° to one other throughout, as seen in Figure 6.3 (Right). This results from the non-convexity of achieving a minimum with fibres aligned at ±90° given that the axial and transverse stiffness are equal.

For $E_x/E_y$ of 3.2:1 for GFRP, we see that the fibre orientations are primarily aligned along the principal stress direction in most places or along the topology features in general. However, for CFRP with $E_x/E_y$ of 3:1, the fibre orientations are not aligned too well. This explains the high compliance for ratios of 3:1 and 2:1 of $E_x/E_y$ for CFRP due to the disoriented fibres stuck in local minima. For CFRP, only $E_x/E_y$ of 6:1 and higher ratios give acceptable results for optimized fibre orientations.

From this limited data, it is seen that the ratio of transverse Young's modulus to the shear modulus has some influence on the ratio of $E_x/E_y$ that can be used for effective results with
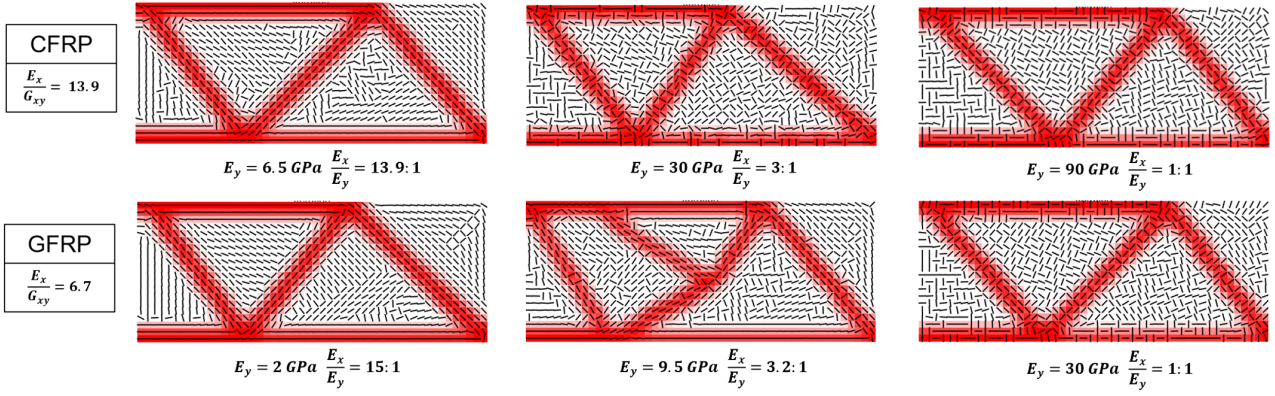
**Figure 6.3:** From (Left) to (Right), for both CFRP and GFRP, three topologies with increasing stiffness in the transverse direction are illustrated. An increasing trend in fibre misalignment is observed.

CFAO. For CFRP, $E_x/G_{xy}$ of 13.9 is almost twice as large as GFRP with $E_x/G_{xy}$ 6.7. It could be hypothesized that a minimum ratio for $E_x/E_y$, 6:1 for CFRP, 3.2:1 for CFRP, which is close to half the $E_x/G_{xy}$ value, 13.9:1 for CFRP, 6.7 for GFRP, is required to have meaningful and manufacturable results from the CFAO approach used in this work. However, the same can not be generalized for all materials and is assumed to be true for this particular material combination and material property used in this study.

Evaluating the impact of different $G_{xy}$ values for the two materials on the final topology and fibre orientations, we chose four different ratios of $E_x/G_{xy}$ for a constant $E_x/E_y$ ratio of 13.9:1 for CFRP and 3.2:1 for GFRP. By doing so, we obtain two weak shear materials, i.e. $\psi \geq 0$, one with isotropic material-like properties, i.e., $\psi = 0$ and one strong shear material with $\psi < 0$. The results of this experiment can be seen in Figure 6.5 and Table 6.5.
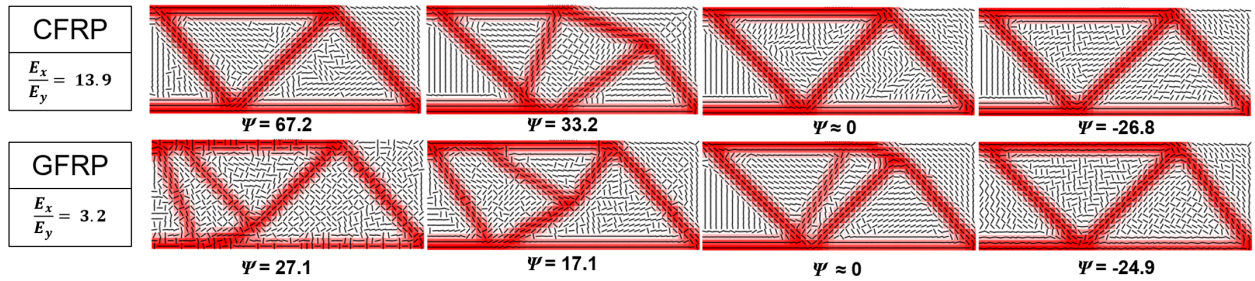


**Figure 6.4:** From (Left) to (Right), for both CFRP and GFRP, four topologies with increasing shear stiffness indicated by $\psi$ are illustrated, highlighting the importance of shear modulus properties on the fibre orientation and optimized topologies.

From Table 6.5, it can be seen that as the material becomes shear strong, the $E_x/G_{xy}$ ratio comes closer to 1:1, and the compliance reduces until it reaches a minimum for the lowest ratio of 3:1 and 2:1 for CFRP and GFRP respectively in this case. The topologies obtained for these ratios look similar to those with $E_x/E_y = 1:1$ and every isotropic material topology for a half-MBB beam in literature. This can also be seen in Figure 6.4.

For shear weak materials that have $E_x/G_{xy}$ greater than twice the $E_x/E_y$ ratio, in this case 15:1 for GFRP, the $\pm 90°$ fibre misalignment can be seen again. This limit to the shear stiffness ratio of a material required for the current implementation of CFAO with in-optimization filtering, in relation to its $E_x/E_y$ stiffness ratio, is again observed. Hence, if we were to calculate the shear stiffness values for the topologies from previous parametric studies of varying $E_x/E_y$

**Table 6.5:** Values for averaged compliance and iterations and the standard deviations for MM-FATO using the five MMA empirical parameter combinations 1-5. Three different instances of the random initial field for fibre orientations were used for averaging per trial 6-10, corresponding to the parameter combinations 1-5.

| Material | $G_{xy}$ (GPa) | $E_x : G_{xy}$ (GPa) | $\psi$ | $f(x)$ (N.m) | Material | $G_{xy}$ (GPa) | $E_x : G_{xy}$ (GPa) | $\psi$ | $f(x)$ (N.m) |
|---|---|---|---|---|---|---|---|---|---|
| **CFRP** | 6.5 | 13.9:1 | 67.2 | **5.7** | **GFRP** | 2 | 15:1 | 27.1 | 35.4 |
| | 15 | 6:1 | 33.2 | 7.3 | | 4.5 | 5.7:1 | 17.1 | 25.0 |
| | 23.3 | 3.9 | 0 | 5.6 | | 8.8 | 3.4:1 | 0 | 21.1 |
| | 30 | 3:1 | -26.8 | 5.6 | | 15 | 2:1 | -24.9 | 16.7 |

*$E_x : E_y = 13.9{:}1$ for CFRP and $E_x : E_y = 3.2{:}1$ for GFRP, and $f(x)$ or compliance results are reported for unfiltered fibre angles, i.e., before post-processing.*

ratios for $E_x/E_y = 3{:}1$ for CFRP, we have $\psi = 76.7$, and for ratios of 1:1 for GFRP we have a $\psi = 26.3$. Again, a low shear stiffness, but this one could be said to result from the extremely low $Ex/E_y$ ratio without a correspondingly high shear modulus.

The issue of fibre-misalignment with lower $G_{xy}$ values was also observed for multi-material structures optimized using MM-FATO. For brevity, the detailed results are not discussed here. Further discussion of this CFAO issue and its implication on multiple materials with non-convexity corresponding to extremely shear weak materials is done later in Chapter 7. This is, however, considered a limitation of the framework when optimizing fibre orientations.

## 6.1.3. Influence of material design volume fraction ratio

A simple study to determine the smallest and largest possible ratios of the two material design volume fractions is reported here. Figure 6.5a,b and c show the obtained topology after post-processing for three different design volume fraction ratios: 0.25:0.05, 0.005:0.295 and 0.299:0.001, respectively. Only the moderately low design volume fractions of 0.25:0.05 and 0.005:0.295 give an acceptable topology at the end of optimization. In the case of 0.005:0.295, acceptable results are obtained, as the minimum design volume fraction mandated for the stiffer material 1, CFRP, rightly optimizes the same at close to the region of load application to minimise compliance.
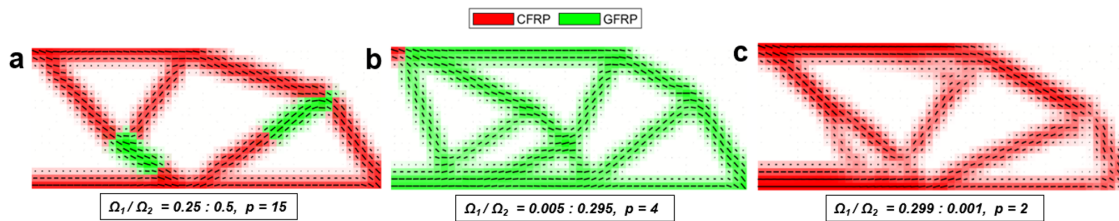


**Figure 6.5:** An evaluation for the obtained topologies with varying ratios of design volume fractions of material 1 and material 2, in this case, CFRP and GFRP from Table 5.1, shows (a) well-defined results for $\Omega_1 : \Omega_2 = 0.25{:}0.05$, (b) results for $\Omega_1 : \Omega_2 = 0.005{:}0.295$, with somewhat well-defined topology, and (c) results for $\Omega_1 : \Omega_2 = 0.299{:}0.001$, with an ill-defined topology.

As observed, extreme design volume fraction ratios of 0.299:0.001 and 0.005:0.295 for the two materials show premature convergence. Such a behaviour can be attributed to the DMO convergence criterion ($h_{95} = 1$) being met earlier at lower penalization values, i.e., $p <= 4$. This leaves final designs with many intermediate densities or grey elements. Hence, for meaningful optimization results with the MM-FATO framework, a minimum design volume fraction of 0.05 or similar for any material being considered is recommended.

This behaviour for stopping criteria is in line with the material interpolation scheme, which is specifically targeted to optimize for multiple materials. However, the convergence criteria must be modified to maintain the framework's applicability and robustness. This can be achieved as follows. Once we ensure that $h_{95} = 1$ is adhered to, we must also ensure that the convergence criterion for discreteness $D_g$ (CC3) or the maximum penalty is met, whichever comes earlier. This is different than either CC2 or CC3 being met, which is currently being done. This is, however, not implemented for results reported in this work.

### 6.1.4. Convergence Study

Convergence Characteristics

A general evolution of the topology, objective values and $h_{95}$ through different penalty steps and iterations can be visualized in Figure 6.6, where a random orientation field is used as an initial guess with $p_{max} = 6$. As seen in Figure 6.6, with increasing penalization, $h_{95}$ or DMO convergence keeps increasing till it reaches a very high value of 0.997. The compliance values are seen to reduce monotonously in a stepped manner. The steep drop observed at $p = 6$ can be attributed to the rapid redistribution of the intermediate features from the previous $p = 5$ step. Lastly, while a higher final objective than the initial design is observed, the initial guess, unlike the final result, is not manufacturable.
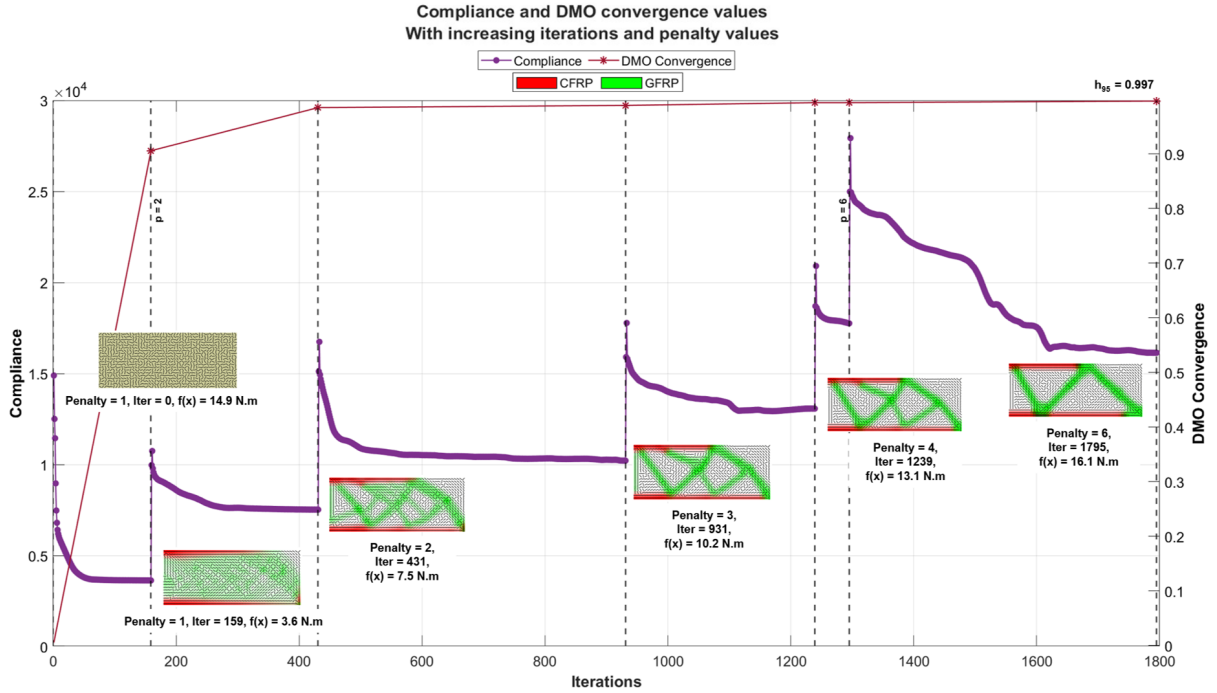


**Figure 6.6:** An illustration showing the evolution of topology, compliance and DMO converged elements, from the initial guess at iteration 0, through every $\Delta p = 1$ change, until the optimization reaches $p_{max} = 6$.

Comparing this to a single penalty step approach in Figure 6.7a and b, the final value is somewhat in the same range, i.e. 14.6 N.m vs 16.1 N.m, but the topologies obtained vary significantly. However, as seen in Figure 6.7a, the fixed penalization approach also displays an overall monotonous reduction in compliance like in penalty continuation but with fewer iterations. A minimum penalty value of five is chosen for a single penalty step, as better discreteness and quality of post-thresholding designs are achieved for a penalty of five and greater. A detailed assessment with fixed penalty values ranging from three to five and their post-processed and post-thresholding results can be referred to in Appendix C.
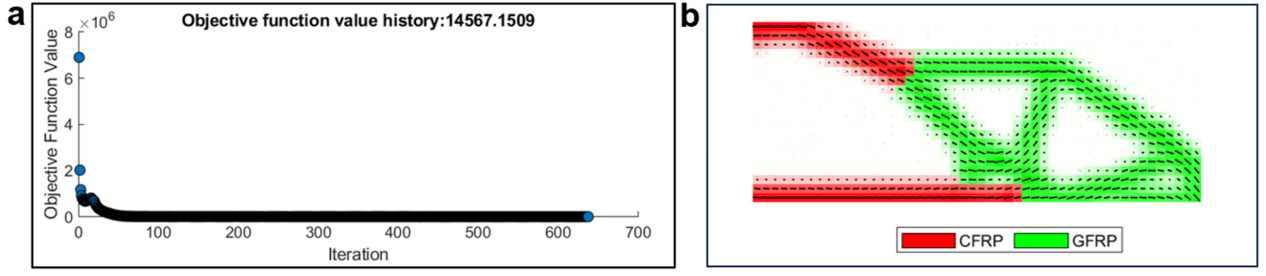
**Figure 6.7:** (a) A typical convergence curve plotted for compliance or objective function vs the number of iterations, and (b) a typical CFRP-CFRP multi-material fibre angle optimized topology, obtained with a fixed penalty factor of $p = 5$

## Penalty Step Size

Until this point, the results reported were generated using $\Delta p = 1$. To see the effect of higher or lower step size on the developed framework, a lower penalty step of 0.3 was experimented with.

Table 6.6 documents three trials each for $\Delta p = 0.3$ and 1, using the MMA parameter combination five, and with $r_{min} = 2$. All trials are carried out with a maximum penalty $p_{max}$ of 15 to ensure the DMO convergence $h_{95}$ value reaches one. From the results of this table, it is evident that a smaller penalty step size of 0.3 leads to better-optimized results overall.

**Table 6.6:** Results of three trials each for two different penalty step sizes of 0.3 and 1 values are reported, which includes the compliance before post-processing, discreteness $D_g$, DMO convergence $h_{95}$ and the maximum penalty reached for all the cases.

| $\Delta p$ | Trial | $f(x)$ (N.m) | Iterations | $h_{95}$ | $D_g$ (%) | Maximum $p$ |
|------------|-------|--------------|------------|----------|-----------|-------------|
|            | 1     | 24.2         | 1917       | 1.0      | 64.2      | 9           |
| 1          | 2     | 35.6         | 1743       | 1.0      | 59.1      | 9           |
|            | 3     | 38.2         | 1583       | 1.0      | 62.0      | 11          |
|            | 1     | 74.7         | 2741       | 1.0      | 60.7      | 13          |
| 0.3        | 2     | 18.3         | 3400       | 1.0      | 62.3      | 7.3         |
|            | 3     | 21.5         | 3133       | 1.0      | 62.8      | 8.5         |

As observed from the results, using a step size of 0.3, we can achieve $h_{95} = 1$ at lower maximum penalty values but at the cost of a higher number of total iterations. On the other hand, $\Delta p = 1$ has a higher chance of overestimating compliance and taking more penalty updates to reach $h_{95} = 1$. This overall higher compliance or a worse local minimum for the bigger step size of $\Delta p = 1$ could directly result from the quicker non-convexification of optimization problems that arise from penalization. However, the compliance for trial 1 with $\Delta p = 0.3$ is also significantly higher. Based on the obtained topology, this discrepancy could result from the optimization getting stuck in a bad local minimum. This shows that non-desirable results can be obtained even with a smaller penalty step size when a random initial guess is used without fibre angle filtering.

For practical purposes, though, the reason for any value significantly above 30 N.m obtained for the given initial conditions and penalty step size can be attributed to quick jumps in penalty factor as the optimization gets closer to meeting $h_{95} = 1$. This occurs due to the soft convergence being met at those steps quickly without any further significant improvement in the topology. This occurrence for $\Delta p = 1$ at higher penalty values can be visualised from Figure 6.8.
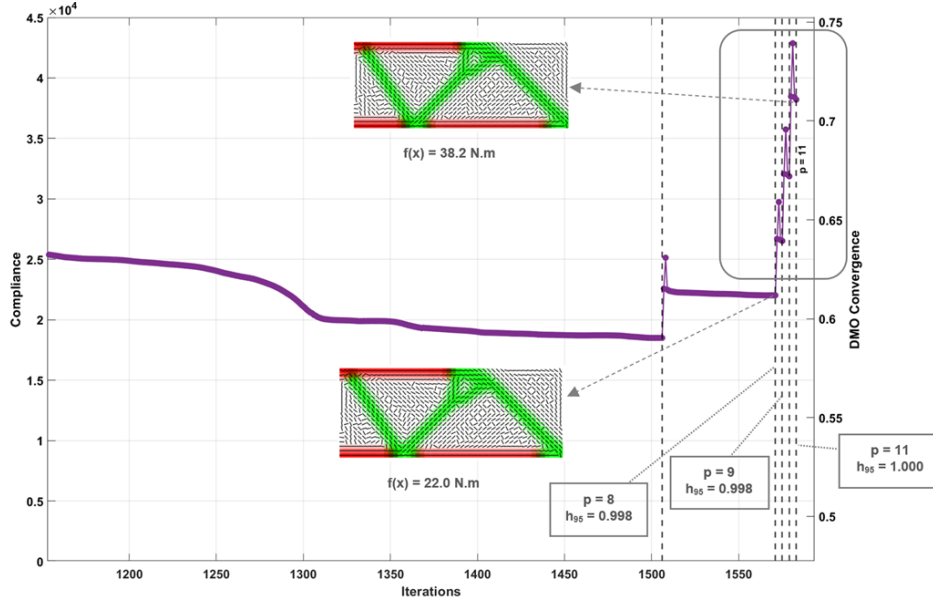
**Figure 6.8:** An illustration of sudden jumps in penalty values causing a significant increase in the compliance values without significant improvement in discreteness or DMO convergence values.

Through a crude analysis of the values in Table 6.6 and Figure 6.8, it is fair to assume that in most of the above cases, penalty steps higher than 9-10 do not improve the discreteness $D_g$ values significantly, and the intermediate DMO convergence $h_{95}$ do not change significantly for the penalty steps showing quick convergence. While effective in making $h_{95}$ reach one, the higher penalization does not change the topology or discreteness. Given that the discreteness is not as high for these results, increasing penalization values means that many intermediate densities are raised to higher powers, leading to compliance being calculated, which is quite high but not completely representative of the actual stiffness of the structure. As a result, the compliance obtained for higher penalization values should not be used directly for comparison. Based on this analysis, and to avoid such unpredictability in final results, the final compliance is calculated using p = 1 to have a fair comparison of results from now on.
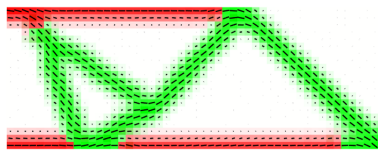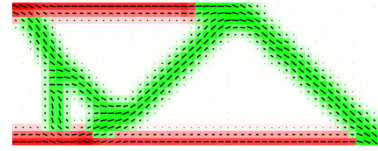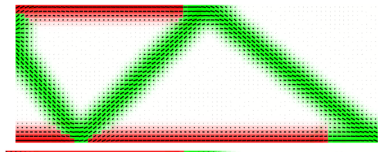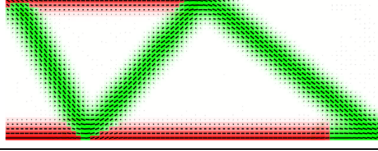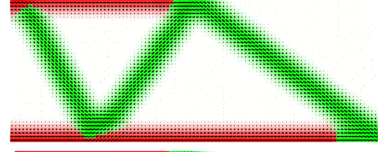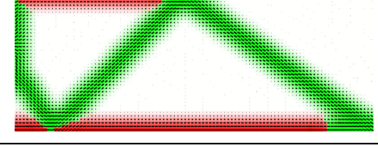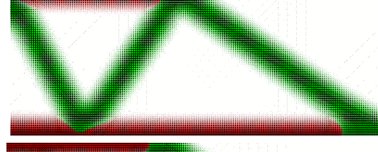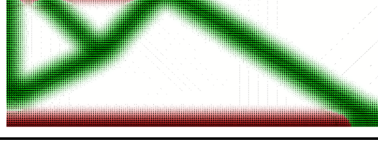
### 6.1.5. Mesh Independence Study

This study aims to see if mesh-independent results can be achieved for MM-FATO using only a density filter. Results for this study are obtained by optimizing a two-material system with CFRP and GFRP from Table 5.1 for four different mesh sizes, $50 \times 20$, $80 \times 32$, $100 \times 40$, and $200 \times 80$. This is done for a constant domain size of 50 mm $\times$ 20 mm for the half-MBB-beam load case. The four mesh sizes are filtered using $r_{min} = 2,3.2,4$ and 8 elements, respectively, resembling a 2 $mm$ filter radius with reducing element size and a $p_{max}$ of 15. The optimization results for the four meshes evaluated for two different penalty step size values are reported in Table 6.7.

As observed from the results in Table 6.7, mesh independence is not achieved for the framework when random orientations are used as initial guesses and only the density filter is used as the regularization scheme. This is irrespective of the penalty step size used. Since different random guesses are used for each trial in Table 6.7, it is possible that different local minimums are achieved. This difference in obtained topologies is further amplified by mesh refinement, which reduces the non-convexity arising from the discretization of the design domain [52].

On further investigation, another trend was observed from the convergence curves. With increasing mesh refinement, the soft-convergence condition of CC1 was not met at each penalty step update. The optimization for each penalty value terminated only due to the hard-stopping criteria, i.e. when the maximum of 500 iterations per penalty step was reached. This implies the need for more iterations per penalty step. However, if this were addressed directly by modifying the maximum iterations, the user would be required to keep increasing the maximum iterations to even higher values with mesh refinement. This would imply further slowing the convergence, limiting the framework's computational efficiency.

**Table 6.7:** Mesh-independence study for four different mesh sizes of 50x20, 80x32, 100x40 and 200x80 at two different penalty step sizes of 0.3 and 1, illustrating the obtained topology and the respective compliance obtained

| Mesh Size | Compliance (N.m)[1] | Iterations | $\Delta$p | Final Topology |
|---|---|---|---|---|
| $50 \times 20$ | 5.3 | 1602 | 1 | |
| | 5.0 | 3171 | 0.3 | |
| $80 \times 32$ | 8.1 | 4284 | 1 | |
| | 6.0 | 7815 | 0.3 | |
| $100 \times 40$ | 5.3 | 4626 | 1 | |
| | 8.9 | 10179 | 0.3 | |
| $200 \times 80$ | 6.8 | 5587 | 1 | |
| | 6.7 | 11453 | 0.3 | |



CFRP    GFRP

[1]Compliance reported with p = 1 generalization, is for compliance before post-processing step.

It is clear from the topologies shown in Table 6.7 that the converged results obtained with a mesh size of $50 \times 20$ exhibit additional truss-like features when compared to the achievable topology with increased mesh refinement. This suggests that the given design space cannot be effectively optimized with such a coarse mesh size. As a result, despite not achieving mesh-independent designs, the minimum mesh size for evaluating MM-FATO as we advance is increased to $80 \times 32$. This is done by using an element size $elSize$ of 0.625 mm. This finer mesh size could potentially give better results without a significantly higher computational cost, which would otherwise occur for more finer meshes like $100 \times 40$ or $200 \times 80$.

This study shows that using only density filtering as a regularization scheme is not ideal or enough for the current MM-FATO framework. It does not address mesh dependency. However, the same was sufficient for a simple DMO exercise in some other studies [59]. This demonstrates the persistent issue of obtaining different local minima when CFAO is coupled with DMO for MM-FATO without sufficient regularization schemes. As a result, an alternative regularization scheme might be necessary to achieve mesh-independent results for the current definition of the MM-FATO framework.

# 6.2. Influence of regularization and discreteness schemes

In this section, we evaluate the impact of alternative morphology-based filtering schemes and discreteness approach discussed in Chapter 4 on achieving a more robust MM-FATO framework that provides discrete designs.

## 6.2.1. Influence of using a combination of density and sensitivity filter

So far, all the evaluated results have only used a density filter as the regularization scheme. Given the computational benefits of a density-plus-sensitivity filter seen earlier in Section 4.1.3, in this section, the impact of the same on the current framework is evaluated to determine its effectiveness.

**Table 6.8:** Material properties calculated for 40% flax and carbon fibres in epoxy

| Material | $E_x$ $(MPa)$ | $E_y$ $(MPa)$ | $\nu_{xy}$ | $\nu_{yx}$ | $G_{xy}$ $(MPa)$ | $\rho$ $(Kg/m^3)$ |
|---|---|---|---|---|---|---|
| Epoxy & 0.4 $V_f$ of Flax | 22846 | 3899 | 0.38 | 0.06 | 2997 | 2998 |
| Epoxy & 0.4 $V_f$ of LM Carbon | 98446 | 3990 | 0.28 | 0.01 | 3752 | 3753 |

A mesh independence study with the same mesh sizes used in the previous section, Section 6.1.5, is conducted for this new regularization scheme. Here, we primarily compare the changes to topology as mesh size is refined. A random orientation field is used as the initial guess, with 40 % flax fibres in epoxy and 40 % Low Modulus (LM) carbon fibres in epoxy as alternate material choices. Properties for both materials are tabulated in Table 6.8. The results of this study are shown in Figure 6.9.

As observed, compared to using only a density filter in the previous section, the topological changes with increased mesh refinement vary less in this case. This is true for mesh sizes of $80 \times 32$ and $100 \times 40$ with a small difference in mesh size. Meanwhile, mesh dependency persists when superfine meshes like 200 x 80 are used. Such a deviation can again be attributed to the absence of fibre angle filtering during optimization. This means that the non-convexity of the objective function arising primarily from the orientation design variable is not sufficiently
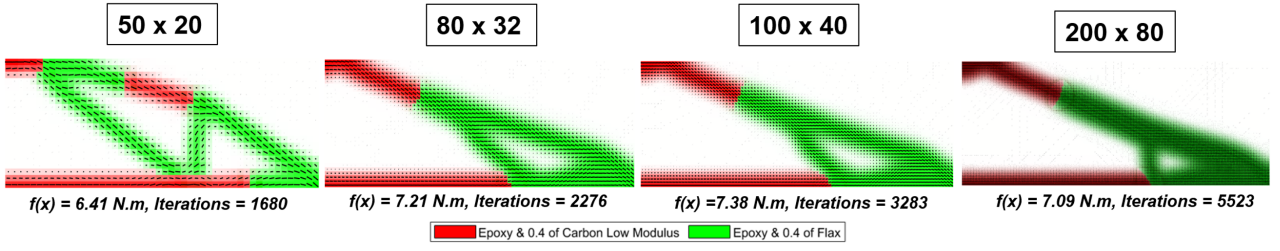
**Figure 6.9:** Largely similar topology and compliance obtained for three of four different mesh sizes of 50 x 20, 80 x 32, 100 x 40 and 200 x 80 when using a density plus density filter. A mesh size of 80 x 32 is the minimum required to obtain somewhat mesh-independent results.

addressed. As a result, when different random orientations are chosen each time, the final topologies vary to some extent, regardless of the filtering scheme applied for the material density design variables. Nonetheless, Figure 6.9 shows that the coarser mesh size of $50 \times 20$ is too coarse for this optimization problem. It deviates the most from the overall topologies obtained for other refined meshes. However, the $80 \times 32$ mesh can be used as a better option to evaluate the results further despite not achieving complete mesh independence.

To compare the two approaches further, we evaluate the influence of different filter radii on the obtained topology and compliance for the density filter and density plus sensitivity filter combination. The objective is to see the minimum feature size control variation of both approaches with different filter radii. This study uses three filter radii of 1.5 mm, 2 mm and 3 mm. The filter radii values are adjusted to the mesh size of 0.625 mm per element, resulting in values of 2.4, 3.2 and 4.8, respectively. A random angle field is used as an initial guess, and the optimization is carried out using a penalty continuation approach, where $p_{max} = 15$ and $\Delta p = 1$.
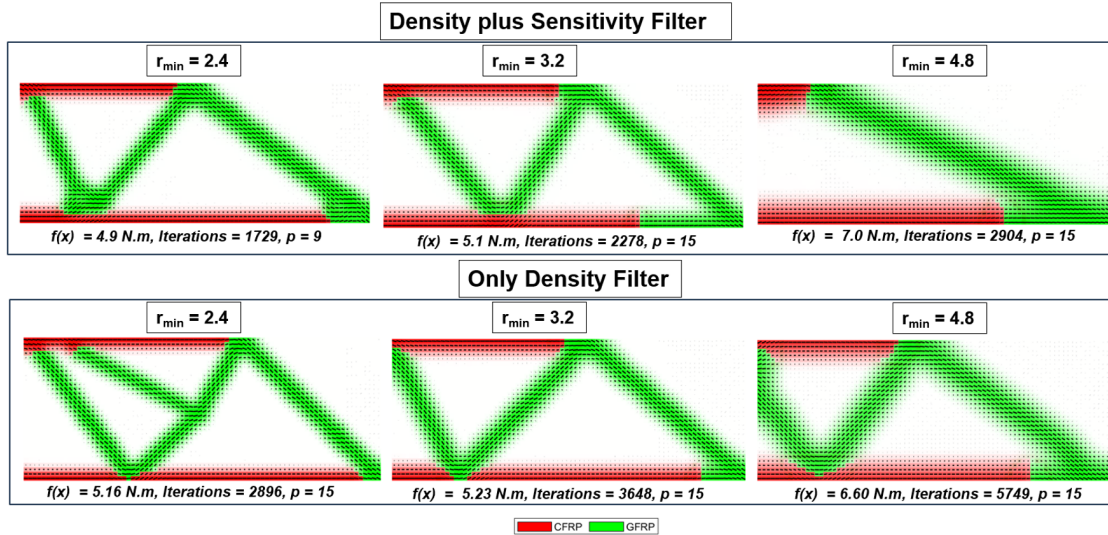


**Figure 6.10:** Minimum feature size control achieved using density plus sensitivity filter and density filter for three filter radii of 2.4, 3.2 and 4.8 mm. For the filter radii of 2.4 and 3.2, the density plus sensitivity filter results in optimized topologies with lower or similar compliance. It also takes almost half the number of iterations to obtain these topologies compared to the results using only a density filter.

Figure 6.10 shows that we can achieve the desired minimum feature size when using corresponding filter radii. This is observed for both the density filter and density plus sensitivity filter combination. However, it can be seen that the topologies and compliance obtained using a density plus sensitivity filter are better overall than when only a density filter is used. Lastly,

as expected, the number of iterations taken to convergence for three cases for the density plus sensitivity filter case is substantially less than those required for optimization with only a density filter.

Previous sections found that using only a density filter with a random angle field as an initial guess led to different outcomes for each new trial. Since this is a different regularization scheme, the impact of the density plus sensitivity filter on topologies on the repeatability of results over multiple trials using various random orientations must also be evaluated. Hence, a comparative study is conducted to assess the influence of each regularization scheme on obtaining reproducible topologies with different starting angles. The results of this evaluation are presented in Figure 6.11, where a fixed penalty factor of $p = 6$ and a density filter radius of $r_{min} = 4.8$ were used.
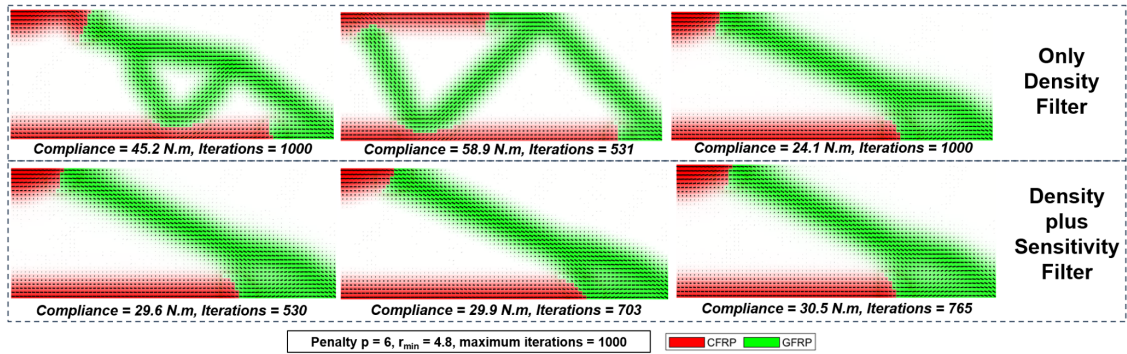


**Figure 6.11:** Comparing the results obtained for three trials with density filter and density plus sensitivity filter when random initial guesses are used for a fixed penalty step of $p = 6$ and filter radius of 4.8 mm. The density plus sensitivity filter gives more repeatable results with different random initial guesses. Whereas using only a density filter gives a different topology every time.

It is evident from Figure 6.11 that the use of density plus sensitivity filter gives more repeatable topologies results even with a random orientation field as an initial guess. This was impossible with only a density filter, even when penalty continuation was used. This is significant in addressing the issue of non-repeatable topology with random initial orientations. This combination filtering scheme thus reduces the number of trials and, subsequently, the computation time required to assess the quality of the local minima obtained when using random orientations as an initial guess. However, using only a density filter can result in lower compliance for certain initial guesses, as observed in Figure 6.11 (Right) compared to using a density plus sensitivity filter. This is despite similar-looking topologies for both cases. As a result, some questions about such a filtering scheme's efficacy in obtaining better solutions still remain.

From this evaluation of the regularization scheme, it can be concluded that for a multi-material topology optimization problem addressed using the DMO2 interpolation scheme, the use of a density plus sensitivity filter is imperative to achieve better, if not completely, mesh-independent results. In Sanders et al. [42], it was not the best solution when only material density optimization was done. However, this filter combination is the better option when fibre orientation is optimized as a separate variable and with a random orientation field as an initial guess.

## 6.2.2. Influence of discreteness improvement approaches

Both penalty steps of 1 and 0.3 in Section 6.1.4 gave similar results in terms of discreteness. However, for AM fabrication, the results are not discrete enough. The proposed density filter reduction scheme or "Approach 1" post-convergence can be applied to improve the $D_g$ values achieved. Alternatively, a projection-based post-processing scheme using the Equation 4.2 in Section 4.1.3, "Approach 2" can also be implemented. Comparative results for these two approaches, when applied to the topology obtained for $r_{min} = 3.2$ in Section 6.2, Figure 6.10, can be seen in Figure 6.12.

From Figure 6.12, "Approach 1" to improve discreteness is seen to give more discrete results even before thresholding. This is expected since the filtering effect is reduced drastically, and filtering is the reason for intermediate densities in the first place. However, a disadvantage of this approach is the jagged topology obtained. This could be reduced by further increasing the penalization step when reducing the filter radius at each step. Nonetheless, the number of iterations taken is significantly higher for "Approach 1", with approximately 1000 extra iterations. This is not the best outcome for computational efficiency.
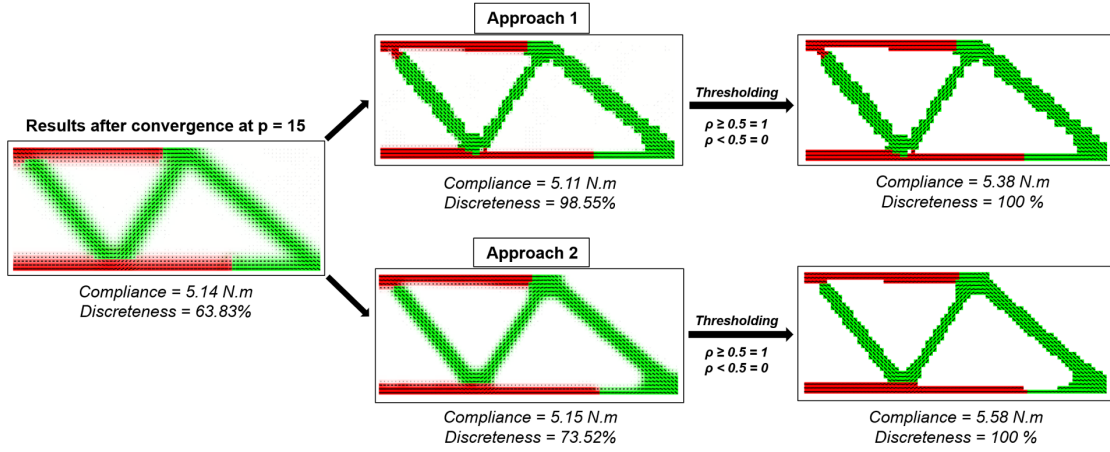


**Figure 6.12:** The two discreteness improvement approaches, "Approach 1" with gradual filter reduction to $r_{min} = 1$ post-convergence at the end of p = 15, and "Approach 2" with a Heaviside projection scheme applied till $\beta$ reaches 16, starting from 1. The discreteness and the compliance obtained with "Approach 1" is better overall. However, a jagged topology is achieved. A topology with better-defined edges is achieved for "Approach 2". Post thresholding, however, a discreteness of 100% can be achieved for both approaches without a significant increase in compliance.

On the other hand, "Approach 2" gives slightly less discrete designs for an additional 250 iterations. Still, better-defined contours for the topology are obtained for this approach compared to "Approach 1", which is suitable for manufacturing without any further excessive post-processing. Some other disadvantages of "Approach 2" include the loss of minimum feature size after thresholding with a limit of 0.5 in some regions of the structure, as seen in Figure 6.12. The thresholding also causes the design volume fraction of the materials to drop to 0.099 and 0.179 from 0.1 and 0.2, respectively, for GFRP and CGRP.

A less aggressive value for thresholding of 0.3 for "Approach 2" was seen to improve the feature size but increases $\Omega_1$ to 0.127 and $\Omega_2$ to 0.242. This change in volume fraction is not desirable, given that it directly impacts the final mass of the structure. A change in mass alters the expected $CO_2$ footprint of the multi-material structure significantly. Nonetheless, "Approach 2" is a better alternative for current work since it potentially gives more manufacturable designs. However, further investigation is necessary to assess the actual ease of manufacturing for "Approach 2".

## 6.3. Robustness of MM-FATO to alternate design domains

The previous assessment was used to determine the better filtering and post-optimization discreteness improvement schemes. This assessment modified the MM-FATO framework to include a density plus sensitivity filter and the Heaviside projection method, resulting in a more robust and functional MM-FATO framework.

Two alternate load cases are considered to further assess the robustness of this modified framework. One is an L-shaped beam, and the other is a cantilever beam with a pressure load on its top edge. Both load cases are optimized for the baseline setup materials, CFRP and GFRP, using the penalty continuation approach, where $\Delta p = 1$ and $p_{max} = 15$. The compliance and topologies obtained for both the load cases can be seen in Figure 6.13a and b, respectively. Optimizing the L-shape and cantilever beam load cases for $\Omega_f = 0.3$ using MM-FATO gives a compliance of 15.89 N.m and 9.465 N.m, respectively. Both the compliance values are reported at $p = 1$.
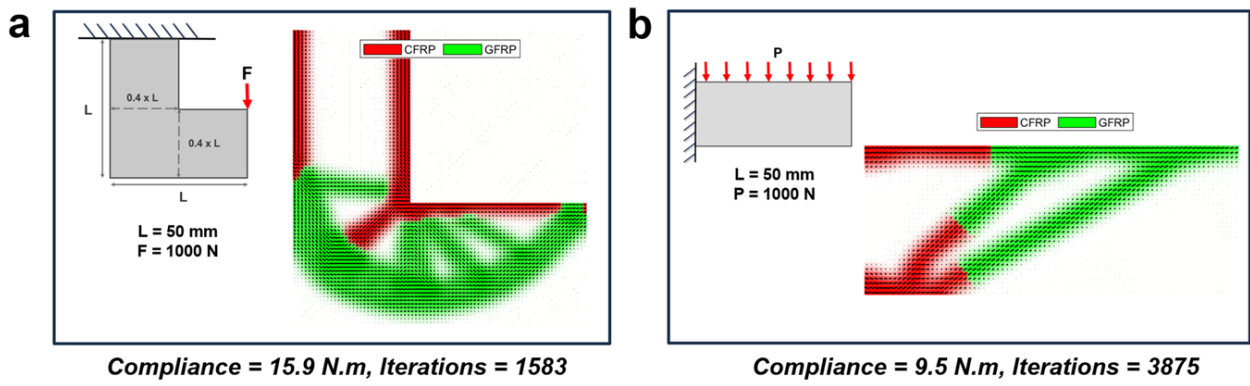


**Figure 6.13:** For an L-shape beam with dimension 50 mm x 50 mm and a point load at the free tip in (a), a well-defined multi-material topology with continuous and manufacturable fibre paths is obtained except at the point of load application. Meanwhile, a well-defined multi-material topology and continuous fibre orientations are also obtained for a cantilever beam with a pressure load on the top edge in (b).

As seen in Figure 6.13a and b, well-defined topologies are obtained for both the alternate design space and load cases. This establishes the general applicability of the framework to design domains with passive regions and alternate loading conditions. Furthermore, in Figure 6.13a and b, the resultant topologies show placement or stiffer material in locations with highly loaded regions in tension and compression as expected. However, an island of CFRP material at the region of load application is also observed in Figure 6.13a. This anomaly can be attributed to the finite element definition, where the point load F of 1000 N acts solely on one node in the finite element mesh.

The results for the L-shape beam in Figure 6.13a also highlight another limitation of the framework to converge prematurely. It was observed that the DMO convergence or $h_{95}$ is met sooner at p = 4. This premature convergence caused by the convergence criteria definition can lead to less-developed topologies. Such an effect is undesirable and unsuited for manufacturable designs. An alternative would be to modify the convergence criteria to always run until the CC3 or discreteness condition is met and apply point loads to a group of nodes in proximity to the actual point of load application.

# 6.4. Framework performance assessment

Although computational efficiency is maximized despite the limitations of DMO formulation and a lack of in-optimization fibre orientation filtering, it has not been quantitatively evaluated so far. Hence, this, along with the objective values and $CO_2$ footprint achievable with MM-FATO, is analyzed in this section through comparative studies. However, given the MM-FATO framework implementation limitations, only a simple computational efficacy study is conducted without bench-marking the framework with other frameworks in the literature.

## 6.4.1. Evaluating Compliance Performance for MM-FATO

To assess the MM-FATO framework's performance regarding the attainable computational efficiency and objective values, we compare the results obtained with MM-FATO to those achieved with the SM-FATO framework of Almeida [6] and an equivalent isotropic multi-material topology optimization result. All the results use the same optimization algorithm, MMA, to enable the comparison of iterations as a metric for computational costs. Furthermore, to obtain a fair comparison, the SM-FATO framework without in-filter optimization is used.

Figure 6.14a,b and c show the results of topologies obtained using SM-FATO for CFRP and GFRP, MMTO framework with isotropic equivalent of CFRP and GFRP materials, and the MM-FATO framework developed in this work for the same set of materials respectively. For figure 6.14b, the isotropic equivalent properties are evaluated using the MM-FATO framework minus the fibre orientation optimization. To mimic the isotropy as randomly oriented metal grains on the micro-scale, results are derived with a finer mesh of $200 \times 80$.



**a** Anisotropic Single Material TO (SM-FATO)

CFRP  GFRP

*Compliance = 4.0 N.m , Iterations = 4203*   *Compliance= 7.6 N.m , Iterations = 1417*

**b** Isotropic Multi-Material TO* (MMTO)   **c** Anisotropic Multi-Material TO (MM-FATO)

CFRP  GFRP   CFRP  GFRP

*Compliance = 12.9 N.m, Iterations = 4495*   *Compliance = 5.4 N.m , Iterations = 3237*

*The isotropic case is still a result from the MM-FATO framework minus the fibre orientation optimization. Results are obtained with a finer mesh of 200 x 80 that has random orientations, mimicking isotropy on a micro scale.

**Figure 6.14:** (a) Compliance and topology for CFRP and GFRP structures obtained using the SM-FATO approach, (b) A higher overall compliance and topology for an equivalent isotropic multi-material structure with CFRP and GFRP obtained using the MM-FATO approach, but without fibre angle optimization and a random orientation field mimicking metals at micro-scale, (c) Compliance and topology obtained for CFRP and GFRP simultaneously optimized using MM-FATO, with lower compliance compared to (b) and intermediate to that of CFRP and CFRP structures in (a).

Comparing Figure 6.14a and c, we can see that the compliance obtained with MM-FATO of CFRP and GFRP is in between that of SM-FATO for the individual materials and only 35.7% greater than the stiffest material of the two. This comparison is done for the same $\Omega_f = 0.3$

for SM-FATO and MM-FATO, without additional constraints. As seen from the iterations, the computational efficacy for MM-FATO is not worse and is comparable to the SM-FATO approach. This is despite both approaches considering the same penalty continuation approach with $\Delta p = 1$ and equivalent convergence criteria of obtaining discreteness of 70% or $p_{max}$ whichever comes first.

To reiterate the benefit of optimizing fibre orientations compared to using equivalent isotropic properties for topology optimization of composites, the compliance for the Isotropic MMTO and anisotropic MMTO or MM-FATO can be compared in Figure 6.14b and c. A 58.3 % improvement in compliance is achieved by using anisotropic materials and fibre orientation optimization MM-FATO compared to MMTO with equivalent isotropic materials. The computational efficacy, however, is not comparable in this case, given the different mesh sizes used to generate the two results.

## 6.4.2. Evaluating $CO_2$ Footprint Performance for MM-FATO

One of the main goals of this project was to evaluate the enhancement of compliance and reduction of $CO_2$ footprint in a composite structure consisting of multiple materials. For this assessment, we first compare the impact of substituting different natural fibres in a CFRP composite and optimizing it using MM-FATO.

For this study, results are generated for three $V_f = 0.3$, 0.4 and 0.5 and for three ratios of design domain occupied by the two materials in the multi-material structure, i.e. $\Omega_1/\Omega_2 = 0.2{:}0.1$, 0.15:0.15 and 0.1:0.2. This is done in accordance to the design of experiments for $CO_2$ evaluation detailed in Section 5.3.3. Table 6.9 shows the results for composites comprising 50 % $V_f$ of four different fibres, bamboo, hemp, flax, and low-modulus (LM) carbon in PLA matrix. These combinations are further referred to by their abbreviations, BFRP, HFRP, FFRP and CFRP. Note that all the total $CO_2$ footprint values reported in this section are uniformly scaled by 6.5. This is done as a correction factor to account for a discrepancy in the LCA data reported in the two reference studies [61], [62].

**Table 6.9:** Material properties and $CO_2$ footprint of materials obtained when different fibres, both synthetic and natural with a fibre volume fraction of 0.5, are combined with PLA matrix

| Material | $E_x$ (MPa) | $E_y$ (MPa) | $\nu_{xy}$ | $\nu_{yx}$ | $G_{xy}$ (MPa) | $\rho$ (Kg/m³) | $CO_{2mat}^i$ (KgCO₂/kg) |
|---|---|---|---|---|---|---|---|
| PLA & 0.5 $V_f$ of Bamboo | 10475 | 5764 | 0.39 | 0.215 | 2912 | 980 | 3.69 |
| PLA & 0.5 $V_f$ of Flax | 28475 | 6482 | 0.37 | 0.085 | 4639 | 1365 | 2.58 |
| PLA & 0.5 $V_f$ of Hemp | 32975 | 6539 | 0.33 | 0.066 | 4916 | 1375 | 3.82 |
| PLA & 0.5 $V_f$ of LM-CF | 122975 | 6803 | 0.25 | 0.014 | 6283 | 1540 | 25.86 |

When optimizing a multi-material composite structure comprising of CFRP and one of the NFRPCs, namely, BFRP, FFRP or HFRP, resultant structures with much lower $CO_2$ footprint can be achieved at the cost of some stiffness, as seen in Figure 6.15. This reduction in carbon footprint increases as the $\frac{E_x}{\rho}$ ratio of the natural fibre increases or the absolute value of $\rho$ decreases. Bamboo fibre has the highest $\frac{E_x}{\rho}$ ratio and the lowest $\rho$ amongst all fibres considered. Hence, the lowest carbon footprint values are observed for all CFRP-BFRP cases with different fibre volume fractions and the CFRP to BFRP ratio in the optimized structure. As also observed, since HFRP and FFRP have similar densities, they tend to show similar results for achievable $CO_2$ footprint and compliance when combined with CFRP.
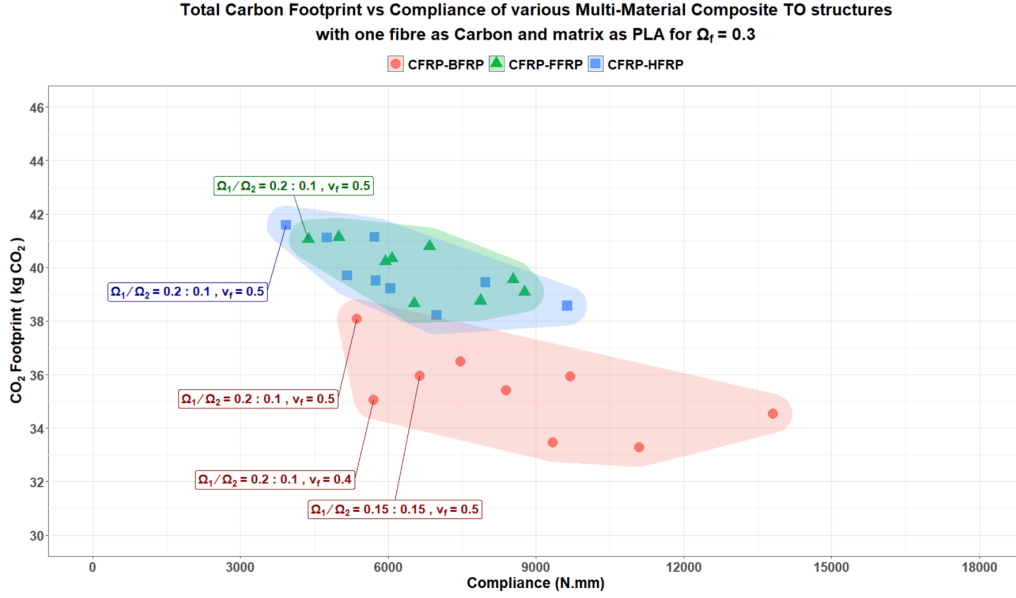
**Figure 6.15:** A plot of total $CO_2$ footprint vs compliance achieved for various multi-material structures where one material is LM carbon fibre in PLA matrix and the second is bamboo, hemp or flax fibre in PLA. Each envelope for these combinations includes results for a fixed design volume faction $\Omega_f = 0.3$ but with three different $\Omega_1/\Omega_2$ values (0.2:0.1, 0.15:0.15 and 0.1:0.2) for the two materials. These ratios are optimized for three fibre volume fractions ($V_f = 0.3$, 0.4 and 0.5), resulting in nine data points per material combination.

Next, we evaluate the performance of SM-FATO structures of BFRP, HFRP and CFRP with $V_f = 0.5$. The compliance and $CO_2$ footprint values of the optimized CFRP, BFRP, and HFRP structures for $\Omega_f = 0.3$ can be seen from Figure 6.16a and b. For MM-FATO, we can now compare how the variations in fibre volume fraction and the ratio of the volume occupied in the design domain by the two materials influence the obtained compliance and $CO_2$ footprint.

As seen in Figure 6.16a, by substituting 33.33 % of the occupied fraction for an optimized structure made up only of CFRP with BFRP, we can obtain a reduction of 16.2 % in $CO_2$ footprint and an increase of 140.4 % in compliance. With any further increase in the total fraction of BFRP occupied in the design domain to 15 % and beyond while maintaining $\Omega_f = 0.3$, a reduction of $CO_2$ footprint is observed. The rate of increase in compliance, however, is much higher than the amount of reduction in $CO_2$ footprint.

Since the density of BFRP is quite lower than that of CFRP, i.e., $\rho_{BFRP} = 980\ kg/m^3$ and $\rho_{CFRP} = 1540\ kg/m^3$, increasing its volume fraction adds less but a sufficient amount to the total mass of the structure than what reducing the volume fraction of CFRP removes from it. This leads to a slower reduction in the $CO_2$ footprint that is dictated by the structure's mass. On the other hand, a reduction in the amount of LM carbon fibres in the resultant structure, which contributes more to the stiffness amongst both the fibres in highly loaded regions, affects compliance significantly and causes a sharper drop.

Furthermore, from Figure 6.16a and b, it can be observed that a higher fibre volume fraction of 0.5 compared to 0.3 for both CFRP-HFRP and CFRP-BFRP shows a decrease in the overall compliance. This is expected with the increase in directional stiffness. However, different trends are observed for the total $CO_2$ footprint reduction. A not-so-significant increase in the $CO_2$ footprint for the CFRP-BFRP combination and a moderate increase in the $CO_2$ footprint for the CFRP-HFRP combination.
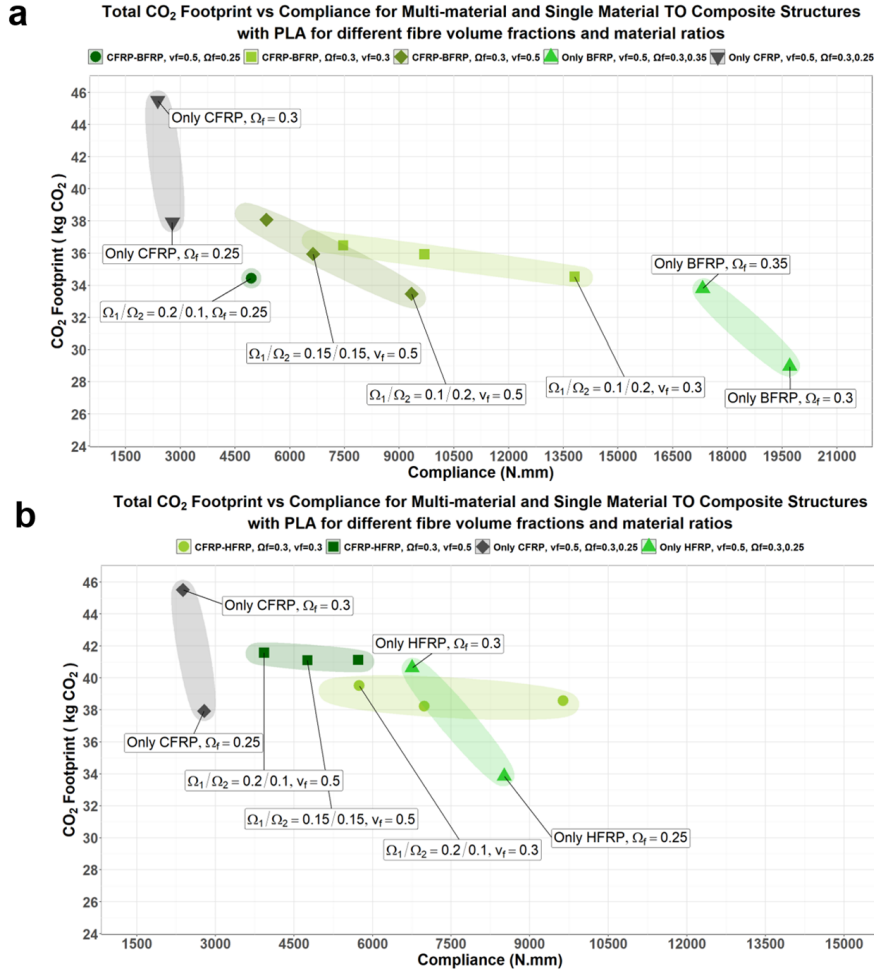
**Figure 6.16:** (a) LM carbon and bamboo fibre-reinforced PLA composite structures achieve intermediate compliance and $CO_2$ footprint to those achievable using only either of those materials. This is true for a fixed $\Omega_f = 0.3$ for both SM-FATO and MM-FATO. However, the results for the CFRP-BFRP structures are not necessarily better in terms of $CO_2$ footprint when compared to a result for a reduced $\Omega_f = 0.25$ for only the CFRP structure. (b) On the other hand, LM carbon and hemp fibre-reinforced PLA composites in the two material systems also show a similar trend for the higher $V_f$ of 0.5.

This again relates to the difference in density of the composites achieved with varying fibre volume fractions from 0.5 to 0.3. This change for low-density BFRP increases the mass while reducing it by a similar amount for CFRP. This negates any impact on mass savings when the same volume fraction of 0.15 is occupied by both materials in the design domain for $V_f = 0.5$ and $V_f = 0.3$. For HFRP, on the other hand, the density increases with an increase in the fibre volume fraction from 0.3 to 0.5 for all $\Omega_1/\Omega_2$ ratios. At the same time, the density of CFRP also increases, causing the mass to increase. This eventually leads to an increase in the overall $CO_2$ footprint of the structure.

Figure 6.16a further shows that for an occupied volume fraction reduction from $\Omega_f = 0.3$ to 0.25 in the SM-FATO CFRP structure, a substantial reduction in the $CO_2$ footprint of 16.6 % at the cost of a 24.84 % increase in compliance is observed. This is better than what was achieved with multi-material TO structure with CFRP and BFRP. This reduction in $CO_2$ footprint directly results from lower weight resulting from a lower volume fraction. However, for the given filter radius of two, any further reduction in design volume fraction does not yield any optimized structure, and 0.25 is the lowest value tried for which a result was obtained. Further increasing $\Omega_f$ from = 0.25 to 0.7 only resulted in a steady increase in $CO_2$ footprint and reduced compliance. This was accompanied by a reducing slope for each step of increase in $\Omega_f$.

Results for an CFRP-BFRP structure with a lower $\Omega_f = 0.25$ and $\Omega_1/\Omega_2 = 0.2 : 0.05$ are also plotted in Figure 6.16a. For this configuration, a 24 % reduction in $CO_2$ footprint at the cost of approximately 100 % increase in compliance compared to CFRP structure with $\Omega_f = 0.3$ is observed. On the other hand, an CFRP-HFRP structure with a higher $\Omega_f = 0.3$, and $\Omega_1/\Omega_2 = 0.2 : 0.1$ is plotted in Figure 6.16b. For this structure, it is seen that a 7.6 % reduction in $CO_2$ footprint at the cost of approximately 76 % increase in compliance can be obtained. In a real-life application, depending on the stiffness requirements for the structure, one can be a better option than the other. The reduction in $CO_2$ emissions reported here can be expected to scale with the size of the structure. Hence, even a 7.6 % saving in $CO_2$ footprint or 4 kg of $CO_2$ for a small 10 $cm^3$ part is not negligible.

However, as expected, the results generated with fixed $\Omega_f$ values are not better than a simple SM-FATO structure with an optimum design volume fraction on the Pareto front. This is the inherent limitation of what can be achieved with MMTO or multi-objective TO for such problems. Nonetheless, it allows for a better-optimized compromise between the desired properties. The obtained results for MM-FATO in this study for the same design volume fraction as the SM-FATO results can be seen to form a Pareto front of sorts in Figure 6.16a and b, which fills the gap between already existing Pareto fronts for the individual materials with varying design volume fractions. This allows designers to tap into the potential for structures that can best compromise between each material's desired properties, $CO_2$ footprint and compliance.

Hence, further creation of a database of $CO_2$ footprint and compliance for all the multi-material material combinations for various ratios of material can be used for preliminary assessment for choosing what ratio of two materials can potentially give the best compromise in $CO_2$ reduction and compliance to carry designed loads while being more eco-efficient.

### Limitation of the $CO_2$ impact study

A limitation of this evaluation is that a fixed total volume occupied in the design domain by both the materials of $\Omega_f = 0.3$ is used. As expected, this results in limited information, and more optimal solutions can be achieved by including results for arbitrarily varying volume constraints for each material. Ideally, we should have the Pareto front with $CO_2$ footprint and compliance data for all combinations of composite materials under consideration for different design volume fraction ratios. This can then be compared with the optimal Pareto front obtained for plotting results of SM-FATO structures at different design volume fractions to see if any improvement is possible. However, the same was not done owing to the high computational times and efforts, which included 4000 to 7000 major iterations per optimization with times upward of 5400 seconds on average with smaller penalty steps of $\Delta p = 0.3$. Hence, a computing cluster is recommended when creating a database with different material combinations for varying $\Omega_f$ and $\Omega_1/\Omega_2$ values.

Furthermore, with an alternative optimization routine incorporating the free selection of volume fractions of individual materials with a constraint on compliance, equal to CFRP with $V_f = 0.5$, more optimal results could be achieved [13]. However, only if the $\frac{E_x}{\rho}$ ratio of the second composite material to be used is high enough does the optimization in such a case result in the presence of both materials in the optimized structure [35]. This is true only when the co-existence of both materials in the design space is not explicitly mandated using individual volume constraints. If both materials are mandated to co-exist, the solver might result in an unsuccessful optimization attempt for a potentially over-constrained design space.

<div align="right">

# 7

</div>

<div align="right">

# Discussion

</div>

To obtain continuous fibre paths, the orthotropic material approximation for shear modulus, shown in Equation 7.1, was implemented for all the results in this work. This was done instead of the more suitable transverse isotropic material approximation for shear modulus in Equation 7.2.

$$G_{xy} = \frac{E_x E_y}{E_x + E_y + 2E_y\nu_{xy}} \tag{7.1}$$

$$G_{xy}^{matrix} = G_{xy}^{fibre} = \frac{E_x}{2(1 + \nu_{xy})}; \qquad G_{xy}^{composite} = \frac{G_{xy}^{matrix} \times G_{xy}^{fibre}}{V_f G_{xy}^{matrix} \times (1 - V_f)G_{xy}^{fibre}} \tag{7.2}$$

For topologies optimized using Equation 7.2, the issue of non-convexity in fibre angle optimization was observed to be quite high due to extremely shear weak materials. In Figure 7.1a and b, results for the same combination of flax-reinforced epoxy composite with two different shear modulus values from Table 7.1, calculated using the approaches in Equation 7.1 and 7.2 can be seen. For Figure 7.1b, it can be seen that the fibre orientation in elements with FFRP material shows a similar result to what was obtained for GFRP on reducing its shear modulus when evaluating the sensitivity of material properties in Section 6.1.2.
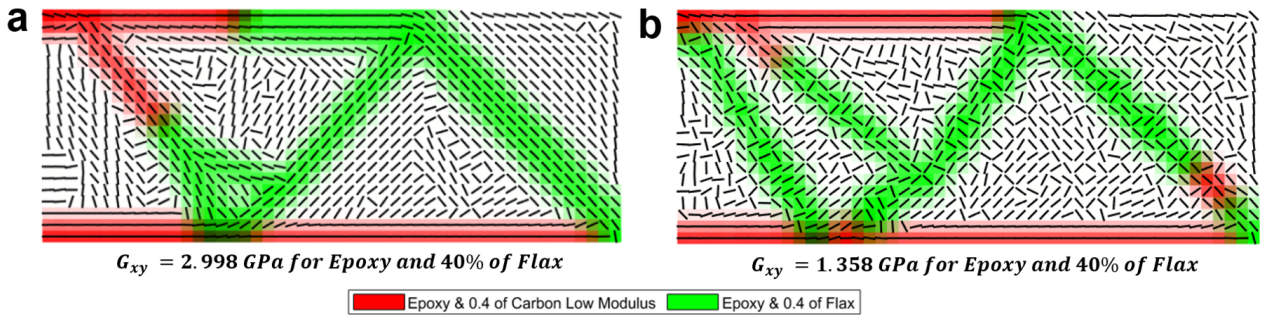


**Figure 7.1:** (a) Multi-material topology with well-aligned fibre orientations obtained by using the orthotropic definition for shear modulus $G_{xy}$ in Equation 7.1 (b) Multi-material topology with misaligned fibres, obtained with by using the transverse isotropic definition for shear modulus $G_{xy}$ in Equation 7.2

In general, fibre irregularities and fibre orientation misalignment by approximately 90°, as seen in Figure 7.1b, result from the non-convexity for the process of optimizing orthotropic materials. These elements in tension and compression regions have "multiple orthogonal local minima" for each principal direction [37]. For highly shear-weak materials especially, multiple local minima can exist for the same loading direction, as seen for the case of Epoxy and 0.4

**Table 7.1:** Shear modulus properties obtained for two combinations of matrix and fibres, flax and epoxy and low modulus carbon and epoxy with fibre volume fraction 0.4, calculated using two different approaches 1 and 2

| Material | $E_x$ (MPa) | $E_y$ (MPa) | $\nu_{xy}$ | $\nu_{yx}$ | $G^1_{xy}$ (MPa) | $G^2_{xy}$ (MPa) |
|---|---|---|---|---|---|---|
| Epoxy & 0.4 of Flax | 22846 | 3899 | 0.381 | 0.065 | 2997 | 1358 |
| Epoxy & 0.4 of LM Carbon | 98446 | 3990 | 0.281 | 0.011 | 3752 | 1421 |

Flax with $G^2_{xy} = 1358$ MPa or $FFRP^2$ also shown in Figure 7.2b. This could explain the behaviour of the design variables getting trapped in local minima for this material in Figure 7.1b when using random orientations as an initial guess.

**a**

**b**
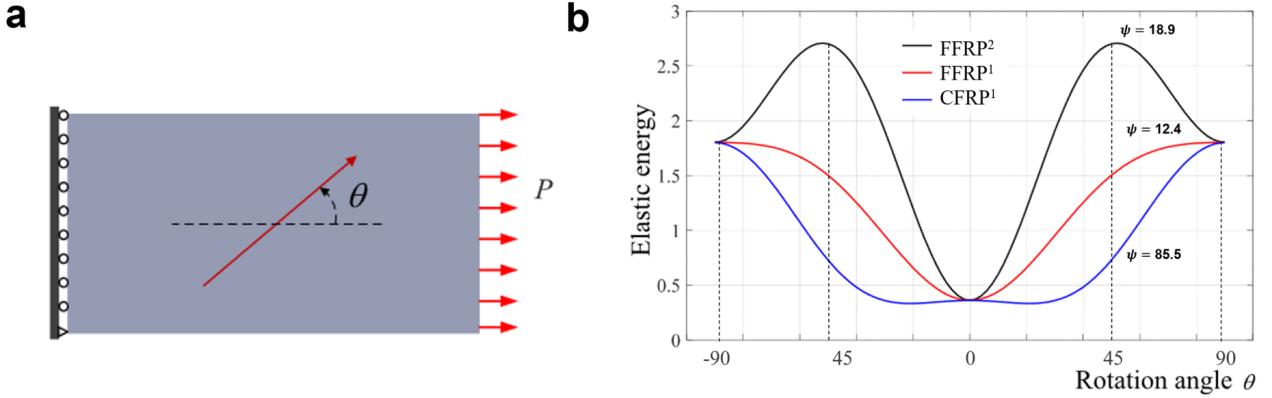


**Figure 7.2:** (a) A simple load-case to test the influence of loading direction on fibre orientations for materials with different shear stiffness, (b) plot for 3 materials obtained at various uniform orientations of fibres in the design domain and loads shown in (a). The materials include two variations of "Epoxy and 0.4 $V_f$ of Flax" composite using $G^1_{xy}$ and $G^2_{xy}$ ($FFRP^1$, $FFRP^2$), and "Epoxy and 0.4 $V_f$ of LM Carbon" using $G^1_{xy}$ ($CFRP_1$). The graph in (b) is not to scale. it is recreated and adapted directly from Qiu et al. [21] as a demonstration of a potential cause for misaligned fibre orientations.

In-optimization filtering is a promising solution to address the anomaly, as demonstrated in Schmidt et al. [37]. If in-optimization filtering is not used, a strategy similar to that described in Qiu et al. [21] can be employed to deal with the non-convexity issue in shear-weak materials. The authors used a two-sub-interval discrete-continuous parameterization (DCP) approach, which enabled them to achieve continuous fibres without encountering the issue of local minima for shear-weak materials. This was done by introducing two orthogonal angles as design variables for each element and interpolating the material properties using both values.

Nonetheless, without any fibre angle filtering scheme during optimization, feasible topologies in terms of fabrication were only achieved when considering the highly non-conservative shear modulus properties calculated using Equation 7.1. This is, however, not representative of the micro-mechanical model or the actual shear modulus of these UD composites being modelled. As a result, a more accurate micro-mechanical representation for the UD composite material properties must be used with a working implementation of fibre angle filtering to obtain reproducible objective functions using AM.

# 8
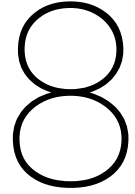
# Conclusions

In this thesis, we established the potential and limitations for a new framework that can concurrently optimize the fibre orientations of multiple composites in the same structure while producing AM manufacturable designs. This gradient-based topology optimization framework has the potential to optimize any number of orthotropic materials with complementary properties within any regular 2D design domains despite the current MATLAB implementation being limited to optimising two composite materials. The designs obtained post-optimization from this framework have the potential to generate continuous fibre paths for creating G-codes compared to previous studies in literature like that of Duan et al. [32]. Thus making it easier to 3D print these multi-material structures using the Fused Deposition Modelling technique.

A simple yet effective solution to solve the combined non-convexity from the extended design space due to the continuous fibre angle optimization (CFAO) and the DMO multi-material interpolation scheme was proposed in this work. The issue of variability in final results when optimizing using random fibre orientation as an initial guess has not been addressed well in the existing literature. However, this work established that using a density plus sensitivity filter as a regularization scheme for density design variables could significantly reduce the variance in topologies obtained with a random orientation field as an initial guess.

A rigorous sensitivity study of material properties suitable for this framework established limitations concerning the CFAO implementation in this framework for highly shear-weak materials. With the current CFAO implementation, the susceptibility of such material properties to cause the local fibre orientations to fall into local minima was deemed unavoidable. This is unless fibre orientation regularization schemes can be implemented throughout the optimization like done in Schmidt et al. [37], or a different formulation (DCP) for fibre orientation optimization that accounts for the local minima issue for shear weak materials using like done in Qiu et al. [21].

Once the study's limitations are addressed, this framework is proposed to serve as a starting point for all future 3D printing exercises for multi-material composite structures. The eco-efficiency assessment saw a successful generation of intermediate designs with a good compromise between $CO_2$ emissions and mechanical performance. As a result, such a framework is also envisioned to be used as a tool for developing an eco-design database for various material combinations. Such a database would enable users to make sustainable material choices for their parts that best meet the application requirements regarding stiffness while minimizing $CO_2$ emissions.

# 9

# Recommendations and Future Work

Based on the insights and results gathered in this study, it is evident that there are implications for future research. For instance, it is recommended to include in-optimization filtering and a more representative constitutive model for material optimization. However, since this study did not validate the designs and stiffness obtained using MM-FATO through FDM printing and testing, the primary recommendation for future work is to print the multi-material composite structures obtained in this study.

For creating more discrete and manufacturable designs without excessive post-processing, it was seen that the use of Heaviside projection plus thresholding post-optimization resulted in more discrete results than without. However, the projection parameter was limited to 16, providing insufficient discreteness without thresholding. Furthermore, HSM and thresholding together significantly modified the occupied volume fraction of the two materials in the design domain. This is not ideal and can impact the structure's total mass, which can be difficult to predict. Hence, a better projection-based discretization strategy must be integrated in future studies which is more robust, i.e., without requiring thresholding and is volume-preserving like proposed in the work of Sigmund [47], and Li and Khandelwal [63].

Furthermore, in this thesis, only two materials were studied, which limits the possible designs that can be achieved using the developed framework. Therefore, an extension to include more candidate materials must be implemented, and the $CO_2$ impact results evaluated for further changes in the design objectives. Additionally, the thin 2D structure optimized for single loads in this work should be expanded to 3D optimization for multiple load cases. This would demonstrate the framework's applicability in optimizing structures for real-life load case scenarios with multiple loads acting in three dimensions.

The current work also does not assess the stress profile of the optimized topologies or the multi-material interfaces or joints. This limits the model's capabilities to reduce stress concentrations and have a designed failure mode. Since the joints are assumed to be perfectly bonded, or simply a uniform stress transfer across the interfaces is considered, the chances of failure during testing at the joints due to stress concentrations are quite high. Hence, the same must be considered for future work by using a stress-based optimization model or stress constraints.

After reviewing the state-of-the-art, it is suggested that the optimization routine should consider the multi-material interface through the use of compression-tension stress constraints

as done by Hu et al. [64]. Additionally, it is proposed to adapt the design of multi-material joints explicitly as functionally graded interfaces in order to improve stress transfer between materials and prevent joint failure [65]. Subsequently, the printing of the multi-material structures is also recommended to accommodate the tested approach of mechanical interlocking as a means for creating the functionally graded interfaces assumed during optimization [66], [67]. As a result, when creating the G-code for continuous fibre paths of composite material, considering individual printing heads for each of the two materials and including functionally graded material at the interfaces is a must.

Lastly, unlike the NN-based TO approach of Chandrasekhar et al. [33] that optimized multi-material structures with both isotropic and anisotropic materials using CFAO, this work is limited to using all anisotropic materials. This is often not the case for real-world structures that could benefit from a multi-material topology optimization approach. Such an optimization approach could help obtain better stress-optimized structures through the distribution of isotropic materials in regions with multi-axial load paths. This can reduce stress concentrations at such intersections as also observed in the works of Schmidt et al. [37] and Kundu and Zhang [50]. Hence, a promising future direction to broaden the scope of this framework and incorporate more real-world applicability includes consideration of both anisotropic and isotropic materials in the same gradient-based framework.

# References

[1] F. Mathys, P. Wild, and J. Wang, *Co2 reduction measures in the aviation industry: Current measures and outlook*, 2021. [Online]. Available: `https://commons.erau.edu/ijaaa/vol8/iss2/6/`.

[2] L. Jing, H. M. El-Houjeiri, J. C. Monfort, *et al.*, "Understanding variability in petroleum jet fuel life cycle greenhouse gas emissions to inform aviation decarbonization," *Nature Communications*, vol. 13, no. 1, Dec. 2022. DOI: `10.1038/s41467-022-35392-1`.

[3] L. Zhu, N. Li, and P. R. N. Childs, "Light-weighting in aerospace component and system design," vol. 7, pp. 103–119, Jun. 2018, ISSN: 2212-540X. DOI: `10.1016/j.jppr.2018.04.001`.

[4] M. Marino and R. Sabatini, "Advanced lightweight aircraft design configurations for green operations," 2014. [Online]. Available: `https://www.researchgate.net/publication/268814067_Advanced_Lightweight_Aircraft_Design_Configurations_for_Green_Operations`.

[5] K. Lau, P. Hung, M. H. Zhu, and D. Hui, "Properties of natural fibre composites for structural engineering applications," en, vol. 136, pp. 222–233, Mar. 2018, ISSN: 13598368. DOI: `10.1016/j.compositesb.2017.10.038`.

[6] A. Castro Almeida, E. Duriez, F. Lachaud, K. Masania, and J. Morlier, *Co2 footprint minimization for afp bio-composites thin structures*, Dec. 2022. [Online]. Available: `https://oatao.univ-toulouse.fr/29513/`.

[7] J. R. R. A. Martins and A. Ning, *Engineering Design Optimization*, en, 1st ed. Cambridge University Press, Nov. 2021, ISBN: 978-1-108-98064-7. DOI: `10.1017/9781108980647`.

[8] A. W. Gebisa and H. G. Lemu, "A case study on topology optimized design for additive manufacturing," en, *IOP Conference Series: Materials Science and Engineering*, vol. 276, no. 1, Dec. 2017, ISSN: 1757-899X. DOI: `10.1088/1757-899X/276/1/012026`.

[9] M. Lang, "Simultaneous structural and material optimization," English, embargoed until null, Ph.D. dissertation, Montanuniversitaet Leoben (000), 2021. [Online]. Available: `https://pure.unileoben.ac.at/en/publications/simultaneous-structural-and-material-optimization`.

[10] E. Stragiotti, "Continuous fiber path planning algorithm for 3d printed optimal mechanical properties," en, 2020. DOI: `10.13140/RG.2.2.30196.07046`. [Online]. Available: `http://rgdoi.net/10.13140/RG.2.2.30196.07046`.

[11] J. Plocher and A. Panesar, "Review on design and structural optimisation in additive manufacturing: Towards next-generation lightweight structures," en, vol. 183, Dec. 2019, ISSN: 0264-1275. DOI: `10.1016/j.matdes.2019.108164`.

[12] O. Sigmund and K. Maute, "Topology optimization approaches," en, *Structural and Multidisciplinary Optimization*, vol. 48, no. 6, pp. 1031–1055, Dec. 2013, ISSN: 1615-1488. DOI: `10.1007/s00158-013-0978-6`.

[13] E. Duriez, "Combiner l'éco-conception et l'optimisation topologique multi-échelle pour des structures micro-architecturées imprimées 3d," 2022ESAE0045, Ph.D. dissertation, 2022. [Online]. Available: http://www.theses.fr/2022ESAE0045/document.

[14] M. Bendsøe and O. Sigmund, *Topology optimization. Theory, methods, and applications. 2nd ed., corrected printing.* Jan. 2004, ISBN: 978-3-642-07698-5. DOI: 10.1007/978-3-662-05086-6.

[15] N. Ranaivomiarana, *Simultaneous optimization of topology and material anisotropy for aeronautic structures*, Mar. 2019. [Online]. Available: https://hal.science/tel-02200522/document.

[16] J. Stegmann and E. Lund, "Discrete material optimization of general composite shell structures," en, *International Journal for Numerical Methods in Engineering*, vol. 62, no. 14, pp. 2009–2027, 2005, ISSN: 1097-0207. DOI: 10.1002/nme.1259.

[17] J. P. Blasques and M. Stolpe, "Maximum stiffness and minimum weight optimization of laminated composite beams using continuous fiber angles," en, *Structural and Multidisciplinary Optimization*, vol. 43, no. 4, pp. 573–588, Apr. 2011, ISSN: 1615-1488. DOI: 10.1007/s00158-010-0592-9.

[18] T. Nomura, A. Kawamoto, T. Kondoh, *et al.*, "Inverse design of structure and fiber orientation by means of topology optimization with tensor field variables," en, *Composites Part B: Engineering*, vol. 176, Nov. 2019, ISSN: 1359-8368. DOI: 10.1016/j.compositesb.2019.107187.

[19] A. Desai, M. Mogra, S. Sridhara, K. Kumar, G. Sesha, and G. K. Ananthasuresh, "Topological-derivative-based design of stiff fiber-reinforced structures with optimally oriented continuous fibers," en, *Structural and Multidisciplinary Optimization*, vol. 63, no. 2, pp. 703–720, Feb. 2021, ISSN: 1615-1488. DOI: 10.1007/s00158-020-02721-1.

[20] Y. Luo, W. Chen, S. Liu, Q. Li, and Y. Ma, "A discrete-continuous parameterization (dcp) for concurrent optimization of structural topologies and continuous material orientations," en, *Composite Structures*, vol. 236, Mar. 2020, ISSN: 0263-8223. DOI: 10.1016/j.compstruct.2020.111900.

[21] Z. Qiu, Q. Li, Y. Luo, and S. Liu, "Concurrent topology and fiber orientation optimization method for fiber-reinforced composites based on composite additive manufacturing," en, *Computer Methods in Applied Mechanics and Engineering*, vol. 395, May 2022, ISSN: 0045-7825. DOI: 10.1016/j.cma.2022.114962.

[22] Y. Gandhi and G. Minak, "A review on topology optimization strategies for additively manufactured continuous fiber-reinforced composite structures," en, *Applied Sciences*, vol. 12, no. 21, Nov. 2022, ISSN: 2076-3417. DOI: 10.3390/app122111211.

[23] Y. Zhou, T. Nomura, E. Zhao, and K. Saitou, "Large-scale three-dimensional anisotropic topology optimization of variable-axial lightweight composite structures," *Journal of Mechanical Design*, vol. 144, no. 1, Jul. 2021, ISSN: 1050-0472. DOI: 10.1115/1.4051721. [Online]. Available: https://doi.org/10.1115/1.4051721.

[24] H. P. Jia, C. D. Jiang, G. P. Li, R. Q. Mu, B. Liu, and C. B. Jiang, "Topology optimization of orthotropic material structure," en, *Materials Science Forum*, vol. 575578, pp. 978–989, 2008, ISSN: 1662-9752. DOI: 10.4028/www.scientific.net/MSF.575-578.978.

[25] D. Jiang, R. Hoglund, and D. E. Smith, "Continuous fiber angle topology optimization for polymer composite deposition additive manufacturing applications," en, *Fibers*, vol. 7, no. 22, Feb. 2019, ISSN: 2079-6439. DOI: 10.3390/fib7020014.

[26] T. Maury, P. Loubet, S. M. Serrano, A. Gallice, and G. Sonnemann, "Application of environmental life cycle assessment (lca) within the space sector: A state of the art," en, *Acta Astronautica*, vol. 170, pp. 122–135, May 2020, ISSN: 00945765. DOI: `10.1016/j.actaastro.2020.01.035`.

[27] G. Barjoveanu, C. Teodosiu, M. Mihai, *et al.*, "Chapter 12 - life cycle assessment for eco-design in product development," en, in *Assessing Progress Towards Sustainability*, C. Teodosiu, S. Fiore, and A. Hospido, Eds. Elsevier, Jan. 2022, pp. 247–271, ISBN: 978-0-323-85851-9. DOI: `10.1016/B978-0-323-85851-9.00012-2`.

[28] J. Tao, L. Li, and S. Yu, "An innovative eco-design approach based on integration of lca, cadcae and optimization tools, and its implementation perspectives," en, *Journal of Cleaner Production*, vol. 187, pp. 839–851, Jun. 2018, ISSN: 0959-6526. DOI: `10.1016/j.jclepro.2018.03.213`.

[29] E. Duriez, C. Azzaro-Pantel, J. Morlier, and M. Charlotte, "A fast method of material, design and process eco-selection via topology optimization, for additive manufactured structures," en, *Cleaner Environmental Systems*, vol. 9, Jun. 2023, ISSN: 2666-7894. DOI: `10.1016/j.cesys.2023.100114`.

[30] S. W. K. Roper, H. Lee, M. Huh, and I. Y. Kim, "Simultaneous isotropic and anisotropic multi-material topology optimization for conceptual-level design of aerospace components," en, *Structural and Multidisciplinary Optimization*, vol. 64, no. 1, pp. 441–456, Jul. 2021, ISSN: 1615-1488. DOI: `10.1007/s00158-021-02893-4`.

[31] W. Zuo and K. Saitou, "Multi-material topology optimization using ordered simp interpolation," en, *Structural and Multidisciplinary Optimization*, vol. 55, no. 2, pp. 477–491, Feb. 2017, ISSN: 1615-1488. DOI: `10.1007/s00158-016-1513-3`.

[32] Z. Duan, Y. Liu, J. Fan, *et al.*, "Concurrent multi-material and multi-scale design optimization of fiber-reinforced composite material and structures for minimum structural compliance," en, *Composite Structures*, vol. 311, May 2023, ISSN: 0263-8223. DOI: `10.1016/j.compstruct.2023.116796`.

[33] A. Chandrasekhar, A. Mirzendehdel, M. Behandish, and K. Suresh, "Frc-tounn: Topology optimization of continuous fiber reinforced composites using neural network," en, no. arXiv:2205.03737, May 2022, arXiv:2205.03737 [cs]. [Online]. Available: `http://arxiv.org/abs/2205.03737`.

[34] L. Yin and G. Ananthasuresh, "Topology optimization of compliant mechanisms with multiple materials using a peak function material interpolation scheme," en, *Structural and Multidisciplinary Optimization*, vol. 23, no. 1, pp. 49–62, Dec. 2001, ISSN: 1615-1488. DOI: `10.1007/s00158-001-0165-z`.

[35] E. D. Sanders, M. A. Aguiló, and G. H. Paulino, "Multi-material continuum topology optimization with arbitrary volume and mass constraints," *Computer Methods in Applied Mechanics and Engineering*, vol. 340, pp. 798–823, 2018, ISSN: 0045-7825. DOI: `https://doi.org/10.1016/j.cma.2018.01.032`.

[36] T. Gao, W. Zhang, and P. Duysinx, "Comparison of volume constraint and mass constraint in structural topology optimization with multiphase materials," Sep. 2010, `https://www.researchgate.net/publication/266522668_Comparison_of_volume_constraint_and_mass_constraint_in_structural_topology_optimization_with_multiphase_materials/figures?lo=1&utm_source=google&utm_medium=organic`.

[37] M. P. Schmidt, L. Couret, C. Gout, and C. B. W. Pedersen, "Structural topology optimization with smoothly varying fiber orientations," en, *Structural and Multidisciplinary Optimization*, vol. 62, no. 6, pp. 3105–3126, Dec. 2020, ISSN: 1615-1488. DOI: `10.1007/s00158-020-02657-6`.

[38] T. Nomura, E. M. Dede, J. Lee, *et al.*, "General topology optimization method with continuous and discrete orientation design using isoparametric projection," *International Journal for Numerical Methods in Engineering*, vol. 101, no. 8, pp. 571–605, 2015. DOI: `https://doi.org/10.1002/nme.4799`.

[39] D. R. Jantos, K. Hackl, and P. Junker, "Topology optimization with anisotropic materials, including a filter to smooth fiber pathways," en, *Structural and Multidisciplinary Optimization*, vol. 61, no. 5, pp. 2135–2154, May 2020, ISSN: 1615-1488. DOI: `10.1007/s00158-019-02461-x`.

[40] M. Bruyneel, "Sfp a new parameterization based on shape functions for optimal material selection: Application to conventional composite plies," en, *Structural and Multidisciplinary Optimization*, vol. 43, no. 1, pp. 17–27, Jan. 2011, ISSN: 1615-147X, 1615-1488. DOI: `10.1007/s00158-010-0548-0`.

[41] O. Sigmund and S. Torquato, "Design of materials with extreme thermal expansion using a three-phase topology optimization method," *Journal of the Mechanics and Physics of Solids*, vol. 45, no. 6, pp. 1037–1067, 1997, ISSN: 0022-5096. DOI: `https://doi.org/10.1016/S0022-5096(96)00114-7`.

[42] E. D. Sanders, A. Pereira, M. A. Aguiló, and G. H. Paulino, "Polymat: An efficient matlab code for multi-material topology optimization," en, *Structural and Multidisciplinary Optimization*, vol. 58, no. 6, pp. 2727–2759, Dec. 2018, ISSN: 1615-1488. DOI: `10.1007/s00158-018-2094-0`.

[43] B. Yi, G. H. Yoon, R. Zheng, L. Liu, D. Li, and X. Peng, "A unified material interpolation for topology optimization of multi-materials," *Computers Structures*, vol. 282, Jul. 2023, ISSN: 0045-7949. DOI: `10.1016/j.compstruc.2023.107041`.

[44] S. Rojas-Labanda and M. Stolpe, "Benchmarking optimization solvers for structural topology optimization," en, *Structural and Multidisciplinary Optimization*, vol. 52, no. 3, pp. 527–547, Sep. 2015, ISSN: 1615-1488. DOI: `10.1007/s00158-015-1250-z`.

[45] E. Alcazar, "Exploring the method of moving asymptotes for various optimization applications," en, Aug. 2021, `http://hdl.handle.net/1853/65142`.

[46] K. d. Zuo, L. P. Chen, Y. Zhang, and J. Yang, "Study of key algorithms in topology optimization," *International Journal of Advanced Manufacturing Technology*, vol. 32, pp. 787–796, Apr. 2007. DOI: `10.1007/s00170-005-0387-0`.

[47] O. Sigmund, "Morphology-based black and white filters for topology optimization," *Structural and Multidisciplinary Optimization*, vol. 33, pp. 401–424, Apr. 2007. DOI: `10.1007/s00158-006-0087-x`.

[48] J. Wu, N. Aage, R. Westermann, and O. Sigmund, "Infill optimization for additive manufacturingapproaching bone-like porous structures," *IEEE Transactions on Visualization and Computer Graphics*, vol. 24, no. 2, pp. 1127–1140, Feb. 2018, ISSN: 1077-2626, 1941-0506, 2160-9306. DOI: `10.1109/TVCG.2017.2655523`.

[49] R. Zheng, B. Yi, X. Peng, and G.-H. Yoon, "An efficient code for the multi-material topology optimization of 2d/3d continuum structures written in matlab," en, vol. 14, Jan. 2024, ISSN: 2076-3417. DOI: `10.3390/app14020657`.

[50] R. D. Kundu and X. S. Zhang, "Stress-based topology optimization for fiber composites with improved stiffness and strength: Integrating anisotropic and isotropic materials," *Composite Structures*, vol. 320, Sep. 2023, ISSN: 0263-8223. DOI: `10.1016/j.compstruct.2023.117041`.

[51] S. Setoodeh, *Optimal design of variable-stiffness fiber-reinforced composites using cellular automata*, Jun. 2015. [Online]. Available: `https://repository.tudelft.nl/islandora/object/uuid%3A89b628b0-a91a-4d32-b5dc-598b11d327cf`.

[52] M. Abdelhamid and A. Czekanski, "Revisiting non-convexity in topology optimization of compliance minimization problems," *Engineering Computations*, vol. 39, no. 3, pp. 893–915, Jan. 2021, ISSN: 0264-4401. DOI: `10.1108/EC-01-2021-0052`.

[53] E. Andreassen, A. Clausen, M. Schevenels, B. S. Lazarov, and O. Sigmund, "Efficient topology optimization in matlab using 88 lines of code," en, *Structural and Multidisciplinary Optimization*, vol. 43, no. 1, pp. 1–16, Jan. 2011, ISSN: 1615-1488. DOI: `10.1007/s00158-010-0594-7`.

[54] D. Griffiths, *Stiffness matrix of the four-node quadrilateral element in closed form*, 1994. [Online]. Available: `http://inside.mines.edu/~vgriffit/pubs/All_J_Pubs/28.pdf`.

[55] K. Svanberg, "The method of moving asymptotesa new method for structural optimization," en, *International Journal for Numerical Methods in Engineering*, vol. 24, no. 2, pp. 359–373, 1987, ISSN: 1097-0207. DOI: `10.1002/nme.1620240207`.

[56] K. Svanberg, "Mma and gcmma  two methods for nonlinear optimization," 2014. [Online]. Available: `https://api.semanticscholar.org/CorpusID:211105912`.

[57] V. Bukshtynov, O. Volkov, L. J. Durlofsky, and K. Aziz, "Comprehensive framework for gradient-based optimization in closed-loop reservoir management," en, *Computational Geosciences*, vol. 19, no. 4, pp. 877–897, Aug. 2015, ISSN: 1573-1499. DOI: `10.1007/s10596-015-9496-5`.

[58] S. Rojas Labanda and M. Stolpe, "Automatic penalty continuation in structural topology optimization," *Structural and Multidisciplinary Optimization*, vol. 52, Jul. 2015. DOI: `10.1007/s00158-015-1277-1`.

[59] P. M. A. da Costa, *Optimization of structures in composite reinforced by fiber and bidimensional additive processes*, Dec. 2019. [Online]. Available: `https://fenix.tecnico.ulisboa.pt/downloadFile/1689244997260300/Pedro_Costa_78581_MasterThesis_compressed.pdf`.

[60] X. Yan, Q. Xu, D. Huang, Y. Zhong, and X. Huang, "Concurrent topology design of structures and materials with optimal material orientation," *Composite Structures*, vol. 220, pp. 473–480, Jul. 2019, ISSN: 0263-8223. DOI: `10.1016/j.compstruct.2019.04.028`.

[61] E. Duriez, J. Morlier, C. Azzaro-Pantel, and M. Charlotte, "Ecodesign with topology optimization," en, *Procedia CIRP*, vol. 109, pp. 454–459, 2022, ISSN: 22128271. DOI: `10.1016/j.procir.2022.05.278`.

[62] Y. Deng, *Life cycle assessment of biobased fibre-reinforced polymer composites*, en, 2014. [Online]. Available: `https://www.kuleuven.be/doctoraatsverdediging/fiches/3E09/3E090884.htm`.

[63] L. Li and K. Khandelwal, "Volume preserving projection filters and continuation methods in topology optimization," *Engineering Structures*, vol. 85, pp. 144–161, Feb. 2015, ISSN: 0141-0296. DOI: `10.1016/j.engstruct.2014.10.052`.

[64] J. Hu, Y. Liu, Y. Luo, H. Huang, and S. Liu, "Topology optimization of multi-material structures considering a piecewise interface stress constraint," en, *Computer Methods in Applied Mechanics and Engineering*, vol. 398, Aug. 2022, ISSN: 0045-7825. DOI: `10.1016/j.cma.2022.115274`.

[65] B. Liu, X. Huang, and Y. Cui, "Topology optimization of multi-material structures with explicitly graded interfaces," en, *Computer Methods in Applied Mechanics and Engineering*, vol. 398, Aug. 2022, ISSN: 0045-7825. DOI: `10.1016/j.cma.2022.115166`.

[66] S. Hasanov, A. Gupta, F. Alifui-Segbaya, and I. Fidan, "Hierarchical homogenization and experimental evaluation of functionally graded materials manufactured by the fused filament fabrication process," en, *Composite Structures*, vol. 275, Nov. 2021, ISSN: 0263-8223. DOI: `10.1016/j.compstruct.2021.114488`.

[67] N. Kwon, H. Deshpande, M. K. Hasan, A. Darnal, and J. Kim, "Multi-ttach: Techniques to enhance multi-material attachments in low-cost fdm 3d printing," en, in *Symposium on Computational Fabrication*, Virtual Event USA: ACM, Oct. 2021, pp. 1–16, ISBN: 978-1-4503-9090-3. DOI: `10.1145/3485114.3485116`. [Online]. Available: `https://dl.acm.org/doi/10.1145/3485114.3485116`.

# A

# Impact of fibre filtering scheme on domains with passive regions

Figure A.1 shows the effect of using two different filtering definitions on the fibre smoothening of an L-shape beam. Figure A.1a shows the design domain and the passive region definition for this L-shape beam. Figure A.1b shows the results obtained using the unmodified Gaussian filter defined in the work of Stragiotti [10]. In this case, the filtered fibre angles are influenced by the angles in the passive region. This causes fibres to not align along the load path followed by the topology. The modifications to this filter, which were necessary to consider the effect of passive regions, could not be generalized in this work. However, better filtering results are obtained with a simple convolution-type filtering, as defined in Equation 4.5 in Section 4.1.3. This can be seen in Figure A.1c, where the fibres are better aligned and without influence from the passive regions after filtering.
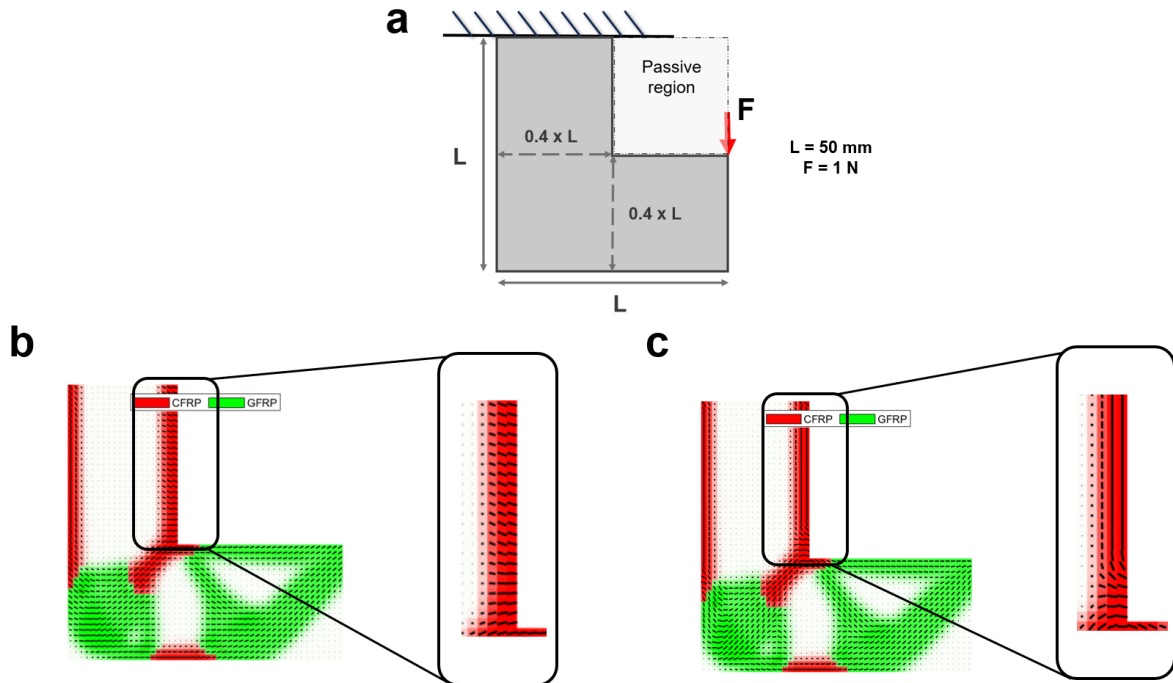


**Figure A.1:** (a) Design domain definition for an L-shape beam with the passive region. (b) When the Gaussian filter from [10] is used, the fibre angles along the passive region are no longer aligned along the optimized topological features post-filtering. (c) When a simple convolution type filter from [21] is used, the fibre angles along the passive region are still mostly aligned along the optimized topological features post-filtering.

# B

# Implementating gradient calculation in MM-FATO

For the template-based approach also used by Chandrasekhar et al. [33] in their work, we assume the elemental stiffness matrix $[K_e]$ as being divided into six components, one each for the six unique entries of the constitutive matrix defined in Equation 4.10. This can be seen from the expression shown in Equation B.1. Where $\hat{K}^i$ is a constant that is calculated once at the beginning of the optimization using expressions B.2 and B.3.

$$\begin{aligned} \mathbf{K_e} &= D_{11}\hat{\mathbf{K}}^{\mathbf{1}} + D_{22}\hat{\mathbf{K}}^{\mathbf{2}} + D_{33}\hat{\mathbf{K}}^{\mathbf{3}} \\ &+ D_{12}\hat{\mathbf{K}}^{\mathbf{4}} + D_{13}\hat{\mathbf{K}}^{\mathbf{5}} + D_{23}\hat{\mathbf{K}}^{\mathbf{6}} \end{aligned} \tag{B.1}$$

$$\hat{\mathbf{K}}^{\mathbf{i}} = \int_{\Omega_e} \mathbf{B}^{\mathbf{T}}\hat{\mathbf{D}}^{\mathbf{i}}\mathbf{B}d\Omega_e, \quad i = 1, 2, \dots 6 \tag{B.2}$$

$$\begin{aligned}
\hat{\mathbf{D}}^{\mathbf{1}} &= \begin{bmatrix} 1 & 0 & 0 \\ 0 & 0 & 0 \\ 0 & 0 & 0 \end{bmatrix} \hat{\mathbf{D}}^{\mathbf{2}} = \begin{bmatrix} 0 & 0 & 0 \\ 0 & 1 & 0 \\ 0 & 0 & 0 \end{bmatrix} \hat{\mathbf{D}}^{\mathbf{3}} = \begin{bmatrix} 0 & 0 & 0 \\ 0 & 0 & 0 \\ 0 & 0 & 1 \end{bmatrix} \\
\hat{\mathbf{D}}^{\mathbf{4}} &= \begin{bmatrix} 0 & 1 & 0 \\ 1 & 0 & 0 \\ 0 & 0 & 0 \end{bmatrix} \hat{\mathbf{D}}^{\mathbf{5}} = \begin{bmatrix} 0 & 0 & 1 \\ 0 & 0 & 0 \\ 1 & 0 & 0 \end{bmatrix} \hat{\mathbf{D}}^{\mathbf{6}} = \begin{bmatrix} 0 & 0 & 0 \\ 0 & 0 & 1 \\ 0 & 1 & 0 \end{bmatrix}
\end{aligned} \tag{B.3}$$

Then, during the material interpolation calculations in the MATLAB implementation, constitutive matrix elements $D_{11}$, $D_{12}, D_{22}, D_{13}, D_{23}$ and $D_{33}$ are calculated for each material and the $\mathbf{D_e^1}$ and $\mathbf{D_e^2}$ in Equation 4.18 and 4.19 are treated individually as $\mathbf{D_e^{1,k}}$ and $\mathbf{D_e^{2,k}}$ respectively. As a result, we have six different terms for $\frac{\partial \mathbf{D_e}}{\partial x_e^{matj}}$. Finally, the sensitivities can be assembled by incorporating the relation for $\mathbf{K_e}$ (Equation B.1) to Equation 4.16. As a result, the calculation of the derivative of the objective function with respect to the material selection design variables $x_e^{mat1}$ and $x_e^{mat2}$ can be modified as shown in Equation B.4.

$$\frac{\partial \mathrm{C}}{\partial x_e^{matj}} = \int_{k=1}^{6} \frac{\partial \mathbf{D_e^k}}{\partial x_e^{matj}} \left( \mathbf{U_e^T} \left( \int_{\Omega_e} \mathbf{B^T}\hat{\mathbf{K}}^{\mathbf{i}}\mathbf{B}d\Omega_e \right) \mathbf{U_e} \right); \qquad j = 1, 2 \tag{B.4}$$

# C

# Fixed Penalty Approach for MM-FATO

In lieu of penalty continuation, to obtain feasible topology optimized topology while keeping computation costs to a minimum, a fixed penalty approach can be used for MM-FATO framework as well. Figure C.1 illustrates how different penalty values affect the obtained topology. We observe that a fixed penalty of three and four is not enough to penalise the intermediate densities and generate more discrete designs, and a lot of interfaces are created between the two materials. Thresholding is used to demonstrate how the topologies evolve when the intermediate densities are pushed to 0-1 based on the threshold value, i.e., $\rho_e \geq 0.5 = 1$, else 0.
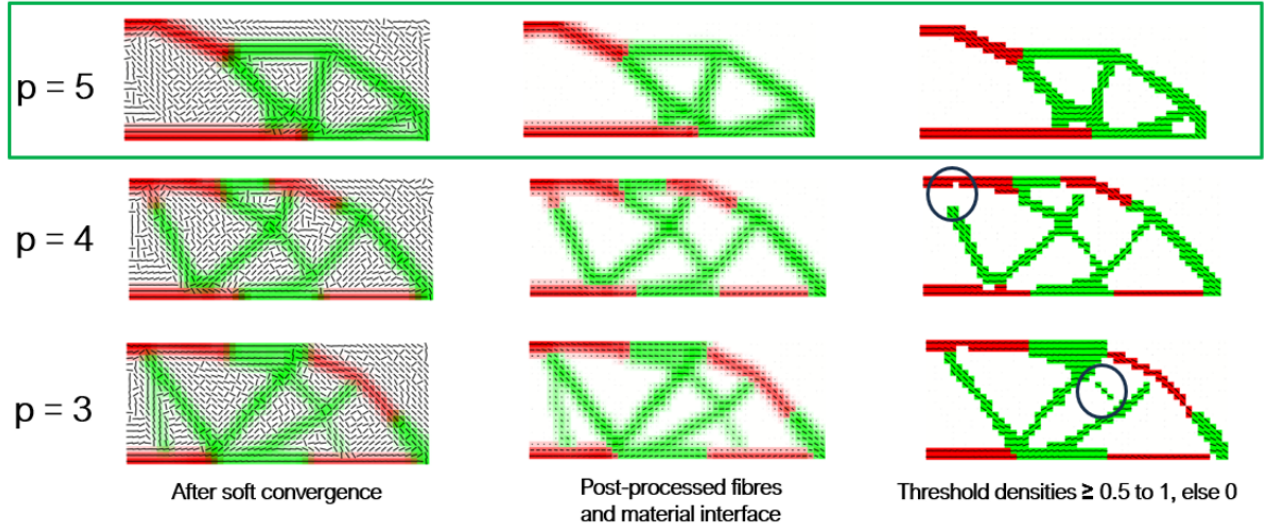


**Figure C.1:** Topologies obtained for varying fixed penalty values of p = 3,4 and 5. When thresholding is applied, such that densities $\geq 0.5$ are equated to 1 and the rest to zero, p = 5 emerges as a minimum penalty value required to attain manufacturable topologies on direct thresholding of optimized topologies.